Two dimensional hydrodynamic instabilities in shear flows

by

Anirban Guha

M.A.Sc., Mechanical Engineering, University of Windsor, ON, Canada, 2008
B.E., Mechanical Engineering, Jadavpur University, India, 2004

A THESIS SUBMITTED IN PARTIAL FULFILLMENT OF
THE REQUIREMENTS FOR THE DEGREE OF

DOCTOR OF PHILOSOPHY

in

The Faculty of Graduate Studies

(Civil Engineering)

THE UNIVERSITY OF BRITISH COLUMBIA

(Vancouver)

June 2013

Abstract

Hydrodynamic instabilities occurring in two dimensional shear flows have been investigated. First, the process of resonant interaction between two progressive interfacial waves is studied. Such interaction produces exponentially growing instabilities in idealized, homogeneous or density stratified, inviscid shear layers. It is shown that two oppositely propagating interfacial waves, having arbitrary initial amplitudes and phases, eventually phase-lock, provided they satisfy a particular condition. Three types of shear instabilities - Kelvin Helmholtz, Holmboe and Taylor have been studied. The above-mentioned condition provides a range of unstable wavenumbers for each instability type, and this range matches the predictions of the canonical normal-mode based linear stability theory.

The non-linear evolution of Kelvin-Helmholtz (KH) instability has been studied. The commonly known manifestation of KH is in the form of spiral billows. However, KH evolving from a piecewise linear shear layer is remarkably different; it is characterized by elliptical vortices of constant vorticity connected via thin braids. Using direct numerical simulation and contour dynamics, it is shown that the interaction between two counter-propagating vorticity waves is solely responsible for this KH formation. The oscillation of the vorticity wave amplitude, the rotation and nutation of the elliptical vortex, and straining of the braids have been investigated.

Finally, the linear stability of plane Couette-Poiseuille flow in the presence of a cross-flow is studied. The base flow is characterized by the cross flow Reynolds number, Re_{inj} and the dimensionless wall velocity, k. Corresponding to each dimensionless wall velocity, $k \in [0, 1]$, two ranges of Re_{inj} exist where

unconditional stability is observed. In the lower range of Re_{inj} , for modest k we have a stabilization of long wavelengths leading to a cut-off Re_{inj}. As Re_{inj} is increased, we see first destabilization and then stabilization at very large Re_{inj}. Analysis of the eigenspectrum suggests the cause of instability is due to resonant interactions of Tollmien-Schlichting waves.

Preface

The second chapter of this thesis has been submitted to a peer-reviewed journal, while the third and fourth chapters are already published journal papers. The contributions of the co-authors are outlined as follows:

Chapter 2 has been submitted for publication with myself as the first author and G. A. Lawrence as the second. I was responsible for developing the idea and formulating the theory, validating it using Matlab and writing the manuscript. G. A. Lawrence edited and revised the manuscript.

Chapter 3 has been published in *Physical Review E*. I am the first author of this paper, the second and third authors respectively being M. Rahmani and G. A. Lawrence. I was responsible for developing the idea, writing the codes and preparing the manuscript. M. Rahmani was responsible for analyzing the DNS data, while G. A. Lawrence helped with writing the manuscript as well as providing an overall guidance.

Chapter 4 has been published in the *Journal of Fluid Mechanics* with myself as the first author and I. A. Frigaard as the second. I was responsible for developing the idea, writing the codes and preparing the manuscript. I. A. Frigaard helped me with writing the manuscript and providing mathematical insights.

Table of Contents

List of Tables

List of Figures

Acknowledgments

I humbly acknowledge the two major sources of financial support that I received during my Ph.D. studies, the Four Year Fellowship of UBC and the Faculty of Applied Science Graduate Award.

I would like to thank my Ph.D. supervisor, Prof. Greg Lawrence for his continuous encouragement, support and invaluable guidance. I am indebted to him for giving me the research freedom, and always having confidence in my abilities. This thesis would not be anywhere near the product it currently is if I was not given the opportunity to grow as an independent researcher. I would also like to thank my supervisory committee members - Bernard Laval, Neil Balmforth and Ian Frigaard for their help and valuable comments.

The general atmosphere of UBC has provided a great learning experience. I took many courses from other Departments, e.g. Mechanical, Mathematics, Physics and Earth and Ocean Sciences (again, thanks to Greg for giving me this freedom), and during this time I had the opportunity to interact with many great minds scattered across the campus. I took a course on Hydrodynamic stability with Prof. Ian Frigaard; the course project actually became the fourth chapter of my Ph.D. thesis. I am indebted to Prof. Frigaard for his help and guidance, and invaluable advise on academia in general. I am also indebted to

Prof. Neil Balmforth for being kind enough to lend his valuable time whenever needed. The long discussions we had on waves and instabilities have helped me a lot with my research. The Environmental Fluid Mechanics weekly lunch meetings also played a key role in my academic development - it has been a great peer learning experience. I would like to thank our EFM members Mona Rahmani, Ted Tedford, Jeff Carpenter and Andrew Hamilton, as well as Sarah Hormozi from the Institute of Applied Mathematics for their encouragement, help and support. Last but not the least, I am indebted to Prof. Kraig Winters of Scripps Institute of Oceanography. I was lucky to have him as my external examiner, and the advise I had from him is simply invaluable.

Special thanks for my wife, Tanaya, who is also a Ph.D. student at UBC. Long ago, when I just completed my Undergraduate degree and had no intention of pursuing higher studies, she made me believe that I am a "Ph.D. material". She has always been there by my side, and has kept on motivating and inspiring me everyday. I am also thankful to my Indian friends in Vancouver - Santanu Mitra and Anuradha Mitra, whose love, encouragement and hospitality I greatly treasure. Finally, I would like to thank my mother from the bottom of my heart. She undertook a lot of difficulties for my upbringing. I am what I am because of her.

My journey as a Ph.D. student has been an eventful and satisfying experience. I believe I have grown as an academic, a philosopher, and most importantly, as a human being.

Dedication

To the three lovely ladies - my mother, my wife, and my motherland...

Chapter 1

Introduction

It was easier to know it than to explain why I know it. — Sherlock Holmes in A Study in Scarlet.

Velocity gradient, also known as velocity shear (or simply, shear), is ubiquitous in natural and industrial flows. As an example, when a fluid flows past a stationary obstacle, its velocity varies from zero at the obstacle wall to the free stream velocity. Therefore a shear layer is produced adjacent to the wall, which is technically known as the boundary layer. Flows over topography or over aircraft wings are examples of boundary layer flows.

Shear flow is not necessarily wall bounded. In atmospheric and oceanic flows there are situations where the upper fluid is left (right) moving while the lower fluid is moving to the right (left). This is known as free shear flow and is typically observed in exchange dominated flows, e.g. oceanic gravity currents, estuarine flows and sea breezes. Natural exchange flows are often density stratified, hence understanding such shear flow dynamics requires consideration of the effects of density variations.

Shear flows can become hydrodynamically unstable, resulting in a process characterized by the growth of wavelike perturbations. These perturbations

can grow at an exponential rate, transforming the base flow from a laminar to turbulent state. Hence hydrodynamic instability is often regarded as the precursor of turbulence. During the instability mechanism energy is extracted from the large-scale motions and transferred to the smaller scales. The smallest scale processes are responsible for dissipating the mechanical energy into heat. If the flow is density stratified, the resulting mechanism leads to the mixing of the density field.

Turbulence and mixing are important aspects of many problems in meteorology, oceanography and several branches of engineering (e.g. mechanical, aerospace, environmental, chemical). In the aerospace industry, understanding boundary layer instabilities is crucial for reducing turbulent drag over an aircraft. In the fields of oceanography and atmospheric sciences, understanding free shear instabilities is important for developing accurate models for predicting weather and climate. Fig. 1.1 shows examples of wall bounded (boundary layer) and free shear turbulence.

1.1 Governing equations

In this thesis, we will only be considering two-dimensional flows. Let x be the streamwise direction and z be the cross-streamwise/vertical direction[1]. We assume the fluid to be incompressible and non-diffusive. Hence the conservation

[1]We replace z by y in Chapters 3 and 4, since the flows under consideration are most likely to occur in the horizontal plane.

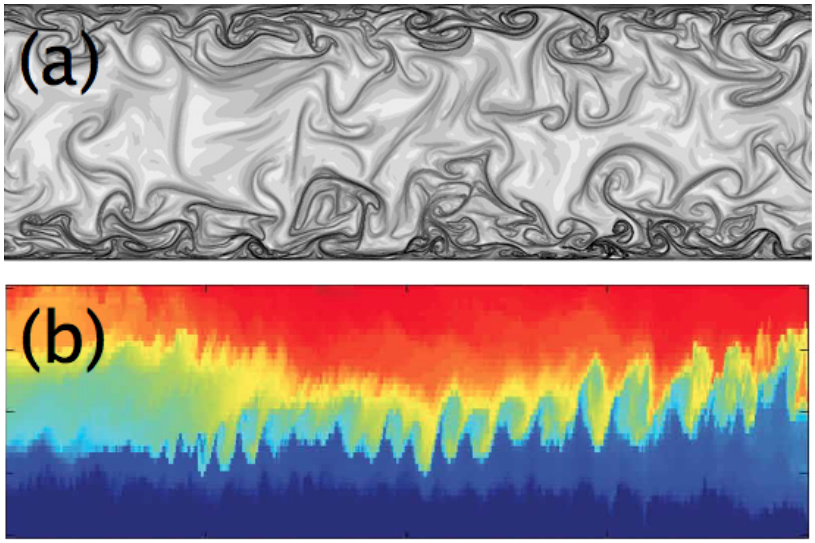

Figure 1.1: (a) Wall bounded turbulence in channel flow (Green, 2006) and (b) turbulence produced in the ocean mixing layer (Smyth & Moum, 2012).

of volume (continuity equation) can be written as

$$\frac{\partial u}{\partial x} + \frac{\partial w}{\partial z} = 0 \tag{1.1}$$

where (u, w) is the velocity field. Let us denote the density, pressure and kinematic viscosity by ρ, P, and ν respectively. Furthermore, we will only consider flows where density variations are either small or negligible. The effect of small density variations is included through Boussinesq approximations (Kundu & Cohen, 2004), in which it is assumed that the variation in density is negligible except when ρ is multiplied by gravity, g. Following Kundu & Cohen (2004),

the two-dimensional, Boussinesq momentum equations are written as follows:

$$\frac{\partial u}{\partial t} + u\frac{\partial u}{\partial x} + w\frac{\partial u}{\partial z} = -\frac{1}{\rho_0}\frac{\partial P}{\partial x} + \nu\triangle u \tag{1.2}$$

$$\frac{\partial w}{\partial t} + u\frac{\partial w}{\partial x} + w\frac{\partial w}{\partial z} = -\frac{1}{\rho_0}\frac{\partial P}{\partial z} - g\frac{\rho}{\rho_0} + \nu\triangle w \tag{1.3}$$

where ρ_0 is a reference density, and $\triangle \equiv \partial^2/\partial x^2 + \partial^2/\partial z^2$. The fluid, assumed non-diffusive, also satisfies the conservation of mass:

$$\frac{\partial \rho}{\partial t} + u\frac{\partial \rho}{\partial x} + w\frac{\partial \rho}{\partial z} = 0 \tag{1.4}$$

1.2 Hydrodynamic stability theory

To understand the hydrodynamic stability of a given fluid flow, we follow the procedure outlined in Drazin & Reid (2004). We will be considering a background flow $U(z)$ (i.e. parallel to x and varying only in z) and background density $\bar{\rho}(z)$. The background flow is perturbed with a small two-dimensional perturbation velocity of $(u^{'}, w^{'})$, density of $\rho^{'}$, and pressure of $P^{'}$, so that the total two-dimensional velocity field, (u, w), density field, ρ, and pressure field, P, are

$$u = U + u^{'}, \quad w = w^{'}, \quad \rho = \bar{\rho} + \rho^{'}, \quad P = \bar{P} + P^{'}, \tag{1.5}$$

where $\bar{P}$ is the hydrostatic background pressure[2], implying $\partial\bar{P}/\partial z = -\bar{\rho}g$.

[2]The quantity $\partial\bar{P}/\partial x = 0$ in Chapters 2 and 3, whereas in Chapter 4 $\partial\bar{P}/\partial x =$ negative constant.

Using these relations along with Eq. (1.5) in Eqs. (1.2)-(1.3), we obtain

$$\frac{\partial u}{\partial t} + u\frac{\partial u}{\partial x} + w\frac{\partial u}{\partial z} = -\frac{1}{\rho_0}\frac{\partial P'}{\partial x} + \nu\triangle u \tag{1.6}$$

$$\frac{\partial w}{\partial t} + u\frac{\partial w}{\partial x} + w\frac{\partial w}{\partial z} = -\frac{1}{\rho_0}\frac{\partial P'}{\partial z} - g\frac{\rho'}{\rho_0} + \nu\triangle w \tag{1.7}$$

We can use the continuity equation (Eq. (1.1)) to define a streamfunction such that

$$u = \frac{\partial \psi}{\partial z} \;\; ; \;\; w = -\frac{\partial \psi}{\partial x} \tag{1.8}$$

Taking $\partial(1.6)/\partial z$ - $\partial(1.7)/\partial x$ and using Eq. (1.8), we formulate the vorticity equation:

$$\frac{\partial \triangle\psi}{\partial t} + u\frac{\partial \triangle\psi}{\partial x} + w\frac{\partial \triangle\psi}{\partial z} = \frac{g}{\rho_0}\frac{\partial \rho'}{\partial x} + \nu\triangle\triangle\psi \tag{1.9}$$

We define a characteristic length scale l, velocity scale δU and density scale $\delta\rho$. This allows us to represent Eq. (1.9) in complete non-dimensional form:

$$\frac{\partial \triangle\psi}{\partial t} + u\frac{\partial \triangle\psi}{\partial x} + w\frac{\partial \triangle\psi}{\partial z} = J\frac{\partial \rho'}{\partial x} + \frac{1}{Re}\triangle\triangle\psi \tag{1.10}$$

where J is the bulk Richardson number and Re is the Reynolds number, and are defined as follows:

$$J = \frac{\delta\rho\, g l}{\rho_0\,(\delta U)^2} \;\; ; \;\; Re = \frac{\delta U\, l}{\nu} \tag{1.11}$$

1.2.1 Linearization and normal mode analysis

We decompose ψ into mean and perturbation components: $\psi = \Psi(z) + \psi'$, and substitute it into Eq. (1.10). The equation is then linearized about the background state, i.e. terms with product of perturbation components are neglected. Similar treatment is also done on Eq. (1.4). The conventional way of solving the resulting linear equation is by applying the method of normal modes. In this method we assume the perturbation streamfunction and perturbation density to have the from $\psi^{'}(x,z,t) = \varphi(z)e^{i\alpha(x-ct)}$ and $\rho^{'}(x,z,t) = \hat{\rho}(z)e^{i\alpha(x-ct)}$ respectively, where i is the imaginary unit, α is the real wavenumber, and $c = c_r + ic_i$ is the complex phase speed of the mode. The quantities αc_i and c_r respectively denote the exponential growth rate and phase speed of the mode. When $c_i > 0$ the mode is unstable. Substitution of normal mode type perturbations into linearized Eqs. (1.10) and (1.4) yield the following eigenvalue problem-set:

$$[(c-U)(\alpha^2 - D^2) - D^2U]\varphi = J\hat{\rho} - \frac{i}{\alpha Re}(\alpha^2 - D^2)^2\varphi \tag{1.12}$$

$$(U-c)\hat{\rho} = \varphi D\bar{\rho} \tag{1.13}$$

where $D \equiv d/dz$. The above two equations can be combined to produce the stratified, viscous linear stability equation:

$$[(c-U)(\alpha^2 - D^2) - D^2U]\varphi = J\frac{D\bar{\rho}}{(U-c)}\varphi - \frac{i}{\alpha Re}(\alpha^2 - D^2)^2\varphi \tag{1.14}$$

If the flow is assumed inviscid ($Re \to \infty$), Eq. (1.14) produces the Taylor-Goldstein equation (Taylor, 1931; Goldstein, 1931):

$$D^2\varphi + \left[-J\frac{D\bar{\rho}}{(U-c)^2} - \frac{D^2U}{(U-c)} - \alpha^2\right]\varphi = 0 \tag{1.15}$$

If the flow is homogeneous and viscous, Eq. (1.14) produces the Orr-Sommerfield equation (Drazin & Reid, 2004):

$$\mathrm{i}\alpha Re[(c-U)(\alpha^2 - D^2) - D^2U]\varphi = (\alpha^2 - D^2)^2\varphi \tag{1.16}$$

1.2.2 Non-modal stability

In the above section, we have introduced the concept of normal-mode based linear stability theory. Although this theory is extremely useful, it provides limited insight into the physical mechanism(s) responsible for hydrodynamic instability. The answer to why an infinitesimal perturbation vigorously grows from a stable background flow is provided in the form of non-intuitive mathematical theorems - Rayleigh's inflection point theorem and Fjørtoft's extension for the case of homogeneous flows, and Miles-Howard criterion for stratified flows (Drazin & Reid, 2004). Since linear instability is the first step towards understanding the more complicated and highly elusive non-linear processes like chaos and turbulence, it is helpful to formulate alternative theories which are able to provide intuitive explanations. Another shortcoming of the normal mode stability theory is the normal-mode assumption itself. The extensive

work by Farrell (1984), Trefethen *et al.* (1993), Schmid & Henningson (2001) and others have shown that shear allows rapid non-modal transient growth due to non-orthogonal interaction between the modes. Farrell & Ioannou (1996) developed the Generalized stability theory for linear dynamical systems, and showed the process of obtaining the optimal non-modal growth from a singular value decomposition of the propagator matrix of the linear dynamical system.

Theories have been proposed to provide an intuitive understanding of the hydrodynamic instability process. Probably the first mechanistic picture of stratified shear instabilities was provided by Holmboe (1962). Using idealized velocity and density profiles, Holmboe postulated that the resonant interaction between stable propagating waves, each existing at a discontinuity in the background flow profile (density profile discontinuity produces gravity waves and vorticity profile discontinuity produces vorticity waves), yields exponentially growing instabilities. He was able to show that Kelvin-Helmholtz instability (Rayleigh, 1880) is the result of the interaction between two vorticity waves (also known as Rayleigh waves). Moreover, Holmboe also found a new type of instability, later came to be known as the "Holmboe instability", produced by the interaction between vorticity and gravity waves. Bretherton, a contemporary of Holmboe, proposed a similar theory to explain mid-latitude cyclogenesis (Bretherton, 1966). He hypothesized that the cyclones form due to a baroclinic instability mechanism caused by the interaction between two Rossby edge waves (vorticity waves in a rotating frame of reference), one existing at the earth's surface and the other located at the atmospheric tropopause.

The theory proposed by Holmboe and Bretherton has been refined and re-interpreted over the years, see Cairns (1979); Hoskins *et al.* (1985); Caulfield (1994); Baines & Mitsudera (1994); Heifetz *et al.* (1999); Carpenter *et al.* (2013). As reviewed in Carpenter *et al.* (2013), resonant interaction between two edge waves in an idealized homogeneous or stratified shear layer occurs when these waves attain a phase-locked state, i.e. they are at rest relative to each other. Maintaining this phase-locked configuration, the waves grow equally at an exponential rate. Hoskins *et al.* (1985) summarized the Rossby edge wave induced shear instability mechanism in one sentence:

> 'The induced velocity field of each Rossby wave
> keeps the other in step, and makes the other grow.'

1.3 Overview

In this thesis we have investigated various aspects of two dimensional shear flow instabilities. Chapter 2 is dedicated to providing a physical understanding of shear instabilities by looking into the problem from wave interaction perspective. The physical reason behind the growth of normal-mode type (i.e. exponentially growing) instabilities is obtained from this analysis. The investigation also provides valuable insight into the non-modal stability theory.

The idea proposed in Chapter 2 is extended to the non-linear regime in Chapter 3 for the case of Kelvin-Helmholtz instability. It has been shown that the non-linear interaction between two counter-propagating vorticity waves

produce elliptical vortex patches connected via thin braids. The vortex and braid dynamics have been investigated.

In Chapter 4 we have followed the conventional normal-mode approach to investigate how channel flows can be unconditionally stabilized/destabilized. In a parameter space of non-dimensional wall velocity and non-dimensional cross flow velocity, we have investigated how these two parameters influence the stability of a channel flow. It has been shown that the two effects compensate each other. Moreover, a small range of cross-flows have been shown to exist for which the channel flow is unconditionally linearly stable even in the absence of wall motion.

Chapter 2

Understanding the mechanism of shear instabilities from wave interaction perspective [1]

Before turning to those moral and mental aspects of the matter which present the greatest difficulties, let the inquirer begin by mastering more elementary problems. — Sherlock Holmes in A Study in Scarlet.

2.1 Introduction

In this Chapter we study shear instabilities in terms of interacting interfacial waves. Holmboe was probably the first to postulate that the resonant interaction between stable progressive waves, each existing at a discontinuity in the background flow profile (can be vorticity or density discontinuity), yields

[1] A version of this chapter has been submitted for publication. A. Guha and G. A. Lawrence (2013) A wave interaction approach to studying non-modal homogeneous and stratified shear instabilities.

exponentially growing instabilities. Holmboe showed that Kelvin-Helmholtz instability (Rayleigh, 1880) is the result of the interaction between two vorticity waves (also known as Rayleigh waves). Moreover, Holmboe also found a new type of instability, later came to be known as the "Holmboe instability", produced by the interaction between vorticity and gravity waves. Holmboe's hypothesis has been refined and re-interpreted over the years, see Cairns (1979); Hoskins *et al.* (1985); Caulfield (1994); Baines & Mitsudera (1994); Heifetz *et al.* (1999); Carpenter *et al.* (2013).

In recent years, Heifetz and co-authors (Heifetz *et al.*, 1999, 2004; Heifetz & Methven, 2005) have extensively studied the interaction between Rossby edge waves. By not limiting the Rossby edge waves to be of the normal-mode type, they were able to obtain non-modal instability and transient growth mechanisms. While Heifetz *et al.* (2004) derived the governing equations using the Hamiltonian approach, Heifetz & Methven (2005) used the streamfunction-vorticity approach. Their successful attempt has motivated us to formulate a generalized interfacial wave interaction technique for studying homogeneous and stratified shear instabilities. Without forcing the wave to be of the normal-mode type, and furthermore, without assuming any particular type of waveform (e.g. gravity wave or vorticity wave), we have formulated the governing equations for wave interaction. Our equations are derived from the linearized kinematic and dynamic (for stratified flows) conditions. Unlike Heifetz *et al.* (2004) and Heifetz & Methven (2005), our key variables are the vertical displacement and the vertical velocity of the wave. The choice of variables, along

with the derivation methodology, provide a deeper and probably more intuitive understanding of the wave interaction process.

2.2 Linear wave(s) at an interface

In the present study we consider multi-layered flows with constant density and vorticity in each layer. This configuration makes the equations of motion for perturbations within a layer to be the same as that in an irrotational background flow. The interface between two adjacent layers signifies a discontinuity in vorticity or density. The former is a vorticity interface, while the latter is a density interface. Let such an interface existing at a location $z = z_i$ be perturbed by an infinitesimal vertical displacement η_i, given as follows:

$$\eta_i = A_{\eta_i}(t)\cos[\alpha x + \phi_{\eta_i}(t)] \tag{2.1}$$

This displacement manifests itself in the form of stable, progressive wave(s), the amplitude and phase of which are A_{η_i} and ϕ_{η_i} respectively. While a vorticity interface produces a vorticity wave, two oppositely traveling gravity waves are produced in the case of a density interface. We have assumed the interfacial displacement (or the wave) to be monochromatic, having a wavenumber α. Moreover, the interface satisfies the *kinematic condition* - a particle initially on the interface will remain there forever. The linearized kinematic condition

is given by

$$\frac{\partial \eta_i}{\partial t} + U_i \frac{\partial \eta_i}{\partial x} = w_i \tag{2.2}$$

where $U_i \equiv U(z_i)$ is the background velocity and w_i is the vertical velocity at the interface. We prescribe the latter to be as follows:

$$w_i = A_{w_i}(t) \cos[\alpha x + \phi_{w_i}(t)] \tag{2.3}$$

Here A_{w_i} is the amplitude and ϕ_{w_i} is the phase of w_i. The interfacial deformation sets up an irrotational velocity field away from the interface (Holmboe, 1962; Caulfield, 1994):

$$\triangle \psi^{'} = 0 \text{ when } z \neq z_i \tag{2.4}$$

When the perturbation streamfunction of the form $\psi^{'}(x, z, t) = \varphi(z) e^{i(\alpha x + \theta_\psi(t))}$ is substituted in the above equation we get

$$\frac{\partial^2 \varphi}{\partial z^2} - \alpha^2 \varphi = 0 \tag{2.5}$$

The above equation yields $\varphi = e^{-\alpha|z-z_i|}\varphi_i$. The vertical velocity $w = -\frac{\partial \psi}{\partial x}$ is then given by

$$w = e^{-\alpha|z-z_i|} w_i \tag{2.6}$$

Substituting Eqs. (2.1) and (2.3) in Eq. (2.2), we obtain

$$\dot{A}_{\eta_i} \cos(\alpha x + \phi_{\eta_i}) - A_{\eta_i} \left(\alpha U_i + \dot{\phi}_{\eta_i}\right) \sin(\alpha x + \phi_{\eta_i}) = A_{w_i} \cos(\alpha x + \phi_{w_i}) \tag{2.7}$$

Here ϕ_{η_i}, $\phi_{w_i} \in [-\pi, \pi]$. The frequency and the growth rate of a wave are respectively defined as $\sigma_i \equiv -\dot{\phi}_{\eta_i}$ and $\gamma_i \equiv \dot{A}_{\eta_i}/A_{\eta_i}$ (overdot denotes d/dt). Using these definitions in Eq. (2.7), we get

$$\sigma_i = \alpha U_i - \omega_i \sin(\triangle\phi_{ii}) \tag{2.8}$$

$$\gamma_i = \omega_i \cos(\triangle\phi_{ii}) \tag{2.9}$$

where $\triangle\phi_{ii} \equiv \phi_{w_i} - \phi_{\eta_i}$. In order to get Eqs. (2.8)-(2.9) from Eq. (2.7), we write the R.H.S. of Eq. (2.7) as follows: $A_{w_i}\cos(\alpha x + \phi_{w_i}) = A_{w_i}\cos(\alpha x + \phi_{\eta_i} + \triangle\phi_{ii})$. The cosine function is expanded using a standard trigonometric identity. Finally we collect the coefficients of $\sin(\alpha x)$ and $\cos(\alpha x)$.

Eq. (2.8) shows that the frequency of a wave consists of two components - (i) the Doppler shift αU_i due to the background velocity, and (ii) the *intrinsic frequency* $-\omega_i \sin(\triangle\phi_{ii})$, where $\omega_i \equiv A_{w_i}/A_{\eta_i}$. The phase-speed $c_i \equiv \sigma_i/\alpha$ of the wave is found to be

$$c_i = U_i - \frac{\omega_i}{\alpha}\sin(\triangle\phi_{ii}) \tag{2.10}$$

The last term (including the negative sign) denotes the *intrinsic phase-speed*. Noting that a wave in isolation cannot grow or decay on its own, Eq. (2.9) demands that $|\triangle\phi_{ii}| = \pi/2$. Therefore for a stable wave, the vertical velocity field at the interface has to be in quadrature with the interfacial deformation. According to Eqs. (2.8) and (2.10), the quadrature condition makes the mag-

nitude of the intrinsic frequency and the intrinsic phase-speed to be ω_i and ω_i/α respectively. The *intrinsic direction of motion* of the wave, however, is determined by $\triangle\phi_{ii}$. For waves moving to the left relative to the interfacial velocity U_i, $\triangle\phi_{ii} = \pi/2$. Similarly for right moving waves, $\triangle\phi_{ii} = -\pi/2$. When such a stable, progressive wave is acted upon by external influence(s) (e.g. when another wave interacts with the given wave, as detailed in §2.3), the quadrature condition is no longer satisfied, i.e. $|\triangle\phi_{ii}| \neq \pi/2$. Therefore, the wave may grow ($\gamma_i > 0$) or decay ($\gamma_i < 0$), and its intrinsic frequency and phase-speed may change.

In our analyses we will consider two types of progressive interfacial waves - vorticity waves and internal gravity waves.

2.2.1 Vorticity waves

Vorticity waves, also known as Rayleigh waves, exist at a vorticity interface (i.e. regions involving a sharp change in vorticity). Such interfaces are a common feature in the atmosphere and oceans. In rotating frame, the analogue of vorticity wave is the Rossby edge wave which exists at a sharp transition in the potential vorticity. When Rossby edge waves propagate in a direction opposite to the background flow, they are called "counter-propagating Rossby waves" or CRWs (Heifetz *et al.*, 1999).

In order to evaluate the frequency ω_i of vorticity waves, let us consider a

velocity profile having the form

$$U(z) = \begin{cases} U_i & z \geq z_i \\ Sz & z \leq z_i \end{cases} \tag{2.11}$$

Here the constant $S = U_i/z_i$ is the vorticity, or the shear in the region $z \leq z_i$ (Carpenter *et al.*, 2013). In Eq. (2.11), the vorticity dU/dz is discontinuous at $z = z_i$. This condition supports a vorticity wave. A deformation η_i of the interface adds vorticity S to the upper layer and removes it from the lower layer, creating a vorticity imbalance in the horizontal direction. This imbalance produces a velocity field which causes the wave to propagate in the horizontal direction. The horizontal component u_i of the perturbation velocity field set up by the interfacial deformation undergoes a jump at the interface, the value of which can be determined from Stokes' Theorem (Appendix 5.3.3):

$$u_i^+ - u_i^- = S\eta_i \tag{2.12}$$

By taking an x derivative of Eq. (2.12) and invoking the continuity relation, we get

$$-\frac{\partial w_i^+}{\partial z} + \frac{\partial w_i^-}{\partial z} = S\frac{\partial \eta_i}{\partial x} \tag{2.13}$$

By substituting Eqs. (2.1) and (2.3) in Eq. (2.13), we obtain

$$\omega_i = -\frac{S}{2}\frac{\sin(\alpha x + \phi_{\eta_i})}{\cos(\alpha x + \phi_{w_i})} = \frac{S}{2\sin(\triangle\phi_{ii})} \tag{2.14}$$

The fact that ω_i is always positive demands

$$\triangle\phi_{ii} = \frac{\pi}{2}\text{sgn}(S) \tag{2.15}$$

where sgn( ) is the sign function. From Eq. (2.14), the intrinsic frequency of a vorticity wave is found to be $-S/2$. The phase-speed c_i can be evaluated by substituting Eq. (2.14) into Eq. (2.10):

$$c_i = U_i - \frac{S}{2\alpha} \tag{2.16}$$

If $S > 0$, the vorticity wave moves to the left relative to the background flow. Alternative derivations of the frequency and phase-speed of a vorticity wave can be found in several references, e.g. Caulfield (1994), Sutherland (2010) or Carpenter *et al.* (2013).

2.2.2 Interfacial internal gravity waves

Interfacial gravity waves exist at a density interface, i.e. regions involving sharp change in density. The most common example of interfacial gravity wave is the surface wave existing at the interface of air and water. Here we will be considering interfacial *internal* gravity waves (hereafter, gravity waves) only. Such waves exist in density stratified flows having a thin density interface (pycnocline). Since most natural water bodies like lakes, estuaries and oceans are density stratified, gravity waves are ubiquitous.

In the case of gravity waves, the intrinsic frequency $-\omega_i \sin(\triangle\phi_{ii})$ can be evaluated by considering the *dynamic condition*. The latter implies that the pressure at the density interface must be continuous. Let the density of upper and lower fluids be ρ_1 and ρ_2 respectively. Then the linearized dynamic condition at the interface after some simplification becomes (Eq. (3.13) of Caulfield (1994)) :

$$\frac{\partial \psi_i}{\partial t} + U_i \frac{\partial \psi_i}{\partial x} = \frac{g^{'}}{2\alpha} \frac{\partial \eta_i}{\partial x} \tag{2.17}$$

Here $g^{'} \equiv g(\rho_2 - \rho_1)/\rho_0$ is the reduced gravity and ρ_0 is the reference density. Under Boussinesq approximation $\rho_0 \approx \rho_1 \approx \rho_2$. By taking an x derivative of Eq. (2.17) and using the streamfunction relation $\{u_i, w_i\} = \{-\partial\psi_i/\partial z,\, \partial\psi_i/\partial x\}$, we get

$$\frac{\partial w_i}{\partial t} + U_i \frac{\partial w_i}{\partial x} = \frac{g^{'}}{2\alpha} \frac{\partial^2 \eta_i}{\partial x^2} \tag{2.18}$$

Substitution of Eqs. (2.1) and (2.3) in Eq. (2.18) yields

$$\begin{aligned} &\dot{A}_{w_i} \cos(\alpha x + \phi_{w_i}) - A_{w_i} \dot{\phi}_{w_i} \sin(\alpha x + \phi_{w_i}) \\ &-\alpha U_i A_{w_i} \sin(\alpha x + \phi_{w_i}) = -\frac{g^{'}\alpha}{2} A_{\eta_i} \cos(\alpha x + \phi_{\eta_i}) \end{aligned} \tag{2.19}$$

The quantity $\dot{\phi}_{w_i} = \dot{\phi}_{\eta_i} = -\sigma = -\alpha c_i$. On substituting this relation in Eq. (2.19), we obtain

$$\omega_i = \frac{g^{'}}{2} \frac{\sin(\triangle\phi_{ii})}{(U_i - c_i)} \tag{2.20}$$

Since ω_i is a positive quantity, Eq. (2.20) demands

$$\triangle\phi_{ii} = \frac{\pi}{2}\text{sgn}(U_i - c_i) \tag{2.21}$$

An important aspect of Eq. (2.20) is that it has been derived independent of the kinematic condition. The presence of single or multiple interfaces does not alter the expression in Eq. (2.20), implying that this equation provides a generalized description of ω_i. Inclusion of kinematic condition yields an expression for ω_i which is simpler but problem specific. For example, when a single interface is present, inclusion of kinematic condition in Eq. (2.20) produces the well known expression for gravity wave frequency. Substituting Eq. (2.8) (this equation has been derived from the kinematic condition for a single interface, i.e. Eq. (2.2)) in Eq. (2.20) and considering only the positive value, we obtain the dispersion relation for gravity waves:

$$\omega_i = \sqrt{\frac{g'\alpha}{2}} \tag{2.22}$$

Moreover Eq. (2.9) requires $|\triangle\phi_{ii}| = \pi/2$. Substituting it along with Eq. (2.20) in Eq. (2.10)) produces the well known expression for the phase-speed of a gravity wave:

$$c_i = U_i \pm \sqrt{\frac{g'}{2\alpha}} \tag{2.23}$$

The above equation shows that each density interface supports two gravity waves, one moving to the left and the other to the right relative to the back-

ground velocity U_i. Alternative approaches to deriving the frequency and phase-speed of a gravity wave can be found in Caulfield (1994); Sutherland (2010); Carpenter *et al.* (2013)).

2.3 Interaction between two linear interfacial waves

Let us now consider a system with two interfaces, one at $z = z_1$ and the other one at $z = z_2$. The linearized kinematic condition at each of these interfaces is then given by:

$$\frac{\partial \eta_1}{\partial t} + U_1 \frac{\partial \eta_1}{\partial x} = w_1 + e^{-\alpha|z_1 - z_2|} w_2 \tag{2.24}$$

$$\frac{\partial \eta_2}{\partial t} + U_2 \frac{\partial \eta_2}{\partial x} = e^{-\alpha|z_1 - z_2|} w_1 + w_2 \tag{2.25}$$

It has been implicitly assumed that both waves have the same wavenumber. The R.H.S. of Eqs. (2.24)-(2.25) reveal the subtle effect of wave interaction, and can be understood as follows. The effect of w_1 extends away from the interface z_1, hence it can be felt by a wave existing at another location, say z_2. Therefore the vertical velocity of the wave at z_2 gets modified - it becomes the linear superposition of its own vertical velocity w_2 and the component of w_1 existing at z_2. This phenomenon is also known as "action-at-a-distance", see Heifetz & Methven (2005).

On substituting Eqs. (2.1) and (2.3) in Eqs. (2.24)-(2.25), we get

$$\dot{A}_{\eta_1}\cos\left(\alpha x+\phi_{\eta_1}\right)-A_{\eta_1}\left(\alpha U_1+\dot{\phi}_{\eta_1}\right)\sin\left(\alpha x+\phi_{\eta_1}\right)= \\ A_{w_1}\cos\left(\alpha x+\phi_{w_1}\right)+e^{-\alpha|z_1-z_2|}A_{w_2}\cos\left(\alpha x+\phi_{w_2}\right) \tag{2.26}$$

$$\dot{A}_{\eta_2}\cos\left(\alpha x+\phi_{\eta_2}\right)-A_{\eta_2}\left(\alpha U_2+\dot{\phi}_{\eta_2}\right)\sin\left(\alpha x+\phi_{\eta_2}\right)= \\ e^{-\alpha|z_1-z_2|}A_{w_1}\cos\left(\alpha x+\phi_{w_1}\right)+A_{w_2}\cos\left(\alpha x+\phi_{w_2}\right) \tag{2.27}$$

Proceeding in a manner similar to §2.2, the growth rate γ_i and phase-speed c_i of each wave is found to be

$$\gamma_1=\frac{A_{w_1}}{A_{\eta_1}}\cos\left(\triangle\phi_{11}\right)+\frac{A_{w_2}}{A_{\eta_1}}e^{-\alpha|z_1-z_2|}\cos\left(\triangle\phi_{12}\right) \tag{2.28}$$

$$c_1=U_1-\frac{1}{\alpha}\left[\frac{A_{w_1}}{A_{\eta_1}}\sin\left(\triangle\phi_{11}\right)+\frac{A_{w_2}}{A_{\eta_1}}e^{-\alpha|z_1-z_2|}\sin\left(\triangle\phi_{12}\right)\right] \tag{2.29}$$

$$\gamma_2=\frac{A_{w_2}}{A_{\eta_2}}\cos\left(\triangle\phi_{22}\right)+\frac{A_{w_1}}{A_{\eta_2}}e^{-\alpha|z_1-z_2|}\cos\left(\triangle\phi_{21}\right) \tag{2.30}$$

$$c_2=U_2-\frac{1}{\alpha}\left[\frac{A_{w_2}}{A_{\eta_2}}\sin\left(\triangle\phi_{22}\right)+\frac{A_{w_1}}{A_{\eta_2}}e^{-\alpha|z_1-z_2|}\sin\left(\triangle\phi_{21}\right)\right] \tag{2.31}$$

Here $\triangle\phi_{ij}\equiv\phi_{w_j}-\phi_{\eta_i}$. When $\alpha\left|z_1-z_2\right|\to\infty$, the two waves decouple, and we recover Eqs. (2.9)-(2.10) for each wave. As argued in §2.2, a wave in isolation cannot grow or decay on its own. Therefore, the first term in each of Eq. (2.28) and Eq. (2.30) should be equal to zero, implying $|\triangle\phi_{ii}|=\pi/2$.

In all our analyses, we will be considering a system with a *left moving top wave* ($\triangle\phi_{11}=\pi/2$) and a *right moving bottom wave* ($\triangle\phi_{22}=-\pi/2$), the wave motion being relative to the background velocity at the corresponding

interface. Let the phase shift between the bottom and top waves be $\Phi \equiv \phi_{\eta_2} - \phi_{\eta_1}$. Therefore $\triangle\phi_{12} = \Phi - \pi/2$ and $\triangle\phi_{21} = \pi/2 - \Phi$. Defining amplitude ratio $R \equiv A_{\eta_1}/A_{\eta_2}$, we re-write Eqs. (2.28)-(2.31) to obtain

$$\gamma_1 = \frac{\omega_2}{R} e^{-\alpha|z_1 - z_2|} \sin\Phi \tag{2.32}$$

$$c_1 = U_1 - \frac{1}{\alpha}\left[\omega_1 - \frac{\omega_2}{R} e^{-\alpha|z_1 - z_2|} \cos\Phi\right] \tag{2.33}$$

$$\gamma_2 = R\omega_1 e^{-\alpha|z_1 - z_2|} \sin\Phi \tag{2.34}$$

$$c_2 = U_2 + \frac{1}{\alpha}\left[\omega_2 - R\omega_1 e^{-\alpha|z_1 - z_2|} \cos\Phi\right] \tag{2.35}$$

Eqs. (2.32)-(2.35) describe the linear hydrodynamic stability of the system. Unlike the conventional linear stability analysis, we did not impose normal-mode type perturbations (they only account for exponentially growing instabilities) in our derivation. Therefore the equation set provides a *non-modal* description of hydrodynamic stability in idealized (multi-layered) shear flows. We refer to this theory as the "wave interaction theory (WIT)". WIT is only applicable to those hydrodynamic stability problems where the discrete spectrum dynamics is of interest and the continuous spectrum can be neglected. A schematic description of the process of wave interaction is illustrated in Fig. 2.1.

Subtracting Eq. (2.34) from Eq. (2.32) and Eq. (2.35) from Eq. (2.33), we

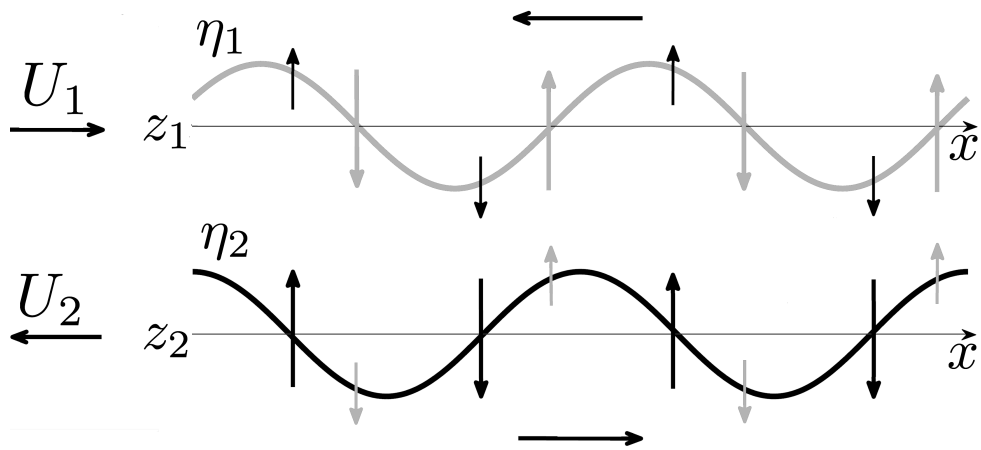

Figure 2.1: Schematic of the interfacial wave interaction mechanism. The deformation and associated vertical velocity of each wave is shown by the same color. Interaction imposes an additional vertical velocity (shown by different color). The horizontal arrow associated with a wave indicates the intrinsic wave propagation direction. Both the waves are counter-propagating (move against the background velocity at that location).

find

$$\frac{dR}{dt} = R\left(\gamma_1 - \gamma_2\right) = \left(\omega_2 - R^2\omega_1\right) e^{-\alpha|z_1 - z_2|} \sin\Phi \tag{2.36}$$

$$\frac{d\Phi}{dt} = \alpha\left(c_1 - c_2\right) = \alpha\left(U_1 - U_2\right) - \left[\omega_1 + \omega_2 - \left(R\omega_1 + \frac{\omega_2}{R}\right) e^{-\alpha|z_1 - z_2|} \cos\Phi\right] \tag{2.37}$$

The two parameters have the following range of values: $R \in (0, \infty)$ and $\Phi \in [-\pi, \pi]$. Eqs. (2.36)-(2.37) represent a two dimensional, autonomous, non-linear dynamical system. The *two* equilibrium points of the system, found by imposing the conditions $dR/dt = 0$ in Eq. (2.36) and $d\Phi/dt = 0$ in Eq. (2.37),

are given by

$$(R,\,\Phi) = (R_{NM}, \Phi_{NM}) \;\text{ and }\; (R_{NM}, -\Phi_{NM}) \tag{2.38}$$

where

$$R_{NM} = \sqrt{\frac{\omega_2}{\omega_1}} \tag{2.39}$$

$$\Phi_{NM} = \pm\cos^{-1}\left[\left\{\frac{\omega_1 + \omega_2 - \alpha\left(U_1 - U_2\right)}{2\sqrt{\omega_1\omega_2}}\right\} e^{\alpha|z_1 - z_2|}\right] \tag{2.40}$$

Eq. (2.40) reveals that the equilibrium points exist only if

$$\left|\left\{\frac{\omega_1 + \omega_2 - \alpha\left(U_1 - U_2\right)}{2\sqrt{\omega_1\omega_2}}\right\} e^{\alpha|z_1 - z_2|}\right| \leq 1 \tag{2.41}$$

The linear behavior of the dynamical system around the equilibrium points is of interest. To understand this behavior, we evaluate the Jacobian matrix, $\mathcal{J}$ at the equilibrium points:

$$\mathcal{J}\left(R_{NM}, \pm\Phi_{NM}\right) = -2\sqrt{\omega_1\omega_2}e^{-\alpha|z_1 - z_2|}\begin{bmatrix} \sin\left(\pm\Phi_{NM}\right) & 0 \\ 0 & \sin\left(\pm\Phi_{NM}\right) \end{bmatrix} \tag{2.42}$$

Eq. (2.42) shows that the two eigenvalues corresponding to each equilibrium point are equal. Further analysis reveals that every vector at the equilibrium point is an eigenvector. The equilibrium point (R_{NM}, Φ_{NM}) produces negative eigenvalues, while the eigenvalues corresponding to $(R_{NM}, -\Phi_{NM})$ are

positive. Hence the dynamical system represented by Eqs. (2.36)-(2.37) is of "source-sink" type. In terms of the classical normal-mode analysis, each equilibrium point corresponds to a normal-mode of the discrete spectrum - (R_{NM}, Φ_{NM}) corresponds to the growing normal-mode (signifying exponential growth) and $(R_{NM}, -\Phi_{NM})$ corresponds to the decaying normal-mode (signifying exponential decay). Normal-mode type instabilities can exist only if the condition in Eq. (2.41) is satisfied. Therefore Eq. (2.41) denotes the condition for exponentially growing instabilities in idealized, homogeneous and stratified shear layers.

WIT allows understanding hydrodynamic instability from two different perspectives - wave interaction and dynamical systems. According to the former, exponentially growing instabilities signify resonant interaction between the two waves. From dynamical systems point of view, resonance implies "equilibrium condition" ($d\Phi/dt = 0$ and $dR/dt = 0$). Wave interaction interpretation of each of the two components of the equilibrium condition are as follows:

(a) *Phase-Locking*: Reduction in the phase-speed of each wave occurs through the interaction mechanism - the vertical velocity field produced by the distant wave acts so as to diminish the phase-speed of the given wave. Furthermore, if the waves are "counter-propagating" (meaning, the direction of the intrinsic phase-speed, $-\boldsymbol{\omega}_i \sin(\triangle\phi_{ii})/\alpha$, is opposite to the background flow), the background flow causes an additional reduction in the phase-speed. Both wave interaction and counter-propagation work in tandem until the two waves

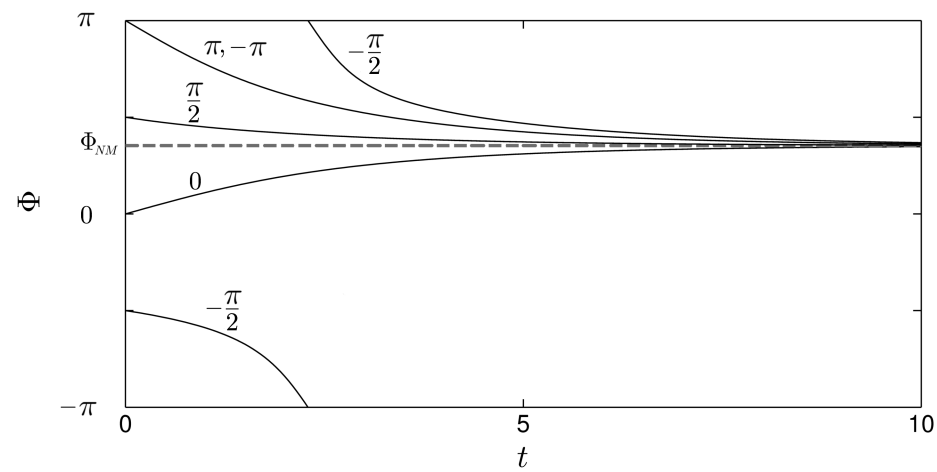

(a)

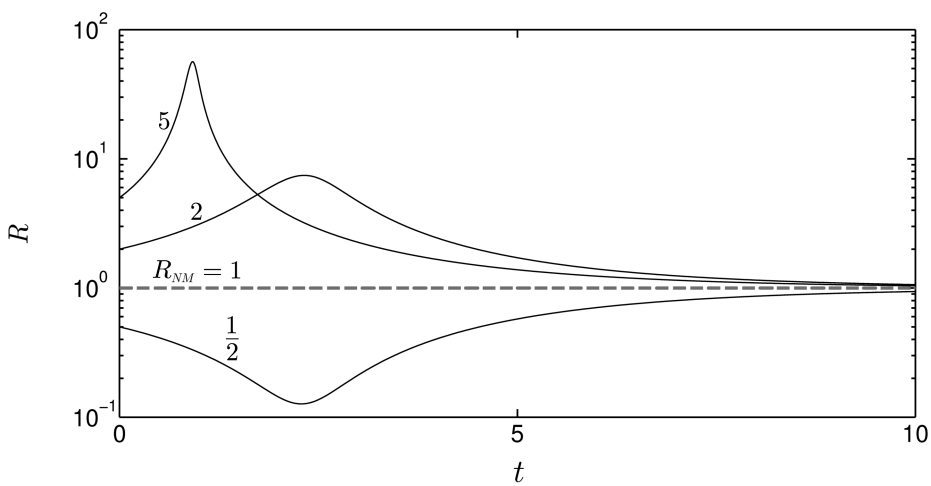

(b)

Figure 2.2: The figure shows that any initial condition (R_0, Φ_0) finally yields the resonant configuration (R_{NM}, Φ_{NM}), provided Eq. (2.41) is satisfied. The case depicted here is Kelvin-Helmholtz instability (interaction between two vorticity waves) corresponding to $\alpha = 0.4$. Any other shear instability will show qualitatively similar characteristics. (a) Φ versus t corresponding to $\Phi_0 = -\pi, -\pi/2, 0, \Phi_{NM}, \pi/2$ and π. The value of R_0 is held constant, and is equal to 2. (b) R versus t corresponding to $R_0 = 1/2, 1(R_{NM}), 2$ and 5. The value of Φ_0 is held constant, and is equal to $-\pi/2$.

"phase-lock", i.e. they are stationary relative to each other. In other words, this means $d\Phi/dt = 0$.

(b) *Mutual Growth*: The phase shift at the phase-locked state, Φ_{NM}, is a unique angle producing the resonant configuration. This configuration causes the two waves to grow equally (i.e. $\gamma_1 = \gamma_2$) via interaction. Eq. (2.36) shows that equal growth rate implies $dR/dt = 0$. Furthermore, Eqs. (2.32) and (2.34) imply $\gamma_1 = \gamma_2 =$ constant, meaning that the wave amplitudes grow at an exponential rate[3]. This exponential growth explains why the equilibrium point (R_{NM}, Φ_{NM}) corresponds to the growing normal-mode of the discrete spectrum.

WIT shows that the individual waves grow when $0 \leq \Phi \leq \pi$ and decay when $-\pi \leq \Phi \leq 0$. The largest possible growth, also known as the *optimal growth*, occurs when $\Phi = \pi/2$. These results are in accordance with the analysis of Heifetz & Methven (2005). Using the Generalized stability theory of Farrell & Ioannou (1996), Heifetz & Methven (2005) showed that the optimal growth in a barotropic shear layer occurs when the two counter-propagating Rossby waves are in quadrature.

WIT also reveals that the left moving top wave and the right moving bottom wave eventually phase-lock (which then leads to mutual growth), provided the condition in Eq. (2.41) is satisfied. *Any* arbitrary initial condition

[3]There are systems where phase-locking does not produce exponential growth. For example, *stable* barotropic and baroclinic modes result from the phase-locking between deep water surface gravity and internal gravity waves; see Chapter 7 of Kundu & Cohen (2004), Pg. 259-261. Shear is always absent in such systems.

(say $R = R_0$ and $\Phi = \Phi_0$) finally leads to phase-locking, and is evident from Fig. 2.2. As mentioned already, Eqs. (2.32)-(2.37) describe the non-modal instability process. Non-modal instability signifies non-orthogonal interaction between the two wave modes, and is the entire process occurring prior to the phase-locking event. Phase-locking is the final or steady state configuration, and corresponds to the the growing normal-mode (R_{NM}, Φ_{NM}) of the discrete spectrum. The fact that Φ_{NM} signifies the growing normal-mode configuration implies $0 \leq \Phi_{NM} \leq \pi$.

A misconception might arise for phase shifts in the range $-\pi \leq \Phi \leq 0$. In this case, the reader might form an impression that the instability will not appear (because both the waves are decaying according to Eqs. (2.32) and (2.34)). However, the wave decay process is temporary. The two waves continuously adjust Φ so as to enter the growing zone $0 \leq \Phi \leq \pi$. After reaching this zone, the two waves still continue to adjust Φ until the steady-state value (i.e. the resonant configuration), Φ_{NM}, is reached. This fact can be better understood by considering the case $\Phi_0 = -\pi/2$ in Fig. 2.2(a). Although initially $-\pi \leq \Phi \leq 0$, the value of Φ eventually enters the growing range and finally attains the steady-state value.

2.4 Homogeneous and stratified shear instabilities

2.4.1 The Kelvin-Helmholtz instability

Let us consider a piecewise linear velocity profile

$$U(z) = \begin{cases} U_1 & z \geq z_1 \\ Sz & z_2 \leq z \leq z_1 \\ U_2 & z \leq z_2 \end{cases} \tag{2.43}$$

This profile is a prototype of barotropic shear layers occurring in many geophysical and astrophysical flows, see Chapter 3. It supports two vorticity waves, one at z_1 and the other at z_2. The shear $S = (U_1 - U_2)/(z_1 - z_2)$. We non-dimensionalize the problem by choosing a length scale $h = (z_1 - z_2)/2$ and a velocity scale $\Delta U = (U_1 - U_2)/2$. In a reference frame moving with the mean flow $\bar{U} = (U_1 + U_2)/2$, the non-dimensional velocity profile becomes

$$U(z) = \begin{cases} 1 & z \geq 1 \\ z & -1 \leq z \leq 1 \\ -1 & z \leq -1 \end{cases} \tag{2.44}$$

where both U and z are now non-dimensional quantities. This profile, along with the vorticity waves, is shown in Fig. 2.3(a). The top wave is left moving

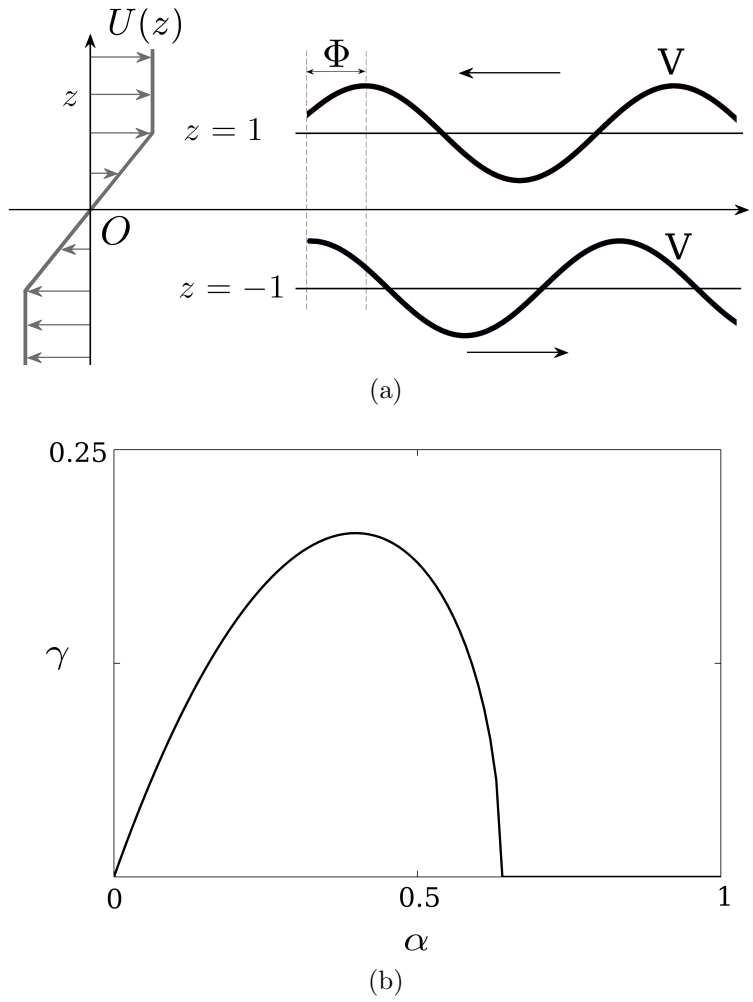

Figure 2.3: (a) The setting leading to the Kelvin-Helmholtz instability. The velocity profile in Eq. (2.44) is shown on the left, while the vorticity waves (marked by "V") are shown on the right. (b) Linear stability diagram of the Kelvin-Helmholtz instability (γ denotes the modal growth rate).

while the bottom wave is right moving. Both the waves counter-propagate, i.e. move in a direction opposite to the background flow. The wave interaction and subsequent instability mechanism can be understood from WIT, see §2.3.

The classical normal-mode based linear stability analysis of the profile in Eq. (2.44) was first performed by Rayleigh (1880). He showed that if the non-dimensional wavenumber α is in the range $0 \leq \alpha \leq 0.64$, the flow is unstable; see Fig. 2.3(b). Thus, the piecewise linear profile and the ensuing instability are often referred to as the "Rayleigh's shear layer" and "Rayleigh's shear instability" respectively. However we will address the latter as the "Kelvin-Helmholtz instability (KH)", following the wider acceptance of this terminology in the stratified shear layer community (Carpenter *et al.*, 2013). The non-modal analysis of the piecewise linear profile was performed in detail by Heifetz *et al.* (1999); Heifetz & Methven (2005). Following the footsteps of Bretherton (1966) and Hoskins *et al.* (1985), Heifetz and co-authors were able to put forward a comprehensive mechanistic picture of KH (in rotating frame) in terms of counter-propagating Rossby wave interactions. By using the Generalized Stability Theory (Farrell & Ioannou, 1996), Heifetz & Methven (2005) showed how wave interaction leads to optimal growth in shear layers.

Here we study the KH problem in terms of WIT, i.e. Eqs. (2.32)-(2.35). Since the two waves involved in the KH problem are vorticity waves, we substitute Eq. (2.14) in the WIT equation-set and after non-dimensionalization

we obtain

$$\gamma_1 = \frac{1}{2R} e^{-2\alpha} \sin \Phi \tag{2.45}$$

$$c_1 = 1 - \frac{1}{2\alpha} \left[1 - \frac{1}{R} e^{-2\alpha} \cos \Phi \right] \tag{2.46}$$

$$\gamma_2 = \frac{R}{2} e^{-2\alpha} \sin \Phi \tag{2.47}$$

$$c_2 = -1 + \frac{1}{2\alpha} \left[1 - R e^{-2\alpha} \cos \Phi \right] \tag{2.48}$$

Eqs. (2.45)-(2.48) are isomorphic to Eqs. (14a)-(14d) of Heifetz *et al.* (1999) and homomorphic to Eqs. (7a)-(7d) of Davies & Bishop (1994). These two referenced equation-sets describe edge wave interactions in two different types of rotating physical systems. While the one described by Heifetz *et al.* (1999) shows how CRW interactions lead to barotropic shear instability, the equation-set formulated by Davies & Bishop (1994) shows how baroclinic instability is produced through the interaction of temperature edge waves of the Eady model. Furthermore, Heifetz *et al.* (1999) showed that their set of equations is homomorphic to that of Davies & Bishop (1994).

Eqs. (2.45)-(2.48) demonstrate how wave interaction causes amplitude growth and phase-speed modification of the individual vorticity waves, thereby leading to KH. The fact that the wave interaction modifies the phase-speed of a vorticity wave can be understood by comparing Eq. (2.46) and Eq. (2.48) with the non-dimensional form of Eq. (2.16) (non-dimensionalization means substituting $S = 1$ and $U_i = 1$ or -1 in Eq. (2.16)).

The generalized non-linear dynamical system given by Eqs. (2.36)-(2.37) in this case translates to

$$\frac{dR}{dt} = \frac{1}{2}\left(1 - R^2\right) e^{-2\alpha} \sin\Phi \tag{2.49}$$

$$\frac{d\Phi}{dt} = (2\alpha - 1) + \frac{1}{2}\left(R + \frac{1}{R}\right) e^{-2\alpha} \cos\Phi \tag{2.50}$$

The equilibrium points of this system are $(R_{NM}, \pm\Phi_{NM})$, where

$$R_{NM} = 1 \tag{2.51}$$

$$\Phi_{NM} = \cos^{-1}\left[(1 - 2\alpha)\, e^{2\alpha}\right] \tag{2.52}$$

The phase portrait is shown in Fig. 2.4. It confirms that the dynamical system is indeed of source-sink type, as predicted in §2.3. When the interaction between the two waves is weak, the waves do not reach the resonant configuration, hence exponentially growing instability is never produced. The resulting dynamical system only produces periodic orbits; see Fig. 2.5.

The necessary and sufficient condition for instability expressed via Eq. (2.41) in this case translates to

$$-1 \leq (1 - 2\alpha)\, e^{2\alpha} \leq 1 \quad \text{implying} \quad 0 \leq \alpha \leq 0.64 \tag{2.53}$$

The range of unstable wavenumbers obtained from the above equation corroborates Rayleigh's normal-mode analysis.

Rayleigh also found the wavenumber of maximum growth (also known as

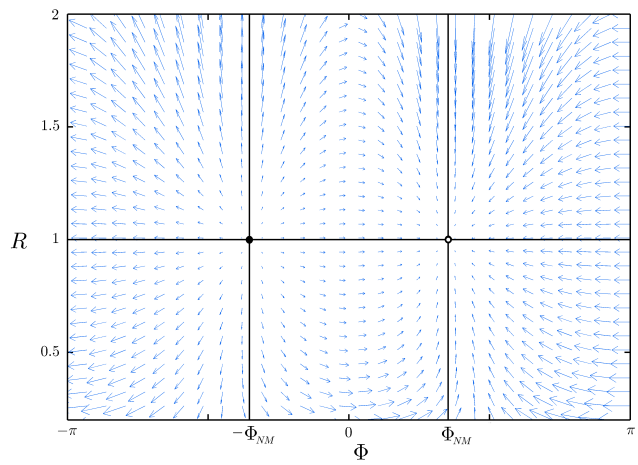

Figure 2.4: Phase portrait of Kelvin-Helmholtz instability corresponding to $\alpha = 0.4$. The system has two equilibrium points - one unstable ($\circ$) and the other stable ($\bullet$). Φ is the phase difference between the lower and upper waves, while R represents the ratio of the upper wave amplitude to the lower wave amplitude.

the critical wavenumber) to be $\alpha_{crit} = 0.4$. This value can be verified through WIT by imposing the normal-mode condition and maximizing γ_1 or γ_2 with respect to α.

The fact that KH develops into a standing wave instability can be verified by applying the normal-mode condition in Eqs. (2.46) and (2.48). Performing the necessary steps we find $c_1 = c_2 = 0$, i.e. the waves have become stationary after phase-locking. In this configuration, the waves start to grow exponentially. Hence the shear layer grows in size. The growth process eventually becomes non-linear, and as shown in Chapter 3, the shear layer modifies into elliptical patches of constant vorticity.

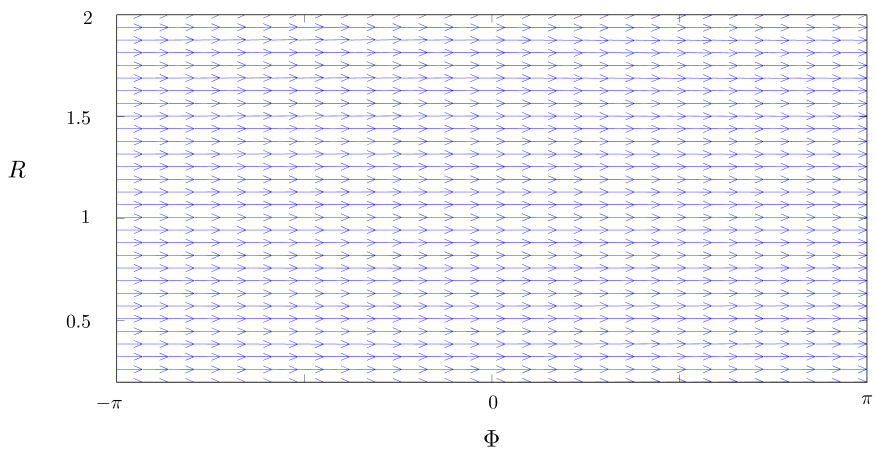

Figure 2.5: Phase portrait when the two interacting vorticity waves do not produce KH ($\alpha = 2$).

2.4.2 The Taylor instability

Let us consider a uniform shear layer with two density interfaces

$$U(z) = Sz \quad \text{and} \quad \rho(z) = \begin{cases} \rho_0 - \frac{\Delta\rho}{2} & z \geq z_1 \\ \rho_0 & z_2 \leq z \leq z_1 \\ \rho_0 + \frac{\Delta\rho}{2} & z \leq z_2 \end{cases} \tag{2.54}$$

The shear S is constant. We choose $\Delta\rho/2$ as the density scale, $h = (z_1 - z_2)/2$ as the length scale, and thereby non-dimensionalize Eq. (2.54). The physical state of the system is determined by the competition between the density stratification and the shear, the non-dimensional measure of which is given by the Bulk Richardson number $J = g^{'}/(hS^2)$, where $g^{'} = g(\Delta\rho/2)/\rho_0$ is the reduced gravity, and ρ_0 is the reference density. The dimensionless velocity

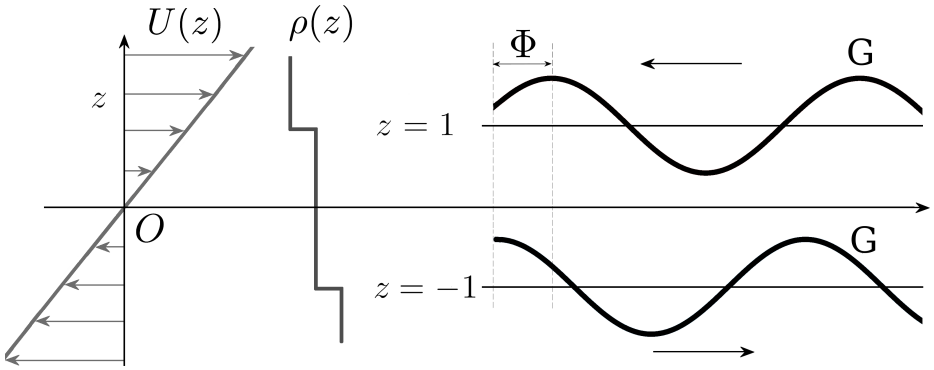

(a)

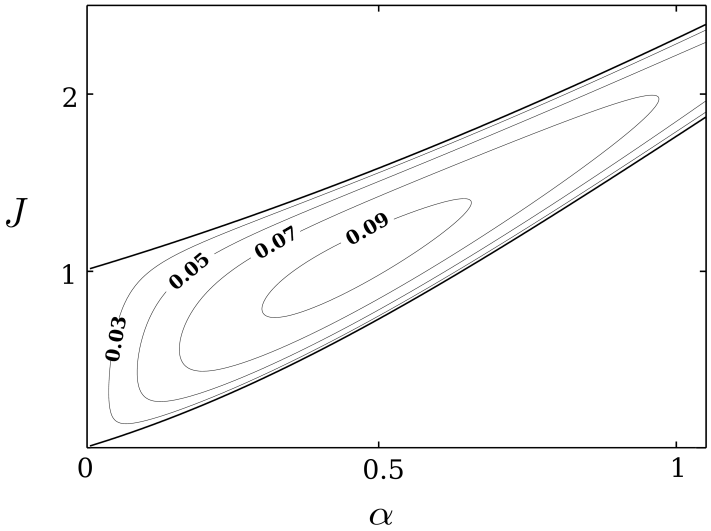

(b)

Figure 2.6: (a) The setting leading to the Taylor instability. The velocity and density profiles in Eq. (2.55) are shown on the left, while the gravity waves "G" are shown on the right. (b) Linear stability diagram of the Taylor instability. The contours represent the growth rate.

and density profiles therefore become

$$U(z) = z \quad \text{and} \quad \rho(z) = \begin{cases} -1 & z \geq 1 \\ 0 & -1 \leq z \leq 1 \\ 1 & z \leq -1 \end{cases} \tag{2.55}$$

This flow configuration is shown in Fig. 2.6(a). Contrary to the conventional notion that gravitationally stable density stratified flows are usually stable, Taylor (1931) put forward the flow given by Eq. (2.55) and showed it to be linearly unstable. The interplay between the background shear and the gravity waves existing at the density interfaces produce the destabilizing effect. The ensuing instability is thus known as the "Taylor instability". Taylor found that for each value of J, there exists a band of unstable wavenumbers (and vice-versa), shown in Fig. 2.6(b). This unstable range is given by (see Eq. (2.154) of Sutherland (2010))

$$\frac{2\alpha}{1+e^{-2\alpha}} \leq J \leq \frac{2\alpha}{1-e^{-2\alpha}} \tag{2.56}$$

Caulfield (1994), and more recently Carpenter *et al.* (2013), have described Taylor instability in terms of wave interactions. As discussed in §2.2.2, each density interface (located at $z = 1$ and $z = -1$) supports two gravity waves. The interaction between the left moving gravity wave at the upper interface and right moving gravity wave at the lower interface leads to Taylor instability.

To understand Taylor instability in terms of WIT, we substitute Eq. (2.20) in Eqs. (2.32)-(2.35). After non-dimensionalization and some algebra, we obtain

$$\gamma_1 = \frac{J}{2R(1+c_2)} e^{-2\alpha} \sin\Phi \tag{2.57}$$

$$c_1 = 1 - \sqrt{\frac{J}{2\alpha}\left(1 - \frac{\beta}{R} e^{-2\alpha}\cos\Phi\right)} \tag{2.58}$$

$$\gamma_2 = \frac{JR}{2(1-c_1)} e^{-2\alpha} \sin\Phi \tag{2.59}$$

$$c_2 = -1 + \sqrt{\frac{J}{2\alpha}\left(1 - \frac{R}{\beta} e^{-2\alpha}\cos\Phi\right)} \tag{2.60}$$

Here $\beta = \omega_2/\omega_1 = (1-c_1)/(1+c_2)$, and by definition is a positive quantity. From Eqs. (2.58) and (2.60) we construct a quadratic equation for β:

$$\beta^2 + \beta e^{-2\alpha}\cos\Phi\left(\frac{1}{R} - R\right) - 1 = 0 \tag{2.61}$$

Of the two roots, only the positive one is relevant.

The coupled nature of Eqs. (2.58) and (2.60) makes it more complicated than the KH problem. The non-linear dynamical system in this case is given by

$$\frac{dR}{dt} = \frac{J}{2}\left(\frac{1}{1+c_2} - \frac{R^2}{1-c_1}\right) e^{-2\alpha}\sin\Phi \tag{2.62}$$

$$\frac{d\Phi}{dt} = 2\alpha - \sqrt{\frac{J\alpha}{2}\left(1 - \frac{\beta}{R} e^{-2\alpha}\cos\Phi\right)} - \sqrt{\frac{J\alpha}{2}\left(1 - \frac{R}{\beta} e^{-2\alpha}\cos\Phi\right)} \tag{2.63}$$

At phase-locking $R = R_{NM} = \sqrt{\beta}$. Substituting this value in Eq. (2.61) gives $\beta = 1$. Therefore $R_{NM} = 1$ and $c_1 = c_2 = 0$ at resonance. This implies that Taylor instability, like KH, also evolves into a standing wave instability. Although this fact is previously known, WIT demonstrates why this is the case. The non-linear structure of Taylor instability is similar to KH. Caulfield *et al.* (1995) has experimentally shown that this instability evolves into standing billows.

The phase-shift Φ_{NM} is evaluated from Eq. (2.63):

$$\Phi_{NM} = \cos^{-1}\left[\left(1 - \frac{2\alpha}{J}\right) e^{2\alpha}\right] \tag{2.64}$$

The condition for Taylor instability is given by

$$-1 \leq \left(1 - \frac{2\alpha}{J}\right) e^{2\alpha} \leq 1 \quad \text{implying} \quad \frac{2\alpha}{1 + e^{-2\alpha}} \leq J \leq \frac{2\alpha}{1 - e^{-2\alpha}} \tag{2.65}$$

The latter result corroborates the classical normal-mode result given in Eq. (2.56).

2.4.3 The Holmboe instability

Let us consider the following velocity and density profiles

$$U(z) = \begin{cases} U_1 & z \geq z_1 \\ Sz & z \leq z_1 \end{cases} \quad \text{and} \quad \rho(z) = \begin{cases} \rho_0 & z \geq z_2 \\ \rho_0 + \triangle\rho & z \leq z_2 \end{cases} \tag{2.66}$$

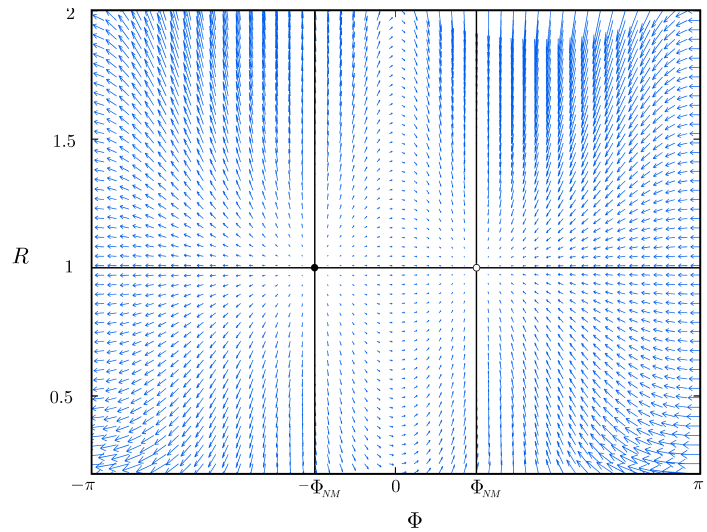

Figure 2.7: Phase portrait of Taylor instability corresponding to an unstable combination of α and J. Here $\alpha = 0.2$ and $J = 0.7264$.

We non-dimensionalize Eq. (2.66) exactly like the Taylor problem, which gives us the dimensionless velocity and density profiles:

$$U(z) = \begin{cases} 1 & z \geq 1 \\ z & z \leq 1 \end{cases} \quad \text{and} \quad \rho(z) = \begin{cases} 0 & z \geq 0 \\ 2 & z \leq 0 \end{cases} \tag{2.67}$$

The vorticity interface at the top supports a vorticity wave, while the density interface at the bottom supports two gravity waves. The interaction between the left moving vorticity wave at the upper interface and the right moving gravity wave at the lower interface leads to an instability mechanism, known as the "Holmboe instability". The corresponding flow setting is shown in Fig. 2.8(a).

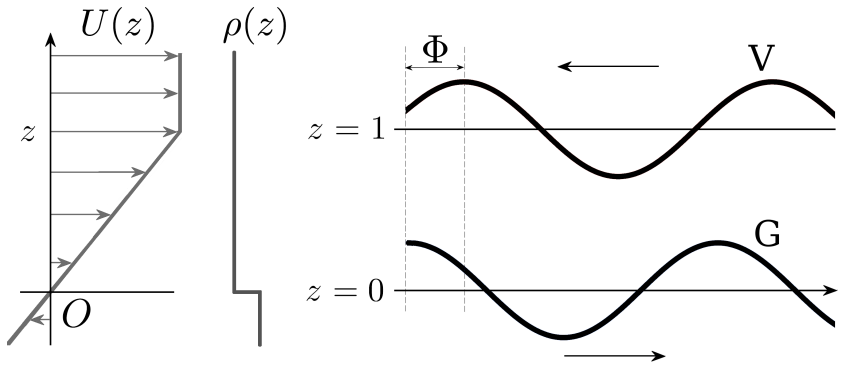

(a)

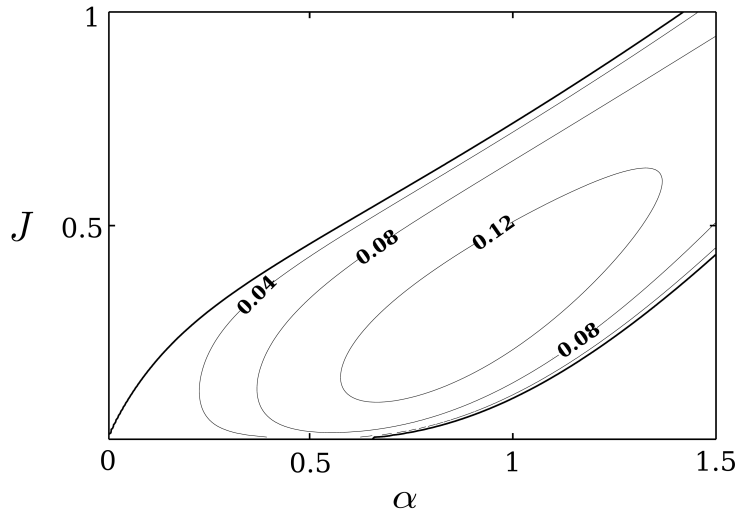

(b)

Figure 2.8: (a) The setting leading to the Holmboe instability. The velocity and density profiles in Eq. (2.67) are shown on the left, while the vorticity wave "V" and the gravity wave "G" are shown on the right. (b) Linear stability diagram of the Holmboe instability. The contours represent the growth rate.

Holmboe (1962) was the first to consider the instability mechanism resulting from the interaction between vorticity and gravity waves. In his actual problem, Holmboe considered a flow setting more complicated than Eq. (2.67). His problem consisted of a velocity profile given by Eq. (2.44), however the density profile is the same as that in Eq. (2.67). Holmboe performed a linear stability analysis and showed that in addition to the conventional KH mode, there is another mode of instability - the Holmboe mode. Unlike the KH mode, the Holmboe mode is characterized by traveling waves. Presence of this unstable mode reveals that stable density stratification can also have a destabilizing influence. This aspect of Holmboe instability is much like the Taylor instability. Recent non-modal analysis by Constantinou & Ioannou (2011) has shown that Holmboe instability is susceptible to substantial transient growths. Such growths especially occur for parameter values for which there is no instability but are close to the stability boundary.

Analyzing the "authentic" Holmboe instability in terms of WIT implies considering the interaction of three waves - two vorticity waves and a gravity wave. An extended version of WIT can handle this problem, however this will not be considered in this work[4]. Baines & Mitsudera (1994) simplified Holmboe's problem by introducing the profile in Eq. (2.67). This allows studying the interaction of a vorticity and a gravity wave, and is therefore suitable for this work. Linear stability analysis shows that corresponding to each value of

[4]Stratified shear layer instabilities resulting from the interaction of multiple waves have been addressed by Caulfield (1994), however he limited his study to the normal-mode waveform.

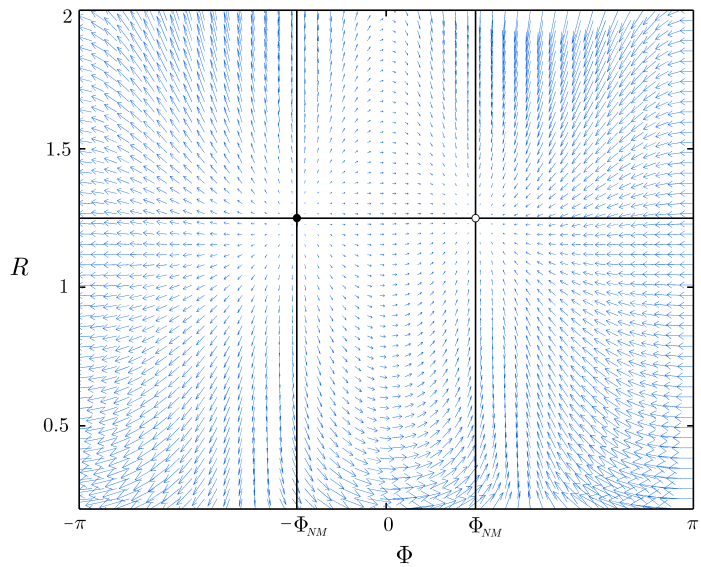

Figure 2.9: Phase portrait of Holmboe instability corresponding to $\alpha = 1$ and $J = 0.5$.

J, there exists a band of unstable wavenumbers. This is shown in Fig. 2.8(b). The stability boundary has been evaluated in Appendix 5.3.3.

In order to understand Holmboe instability in terms of WIT, we substitute Eq. (2.14) and Eq. (2.20) in Eqs. (2.32)-(2.35). After performing non-dimensionalization and some algebra, we obtain

$$\gamma_1 = \frac{J}{Rc_2} e^{-\alpha} \sin \Phi \tag{2.68}$$

$$c_1 = 1 - \frac{1}{\alpha} \left(\frac{1}{2} - \frac{J}{Rc_2} e^{-\alpha} \cos \Phi \right) \tag{2.69}$$

$$\gamma_2 = \frac{R}{2} e^{-\alpha} \sin \Phi \tag{2.70}$$

$$c_2 = \frac{1}{4\alpha} \left(-Re^{-\alpha} \cos \Phi + \sqrt{R^2 e^{-2\alpha} \cos^2 \Phi + 16\alpha J} \right) \tag{2.71}$$

Like the Taylor case, this equation-set is also of coupled type. The non-linear dynamical system in this case is given by:

$$\frac{dR}{dt} = \left(\frac{4\alpha J}{-Re^{-\alpha}\cos\Phi + \sqrt{R^2 e^{-2\alpha}\cos^2\Phi + 16\alpha J}} - \frac{R^2}{2} \right) e^{-\alpha}\sin\Phi \tag{2.72}$$

$$\frac{d\Phi}{dt} = \alpha - \frac{1}{2}\left(1 - Re^{-\alpha}\cos\Phi\right) + \frac{4\alpha J}{-Re^{-\alpha}\cos\Phi + \sqrt{R^2 e^{-2\alpha}\cos^2\Phi + 16\alpha J}} \left(\frac{e^{-\alpha}\cos\Phi}{R} - 1 \right) \tag{2.73}$$

The equilibrium points of this system are $(R_{NM}, \pm\Phi_{NM})$, where

$$R_{NM} = \sqrt{\frac{1 - 2\alpha + \sqrt{32\alpha J + (1-2\alpha)^2}}{2}} \tag{2.74}$$

$$\Phi_{NM} = \cos^{-1}\left[\left(\frac{R_{NM}^2 + 1 - 2\alpha}{2R_{NM}} \right) e^{\alpha} \right] \tag{2.75}$$

The condition for Holmboe instability is found to be

$$-1 \leq \left(\frac{R_{NM}^2 + 1 - 2\alpha}{2R_{NM}} \right) e^{\alpha} \leq 1 \tag{2.76}$$

This provides the range of J leading to Holmboe instability, and is as follows:

$$\frac{1}{2A}\left(-B - \sqrt{B^2 - 4AC}\right) \leq J \leq \frac{1}{2A}\left(-B + \sqrt{B^2 - 4AC}\right) \tag{2.77}$$

where

$$A = 16\alpha^2$$

$$B = -\alpha\left[8\left(2\alpha-1\right)^2 + 36\left(2\alpha-1\right)e^{-2\alpha} + 27e^{-4\alpha}\right]$$

$$C = \left(2\alpha - 1 + e^{-2\alpha}\right)\left(2\alpha-1\right)^3$$

Eq. (2.77) corroborates the normal-mode result given in Appendix 5.3.3.

The phase portrait of Holmboe instability, corresponding to an unstable combination of α and J, is shown in Fig. 2.9. This phase portrait is slightly different from Taylor and KH, because $R_{NM} \neq 1$ in this case. Another feature of Holmboe instability is that, unlike Taylor and KH cases, its phase-speed is non-zero at the equilibrium condition. This phase-speed is found to be

$$c_1 = c_2 = \frac{2J}{R_{NM}^2} = \frac{4J}{1 - 2\alpha + \sqrt{32\alpha J + \left(1-2\alpha\right)^2}} \tag{2.78}$$

In the limit of large α and J, the two phase-locked waves move with unit speed to the right.

2.5 Conclusion

This chapter is devoted to investigating the wave interaction problem in a generalized sense. The governing equations of hydrodynamic instability in homogeneous and stratified shear layers have been derived *without* imposing the

wave type, or the normal-mode waveform. We refer to this equation-set as the "wave interaction theory (WIT)". Using WIT we have shown in Fig. 2.2 that two counter-propagating linear interfacial waves, having arbitrary initial amplitudes and phases, eventually *resonates*, provided they satisfy the condition for resonant interaction (Eq. (2.41)). Resonance makes the interfacial waves, and therefore the shear layer, to grow at an exponential rate - leading to the normal-mode instability. The condition for resonant interaction provides the range of unstable wavenumbers causing exponential growth. By considering three different types of shear instabilities - Kelvin-Helmholtz, Taylor and Holmboe, we have shown that the resonant condition in each case matches the predictions of the canonical normal-mode based linear stability theory.

In addition to perceiving the shear instability problem in terms of two interacting linear waves, WIT also provides an alternate perspective - understanding shear instability in terms of dynamical systems. According to WIT, an unstable shear layer represents a non-linear dynamical system of the source-sink type, source and sink being the two equilibrium points. The equilibrium condition of the dynamical system is analogous to the resonant condition of the two-interacting-waves system. In terms of canonical linear stability theory, the source and the sink respectively correspond to the decaying and the growing normal-modes of the discrete spectrum.

The most important aspect of WIT is that it provides a non-modal description of idealized shear instabilities. Non-modal instability signifies non-orthogonal interaction between the two wave modes, and is the entire process

occurring prior to resonance. Rapid transient growth is a key feature of non-modal instability process. WIT shows that optimal growth occurs when the two waves are in quadrature. The phenomenon of transient growth has been studied very briefly in this thesis; thorough research is required in future for its detailed understanding.

Chapter 3

Non-linear Kelvin-Helmholtz instability in a piecewise linear shear layer [1]

The interplay of ideas and the oblique uses of knowledge are often of extraordinary interest. — Sherlock Holmes in The Valley of Fear.

3.1 Introduction

Shear layers are ubiquitous in atmospheres and oceans. These layers can become hydrodynamically unstable, giving rise to Kelvin-Helmholtz instability (KH). The non-linear manifestation of KH is usually in the form of spiraling billows, whose breaking generates turbulence in geophysical flows.

In theoretical and numerical studies, the hyperbolic tangent velocity profile is often used to model smooth barotropic shear layers (Hazel, 1972). Initially

[1] A version of this chapter has been published. A. Guha, M. Rahmani and G. A. Lawrence (2013) Evolution of a barotropic shear layer into elliptical vortices, Physical Review E.

interested in understanding the long time evolution of KH emanating from the hyperbolic tangent profile, we performed a direct numerical simulation (DNS); see Fig. 3.1(a). The flow re-laminarizes once the KH billow completely breaks down into small scales via turbulent processes. At this stage, the thickness of the shear layer has approximately quadrupled and, more importantly, the profile has almost become piecewise linear (see Fig. 3.1(b)). As shown in Fig. 3.1(c), the new base flow can be well described by Eq. (2.44), which serves as the initial condition for the subsequent instability processes. Detailed study on the linear instability arising from this base flow has been performed in Chapter 2.4. The study has shown that this velocity profile produces two counter-propagating vortcity waves (see Fig. 3.1(d)), which interacts to produce the subsequent Kelvin-Helmholtz instability mechanism. The underlying theory has been referred to as the wave interaction theory (WIT).

The first non-linear analysis of a piecewise linear shear layer was performed by Pozrikidis & Higdon (1985). They used a boundary integral method known as *contour dynamics* to show that the piecewise linear shear profile evolves into nearly elliptical patches of constant vorticity - *Kirchhoff vortices*. We hypothesize that the initial shear layer profile determines the asymptotic form of the ensuing KH - hyperbolic tangent shear layers give rise to spiral billows, while piecewise linear shear layers produce Kirchhoff vortices.

The spiraling billow form of KH has been thoroughly investigated in the past. In fact, the spiral billow shape has become the signature of KH (Smyth & Moum, 2012); but little is known about the non-linear evolution of the

piecewise linear shear layer. This is because the piecewise linear profile is usually considered to be of little practical relevance, hence its usage is restricted to theoretical studies - mainly as an approximation of smooth shear layers (Pozrikidis, 1997; Carpenter *et al.*, 2013). On the contrary, our DNS result in Fig. 3.1(a,b) indicates that the quasi piecewise linear profile is also likely to occur in nature. The fact that this profile produces elliptical vortices similar to those observed in geophysical and astrophysical flows, e.g. meddies in Atlantic ocean (Chérubin *et al.*, 2003), stratospheric polar vortices (Waugh & Randel, 1999), Great Red Spot and other Jovian vortices (Morales-Juberías *et al.*, 2002), Neptune's Great Dark Spot (Polivani *et al.*, 1990), and coherent vortices in the atmosphere of Uranus (Liu & Schneider, 2010), has motivated us to investigate further.

3.2 Non-linear simulation

Over the last few decades, sophisticated computational techniques have been developed for precise understanding of turbulent processes. Two such techniques worth mentioning are direct numerical simulation (DNS) and vortex methods.

Many geophysical and astrophysical flows can be assumed homogeneous, incompressible and quasi-inviscid. In such flows, vorticity plays a major role in driving non-linear processes like chaos and turbulence (Saffman, 1995). Vortex methods are especially useful under such circumstances; they numerically solve

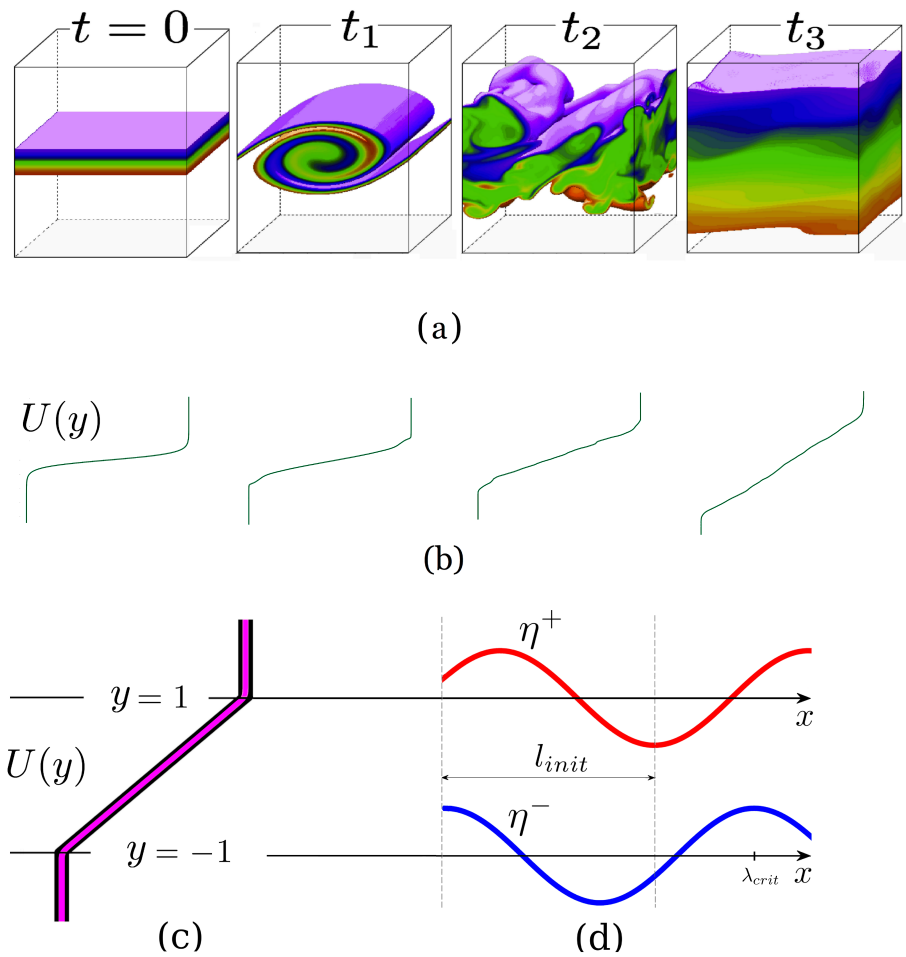

Figure 3.1: (a) 3D DNS performed to capture the complete turbulent dissipation of a KH billow ensuing from a hyperbolic tangent velocity profile. False color is added to aid visualization. (b) Spanwise averaged mean velocity profile corresponding to each instant. (c) The magenta line is the continuous velocity profile obtained from Eq. (3.7), while the thick black line below it is the piecewise linear profile from Eq. (2.44). (d) CVWs (exaggerated) existing at the vorticity discontinuities.

the inviscid and incompressible Navier-Stokes equations (Euler equations). An example of one such 2D vortex method is contour dynamics (Deem & Zabusky, 1978).

3.2.1 Contour dynamics

High Reynolds number flows have a tendency to develop finite-area vortex regions or "vortex patches" with steep sides (Deem & Zabusky, 1978; Pullin, 1992). If the flow is incompressible and 2D, the area as well as the vorticity of a vortex patch are conserved quantities. The vortex patch boundary is referred to as a "contour", and is both a vorticity jump and a material surface (Saffman, 1995). A small perturbation on this contour sets up a vorticity wave (Deem & Zabusky, 1978).

Substantial simplification is possible for constant vorticity patches; the governing 2D Euler equations can be reduced to a 1D boundary integral. This provides a significant advantage for computing the vortex patch evolution by only solving the contour motion. This methodology is known as the contour dynamics (CD) (Pullin, 1992). The contour motion is obtained by tracing the patch boundary with N Lagrangian markers. The evolution of the i-th Lagrangian marker is obtained by solving the following integro-differential equation:

$$\frac{d\mathbf{x}_i}{dt} = -\frac{\Omega}{4\pi} \int_C \ln \left[\left(\triangle x_i^{'} \right)^2 + \left(\triangle y_i^{'} \right)^2 \right] d\mathbf{x}^{'} \tag{3.1}$$

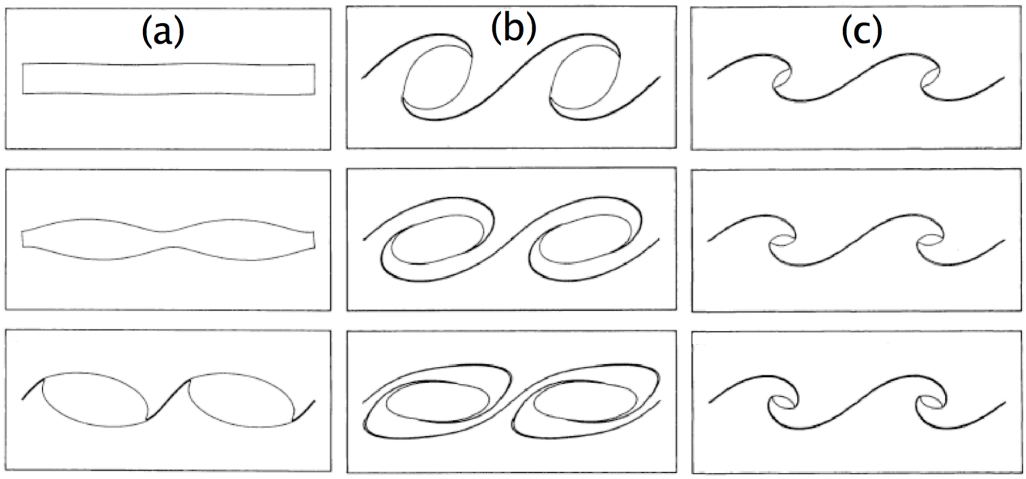

Figure 3.2: Contour dynamics simulation of a piecewise linear shear layer by Pozrikidis & Higdon (1985) for (a) $\alpha = 0.639$, (b) $\alpha = 0.5$ and (c) $\alpha = 0.0625$.

where $\Omega = 1$ is the patch vorticity, $\mathbf{x} = [x, y]^T$, $\triangle x_i^{'} = x_i - x^{'}$, $\triangle y_i^{'} = y_i - y^{'}$ and C is the contour around one patch[5].

Observing that a piecewise linear shear layer can be represented by a horizontally periodic patch of constant vorticity, Pozrikidis & Higdon (1985) modified Eq. (3.1) for a periodic domain (Pozrikidis, 1997) :

$$\frac{d\mathbf{x}_i}{dt} = -\frac{\Omega}{4\pi} \int_C \ln \left[\cosh\left(\alpha \triangle y_i^{'}\right) - \cos\left(\alpha \triangle x_i^{'}\right) \right] d\mathbf{x}^{'} \tag{3.2}$$

On perturbing the contour with sinusoidal disturbances, the shear layer rolls up producing nearly elliptical patches of constant vorticity (Pozrikidis & Higdon, 1985).

[5]Unlike Chapter 2, the cross streamwise coordinate is denoted by 'y' instead of 'z'. This is primarily to stress that there is no density variation along this coordinate.

We interpret the rolling up of the piecewise linear shear layer in terms of the interaction between two CVWs. To better understand this point, let us first consider the simple case of a circular patch of constant vorticity. A small perturbation on its contour produces a linearly stable vorticity wave (also known as "Kelvin wave") (Deem & Zabusky, 1978; Mitchell & Rossi, 2008). Similarly, perturbation on a periodic, piecewise linear shear layer produces two counter-propagating vorticity waves, one at the upper interface and the other at the lower interface. These two CVWs interact with each other causing the shear layer to evolve into elliptical vortex patches. Since WIT represents the linear dynamics of the shear layer evolution process, CD can be regarded as a non-linear extension of WIT.

We assume the pair of CVWs to be initially of the form:

$$\eta^{+} = a_0 \cos(\alpha x - \Phi) \qquad \text{at } y = 1 \tag{3.3}$$

$$\eta^{-} = a_0 \cos(\alpha x) \qquad \text{at } y = -1 \tag{3.4}$$

where the perturbation amplitude $a_0 \ll 1$ and the phase shift $\Phi \in [-\pi, \pi]$. Eqs. (3.3)-(3.4) are similar to the initial perturbation profiles assumed by Pozrikidis & Higdon (1985), except that they interpreted these equations as contour perturbations. Also our choice of α and Φ are different from Pozrikidis & Higdon (1985). We set $\alpha = \alpha_{crit} = 0.4$ (i.e. the fastest growing mode) to ensure that the resulting non-linear structure is most likely to be realized in nature; whereas, Pozrikidis and Higdon used several values of α, not including

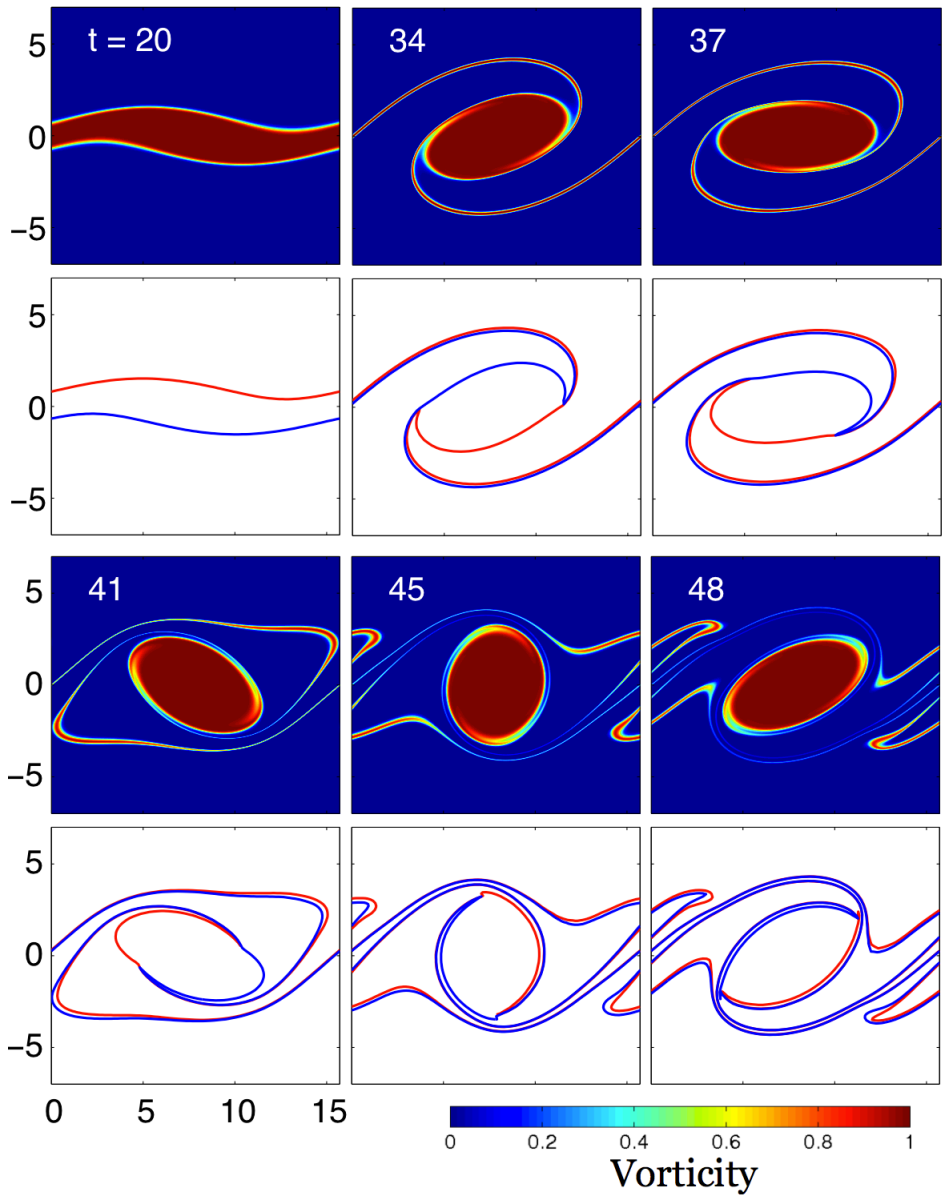

Figure 3.3: Time evolution of Kelvin-Helmholtz instability - comparison between DNS and CD.

α_{crit}. Corresponding to each α, Pozrikidis & Higdon (1985) observed the shear layer to produce a unique non-linear structure; see Fig. 3.2.

To ensure exponential growth from time t = 0, we set $\Phi = \theta_{NM}^{crit} = 0.353\pi$; whereas, in Pozrikidis and Higdon, $\Phi = 0$ or π. The angle θ_{NM}^{crit} is θ_{NM} corresponding to α_{crit}. Recall from Chapter 3 that θ_{NM} is the phase-locking angle (see Eq. (2.52)), and is given by:

$$\theta_{NM} = \cos^{-1}\left[(1-2\alpha)\, e^{2\alpha}\right]$$

In summary, WIT provides the initial conditions (i.e. α_{crit} and θ_{NM}^{crit}) for modeling the non-linear evolution.

We follow the numerical method outlined in Pozrikidis (1997) to solve Eq. (3.2). The contour is approximated by a polygonal line which connects the successive marker points. The integral over a segment that does not contain the i-th marker point is easy to compute by using standard numerical integration methods, e.g. trapezoidal rule. However the integral over the adjacent segments S_j of the i-th marker point, corresponding to $j = i-1$ and i, exhibits logarithmic singularity and is computed as follows:

$$\int_{S_j} \ln\left[\cosh\left(\alpha\triangle y_i^{'}\right) - \cos\left(\alpha\triangle x_i^{'}\right)\right] d\mathbf{x}^{'} \quad =$$

$$\int_{S_j} \ln\left[\frac{\cosh\left(\alpha\triangle y_i^{'}\right) - \cos\left(\alpha\triangle x_i^{'}\right)}{\left(\triangle x_i^{'}\right)^2 + \left(\triangle y_i^{'}\right)^2}\right] d\mathbf{x}^{'} + \int_{S_j} \ln\left[\left(\triangle x_i^{'}\right)^2 + \left(\triangle y_i^{'}\right)^2\right] d\mathbf{x}^{'} \quad (3.5)$$

The first integral on the R.H.S. is non-singular and is computed by using trapezoidal rule. The singularity has been shifted to the second integral, which can fortunately be integrated analytically:

$$\int_{S_j} \ln\left[\left(\triangle x_i^{'}\right)^2 + \left(\triangle y_i^{'}\right)^2\right] d\mathbf{x}^{'} = (\mathbf{x}_{j+1} - \mathbf{x}_j)\left(\ln|\mathbf{x}_{j+1} - \mathbf{x}_j|^2 - 2\right) \tag{3.6}$$

We consider a domain one wavelength ($\lambda_{crit} \equiv 2\pi/\alpha_{crit} = 5\pi$) long, and solve Eq. (3.2) using central differencing for space derivatives and 4th order Runge-Kutta for time. Each wave is initially represented by 400 points. During its evolution process, an adaptive point insertion-deletion algorithm is used to check if the neighboring points are within a desired distance.

3.2.2 Direct numerical simulation

Previous studies have used CD mainly as a tool for *qualitative* understanding of problems involving inviscid vortical flows (Pullin, 1992). In order to demonstrate the quantitative capabilities of CD, we validate our CD simulation against a pseudo-spectral DNS. The DNS code uses full Fourier transforms in the horizontal direction, and half-range sine or cosine Fourier transforms in the vertical direction in order to convert the set of partial differential equations (Navier-Stokes equations) into ordinary differential equations. Time integration is performed using a third-order Adams-Bashforth method. Detailed description of this code can be found in Winters et al. (Winters *et al.*, 2004).

We consider a domain of length λ_{crit} in the horizontal direction and nine

times the initial shear layer thickness in the vertical direction. The horizontal boundary condition is periodic while the vertical boundary condition is no-flux free-slip. We perform a 2D simulation at Reynolds number $Re = 10,000$ ($Re = 1/\nu$, where ν is the fluid viscosity). This Reynolds number is high enough to mimic quasi-inviscid flow conditions. To simulate the smallest scales of motion, we resolve our domain using 2880 points in horizontal and 3456 points in vertical direction.

Since non-differentiable profiles like Eq. (2.44) are subject to Gibbs phenomena, we use a smooth velocity profile that resembles the piecewise linear profile very closely; see Fig. 3.1(c). This velocity profile is derived from a vorticity distribution having the form

$$\Omega\left(y\right) = \frac{1}{2}\left[1 - \tanh\left(\frac{y^2 - 1}{\epsilon}\right)\right] \tag{3.7}$$

Integrating Eq. (3.7), the velocity profile is obtained directly: $U = \int \Omega dy$. The linear stability characteristic of this profile matches with that of the piecewise linear profile almost exactly, and has the same α_{crit}. Equating the total circulation of DNS with CD yields $\epsilon = 0.100$. The vorticity field in DNS is perturbed to match the initial wave amplitude growth in CD.

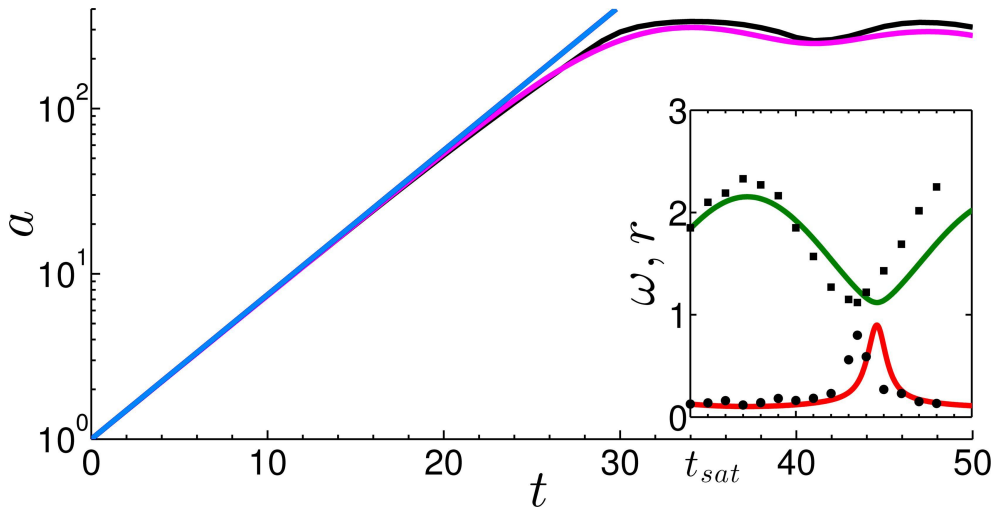

Figure 3.4: Temporal variation of the wave amplitude a. The straight blue line is the prediction from linear theory, the black line corresponds to CD while the magenta line represents DNS results. The green and red lines in the inset respectively show the variation of the ellipse aspect ratio r and the angular rotation rate ω with time. These variations are obtained by solving Eqs. (3.9)-(3.10). The black markers indicate the corresponding data points measured from DNS.

3.3 Results and discussion

3.3.1 Pre-saturation and saturation phases

The non-linear evolution of KH is illustrated in Fig. 3.3. It shows the vorticity field from DNS and contour lines from CD. The vorticity of the region enclosed by the contour lines is conserved in CD. However the presence of viscosity makes conservation of vorticity invalid in DNS. The implementation of high Re DNS minimizes the viscous effects, making DNS comparable to CD. The basic premise behind our simulations is the conservation of total circulation $\Gamma = \Omega A$ (where the vorticity $\Omega = 1$ and A is the shear layer area), which

comes from Kelvin's Circulation theorem (Saffman, 1995). Its corollary is the conservation of shear layer area - a quantity that remains fixed at its initial value $A = 2\lambda_{crit}$.

Fig. 3.4 shows the time evolution of the wave amplitude $a = |\max(\eta^+) - 1| = |\min(\eta^-) + 1|$. The maximum shear layer thickness, $H = 2(1 + a)$ evolves in a fashion similar to the wave amplitude a. We find the growth to be exponential, at least for $t \leq 20$. CVW interaction causes the shear layer to grow non-linearly. This phenomenon leads to the roll-up and formation of the elliptical core vortex (Kirchhoff vortex). The evolution process is shown in Fig. 3.3. The part of the shear layer between the crest of the lower wave and the trough of the upper wave (see Fig. 3.1(d)) gives rise to the elliptical core, the initial length of which is given by

$$l_{init} = \left(1 + \frac{\theta_{NM}^{crit}}{\pi}\right) \frac{\lambda_{crit}}{2} \tag{3.8}$$

The flow saturates (i.e. the amplitude reaches a maxima) at $t_{sat} = 34$. For $t \geq t_{sat}$, approximately 80% of Γ is concentrated in the core. H also reaches a maxima at saturation, and has the value $H_{max} = 8.7$. The fully formed elliptical cores are connected by thin filaments of fluid called *braids*. These braids wrap around the rotating cores, producing a complex spiral like structure, as shown in Fig. 3.3.

3.3.2 Early post-saturation phase

After saturation, the core rotates with an angular velocity ω, causing the wave amplitude, a, to oscillate with a time period $T_{amp} \approx 13$; see Fig. 3.4. The core also nutates, i.e. the core aspect ratio r (defined as the ratio between the ellipse major axis and the minor axis) undergoes a periodic oscillation. This *nutation* phenomenon is apparent in both Figs. 3.3 and 3.4.

Nutation

To better understand the nutation process, we consider the simple model proposed by Kida (1981). An isolated Kirchhoff vortex rotates in the presence of a constant background strain-rate γ. The velocity field associated with this strain-rate is given by $u_s = \gamma\sigma$, $w_s = -\gamma\xi$ where σ and ξ are the principal axes with the origin at the centre of the ellipse. In our case, this velocity field mimics the leading order straining effect induced by the rotation of other Kirchhoff vortices. Note that the periodic boundary condition takes into account the effects of other Kirchhoff vortices.

Let the clockwise angle between σ and the ellipse major axis be θ at any instant. Then θ and r evolve as follows (Kida, 1981):

$$\omega \equiv \frac{d\theta}{dt} = -\gamma \left(\frac{r^2+1}{r^2-1}\right) \sin(2\theta) + \frac{\Omega r}{(r+1)^2} \tag{3.9}$$

$$\frac{dr}{dt} = 2\gamma r \cos(2\theta) \tag{3.10}$$

Eq. (3.10) implies that the nutation is caused by strain. It also reveals that r

reaches maxima at $\theta = \pm\pi/4$. Simultaneously, Fig. 3.3 shows that the core nutates with a maximum value of r along the x axis and a minimum along the y axis. Therefore the σ axis must make an angle of $\pi/4$ with the x axis. The angle made by the braid with the x axis at the stagnation point(s) is also $\pi/4$. This is because the braid aligns itself with the streamlines.

To investigate why the σ axis makes an angle of $\pi/4$ with the x axis, we consider an ideal problem where an infinite number of Kirchhoff vortices, each of circulation $\Gamma_{core} = \Gamma$ (note $\Gamma = 2\lambda_{crit}$), are placed along the x axis with a constant spacing λ_{crit} between their centers. The effect of a vortex patch at a point outside its own boundary is exactly the same as that of a point vortex of equivalent strength placed at the center of the patch (Pozrikidis, 1997). Therefore we replace all the Kirchhoff vortices with point vortices of strength Γ_{core}. This provides a simplistic understanding of the mechanism by which the rotation of distant vortex patches strain a given patch. We find this *ideal* strain-rate to be

$$\gamma' = \frac{\Gamma_{core}}{2\pi\lambda_{crit}^2} \sum_{n=-\infty, n\neq 0}^{\infty} n^{-2} = 0.067 \tag{3.11}$$

The principal axes of the strain field produced by this infinite array of point vortices make angles of $\pm\pi/4$ with the x axis. Hence, this ideal strain field and the strain field of our actual problem have the same orientation. Before comparing the magnitudes of these two fields, it is important to note that the presence of braids complicate the actual problem by making the strain-rate magnitude vary spatially. We simplify the analysis by assuming a strain

field of constant magnitude acting on the elliptical core, thereby reducing the problem to the Kida problem described by Eqs. (3.9)-(3.10). DNS is used to supplement the analysis by providing the values of r and θ wherever necessary. By applying this methodology, the magnitude of the actual strain-rate is found to be $\gamma = 0.073$, which is quite close to the ideal value of 0.067 obtained from Eq. (3.11).

We also capture the evolution of r and ω by solving Eqs. (3.9)-(3.10); see the inset in Fig. 3.4. The initial values are obtained from DNS, and $\gamma = 0.073$. The spike in ω at $t \approx 45$ is caused by $r \to 1$. The figure shows that Kida's model compares well with the DNS. In DNS we fit an ellipse on the Kirchhoff vortex using a least-square based algorithm (Hendel, 2008). Points on the surface of the vortex are selected manually and then the best-fit ellipse is generated. The code supplies the length of the ellipse axes, as well as the orientation.

The nutation period is found to be $T_{nut} \approx 13$, while the period of core rotation is $T_{core} = 2\pi/\bar{\omega} \approx 26$ (overbar denotes average). $T_{core} \approx 2T_{nut}$ is because one full rotation corresponds to passing the coordinate axes twice. Likewise, $T_{core} \approx 2T_{amp}$ because the braids are connected to the two ends of the core.

Small length scale production

The smallest length scales are found to occur in the braid region adjacent to the core; see Fig. 3.3. This is due to the straining effect of the rotating elliptical

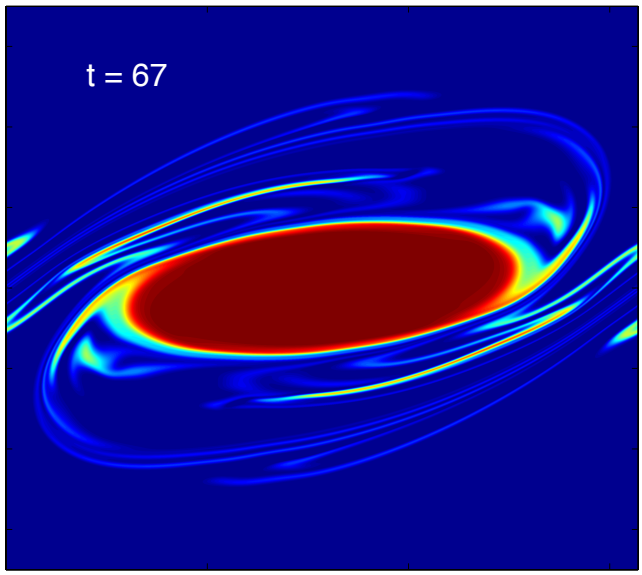

Figure 3.5: Formation of winding filaments around the elliptical vortex during the late post-saturation phase.

core which causes the braid region in its vicinity to thin exponentially fast. In real flows, when a fluid element becomes sufficiently thin, the balance between the strain-rate and the viscous dissipation determines the small length scales. The order of magnitude of the core rotation induced strain-rate, γ_{local}, can be obtained by replacing the core with a point vortex of equivalent strength and located at the ellipse centre:

$$\gamma_{local} \sim \frac{\Gamma_{core}}{2\pi l^2} = \frac{1}{2} \tag{3.12}$$

where l is the characteristic length of the core. Notice that this local strain-rate is one order of magnitude greater than the background strain-rate γ or γ'.

The smallest length scale appearing in a 2D "turbulent" flow is $L_{2D} \sim Re^{-1/2}$ (Davidson, 2004). This length scale is a 2D analogue of the Taylor microscale occurring in 3D turbulent flows. In order to estimate the time when L_{2D} appears in our flow, we formulate a braid evolution equation similar to Eq. (2.8) of Corcos and Sherman (Corcos & Sherman, 1976):

$$\delta^2\left(t^*\right) = \delta^2\left(0\right) e^{-2\gamma_{local}t^*} + \frac{\pi}{2\gamma_{local}Re}\left(1 - e^{-2\gamma_{local}t^*}\right) \tag{3.13}$$

where $\delta\left(t^*\right)$ is the braid thickness adjacent to the core at time $t^* = t - t_{sat}$. We estimate $\delta\left(0\right)$ from our DNS and solve Eq. (3.13). L_{2D} is found to appear soon after saturation, around $t^* \approx 4$, implying that 2D transitional flows like KH can give rise to "turbulent" features at a very early stage.

3.4 Conclusion

When a piecewise linear shear layer becomes unstable, it evolves into a series of elliptical vortices of constant vorticity (Kirchhoff vortices) connected by thin braids. The interaction between two counter-propagating vorticity waves is the driving mechanism behind this instability process. Although this wave interaction perspective was known previously, linearized approximations forced the analysis to be valid only in the linear regime. By finding and exploiting the link between two quite different theories, namely wave interaction theory and contour dynamics, we are able to extend the analysis to the fully non-linear

domain.

The production of Kirchhoff vortices shows that KH arising from a piecewise linear shear layer is very different from the classical spiraling billow type KH ensuing from a smooth shear layer. The characteristics of this little known KH have been investigated. The rotation and nutation of the Kirchhoff vortices are found to be consistent with the predictions of Kida. The time period of rotation of these vortices is twice the period of nutation and the period of maximum shear layer height oscillation. The braids connecting the Kirchhoff vortices thin exponentially fast to a length scale which is the 2D equivalent of Taylor microscale.

Elliptical vortical structures, similar to those found in our simulations, are quite common in nature, especially in regions with quasi piecewise linear shear. Examples of such vortices include meddies in the Atlantic ocean, stratospheric polar vortices, and vortices in the gas giant planets like Jupiter, Neptune and Uranus. Our analysis may motivate further investigation of their formation and evolution.

Chapter 4

Linear stability of a Plane Couette-Poiseuille flow in the presence of cross-flow [1]

Each fact is suggestive in itself. Together they have a cumulative force. — Sherlock Holmes in The Bruce-Partington Plans.

4.1 Introduction

From the perspective of applications in technology, Poiseuille flow of viscous fluid along a duct is undoubtedly one of the most important flows studied as it underpins the field of hydraulics. Instability and subsequent transition from laminar flow marks a paradigm shift in the dominant transport mechanisms of mass, momentum and heat, and it is for this reason that the subject remains of enduring interest, even after more than 100 years of study. In this chapter we focus on two methods for affecting the linear stability of plane Poiseuille

[1] A version of this chapter has been published. A. Guha and I.A. Frigaard (2010) On the stability of plane Couette-Poiseuille flow with uniform crossflow, Journal of Fluid Mechanics.

(PP) flow. The first method consists of introducing a Couette component to the flow, by translation of one of the walls. The second method consists of introducing a cross-flow, e.g. via injection through a porous wall. While both effects have been studied individually to some extent, there are fewer studies of the two effects combined, which is the main focus here.

PP flow is linearly unstable when the critical Reynolds number exceeds $Re_c \approx 5772$, (Reynolds number based on the center-line axial velocity and the half-width of the channel; see Orszag (1971)), whereas the plane-Couette (PC) flow is absolutely stable with respect to infinitesimal amplitude disturbances, $Re_c = \infty$; see Romanov (1973). Superimposing PP and PC flows, we may ask if a small Couette component can affect the stability of the PP flow. Stability of plane Couette-Poiseuille (PCP) flow was first studied by Potter (1966) and later by Hains (1967), Reynolds & Potter (1967) and Cowley & Smith (1985). The results are typically understood with respect to a Reynolds number that is based on the maximal velocity of the Poiseuille component, say Re_p, and the ratio of wall velocity to maximal velocity of the Poiseuille component, denoted k. For small Couette components, k, it is possible to observe some destabilization of the flow, (depending on the wavenumber), but as soon as $k > 0.3$ a strong stabilization of the flow sets in. As the velocity ratio k exceeds 0.7, the neutral stability curve completely vanishes and the flow becomes unconditionally linearly stable, i.e. $Re_c \to \infty$. The term "cut-off" velocity has been used to describe this stabilization; see Reynolds & Potter (1967).

The stability of PP flow with cross-flow was first analysed by Hains (1971) and Sheppard (1972), both of whom have shown that a modest amount of cross-flow produces significant increase of the critical Reynolds number. These results are however slightly problematic to interpret in absolute terms, since at a fixed pressure gradient along the channel, increasing the cross-flow decreases the velocity along the channel, (hence effectively the Reynolds number). This difficulty was noted by Fransson & Alfredsson (2003), who used the maximal channel velocity as their velocity scale (instead of that based on the PP flow without cross-flow), and thus separated the effects of base velocity magnitude from those of the base velocity distribution. Using this velocity scale in their Reynolds number Re, they showed regimes of both stabilization and destabilization as the cross-flow Reynolds number was increased. For example, for $Re = 6000$ and wavenumber $\alpha = 1$, Fransson & Alfredsson (2003) have shown that the cross-flow was stabilizing up to a cross-flow Reynolds number $Re_{inj} \approx 3.4$, and then starts destabilizing before re-stabilizing again at $Re_{inj} \approx 635$. The initial regime of stabilization is the one corresponding to the earlier results.

In the present study we focus on the combination of cross-flow and Couette component. Our motivation stems from a desire to understand how the two mechanisms interact, since in terms of technological application different mechanical configurations may be more or less amenable to cross-flow and/or wall motion. This means that there is value in knowing when one effect may compensate for the other in stabilizing (or destabilizing) a given flow. To the

best of our knowledge, stability of PCP flow with cross-flow has only been studied in any generality by Hains (1971). In considering the base flow for PCP flow with cross-flow, (which is parameterized by Re_{inj} and k), the relation $kRe_{inj} = 4$, defines an interesting paradigm in which the base velocity in the axial direction is linear. These Couette-like flows have been studied by Nicoud & Angilella (1997) for increasing Re_{inj}. They found a critical value of $Re_{inj} \approx 24$, below which which no instability occurs, (we have translated their critical value of 48 into the Re_{inj} that we use). Therefore, we observe that understanding of cross-flow PCP flows is far from complete. We aim to contribute to this understanding.

The 3D linear stability of PCP flow with cross-flow is amenable to Squires transformation, so that the linear instability occurs first for 2D (spanwise-independent) perturbations. It is these perturbations that we study here. Our aim is to demarcate clearly in the (Re_{inj}, k)-plane, regions of unconditional stability, i.e. where there is a cut-off wall velocity or injection velocity. We also wish to understand the underlying linear stability mechanisms as Re_{inj} and k are varied.

4.2 Stability of plane Couette-Poiseuille flow with cross-flow

The base flow considered in this work is a plane Couette-Poiseuille flow (PCP) with imposed uniform cross-flow. This flow is two-dimensional, viscous, incom-

pressible and fully developed in the streamwise direction, x. The imposed base velocity in the y-direction [6], v , is constant and equal to the injection/suction velocity V_{inj}. Since v is constant, the x-component of velocity, u depends only on y. The flow domain is bounded by walls at $y = \pm h$, and is driven in the x-direction by a constant pressure gradient and by translation of the upper wall, at speed U_c. The x-component of velocity, $u(y)$, is found from the x-momentum equation, which simplifies to:

$$V_{inj}\frac{\partial u}{\partial y} = -\frac{1}{\rho}\frac{\partial p}{\partial x} + \nu\frac{\partial^2 u}{\partial y^2} \tag{4.1}$$

where ρ is the density, $\nu = \mu/\rho$ is the kinematic viscosity, and μ is the dynamic viscosity. The boundary conditions at $y = \pm h$ are:

$$u(-h) = 0, \quad u(h) = U_c \tag{4.2}$$

To scale the problem we scale all lengths with h, hence $(x, y) = (x/h, y/h)$ (i.e. henceforth x and y are non-dimensional variables) For the velocity scale two choices are common. First, the imposed pressure gradient defines a "Poiseuille" velocity scale:

$$U_p = -\frac{h^2}{2\mu}\frac{\partial p}{\partial x}, \tag{4.3}$$

which is equivalent to the maximum velocity of the plane Poiseuille flow, driven by the pressure gradient alone. Second, we may take the maximum velocity,

[6] Unlike Chapter 2, the cross streamwise coordinate is denoted by 'y' instead of 'z'. This is primarily to stress that there is no density variation along this coordinate.

which we need to compute. U_p is the choice of Potter (1966), and thus allows one to compare directly with the studies of PCP flows. In the absence of a cross-flow, the maximal velocity is not actually very sensitive to the wall velocity U_c, at least for $U_c < U_p$, which covers the range over which the flow stabilizes. However, in the case of a strong cross-flow the x-velocity is reduced significantly below U_p, which therefore loses its meaning. Consequently we adopt the second choice and scale with the maximal velocity, U_{max}. This choice retains physical meaning in the base velocity, but does introduce algebraic complexity.

The solution is found from (4.1)–(4.2) after detailed but straightforward algebra:

$$\frac{u(y)}{U_p} = \left[\frac{4\cosh Re_{inj} - kRe_{inj}\mathrm{e}^{-Re_{inj}} + [kRe_{inj} - 4]\mathrm{e}^{Re_{inj}y}}{2Re_{inj}\sinh Re_{inj}} + \frac{2y}{Re_{inj}}\right], \quad (4.4)$$

where k and Re_{inj} are defined by:

$$k = \frac{U_c}{U_p}, \quad (4.5)$$

$$Re_{inj} = \frac{V_{inj}h}{\nu}. \quad (4.6)$$

These two dimensionless parameters uniquely define the dimensionless base flow. The parameter k is the velocity ratio of Couette to Poiseuille velocities, which is useful as it allows direct comparison with earlier results on stabilization of PCP flows without cross-flow. The parameter Re_{inj} is simply a

Reynolds number based on the injection velocity. Primarily here we consider the ranges: $k \in [0, 1]$ and $Re_{inj} \geq 0$.

For relatively weak crossflow velocities, the velocity component $u(y)$ has a single maximum at a value of $y = y_{max}$ defined by:

$$\mathrm{e}^{Re_{inj} y_{max}} = \frac{\sinh Re_{inj}}{Re_{inj}} \frac{4}{4 - kRe_{inj}} \tag{4.7}$$

The maximal velocity U_{max}, is then evaluated from (4.4). Since, $\sinh Re_{inj} \geq Re_{inj}$, we can see that $y_{max} > 0$ for $k \geq 0$ and $Re_{inj} > 0$. Both the injection cross-flow and Couette component act to skew the velocity profile towards the upper wall. For stronger cross-flow velocities, (or sufficiently large k), the maximal velocity occurs at the upper wall, i.e. $U_{max} = U_c$.

The division between weak and strong cross-flows, taking into account also the Couette component, is defined by the line

$$kRe_{inj} = 4 \left[1 - \frac{\sinh Re_{inj}}{Re_{inj} \mathrm{e}^{Re_{inj}}} \right] \tag{4.8}$$

The dimensionless base velocity is given by:

$$u(y) = \begin{cases} \dfrac{4\cosh Re_{inj} - kRe_{inj}\mathrm{e}^{-Re_{inj}} - [4 - kRe_{inj}]\mathrm{e}^{Re_{inj}y} + 4y\sinh Re_{inj}}{4\cosh Re_{inj} - kRe_{inj}\mathrm{e}^{-Re_{inj}} - [4 - kRe_{inj}]\mathrm{e}^{Re_{inj}y_{max}} + 4y_{max}\sinh Re_{inj}}, \\ \qquad\qquad kRe_{inj} \leq 4\left[1 - \frac{\sinh Re_{inj}}{Re_{inj}\mathrm{e}^{Re_{inj}}}\right], \\ \dfrac{1}{k}\left[\dfrac{4\cosh Re_{inj} - kRe_{inj}\mathrm{e}^{-Re_{inj}} - [4 - kRe_{inj}]\mathrm{e}^{Re_{inj}y}}{2Re_{inj}\sinh Re_{inj}} + \dfrac{2y}{Re_{inj}}\right], \\ \qquad\qquad kRe_{inj} > 4\left[1 - \frac{\sinh Re_{inj}}{Re_{inj}\mathrm{e}^{Re_{inj}}}\right]. \end{cases} \tag{4.9}$$

It can be verified that in the limit $Re_{inj} \to 0$, with k fixed, the classical form of PCP base velocity profile is retrieved:

$$u(y) \sim \frac{1 - y^2 + \frac{k}{2}(1+y) + Re_{inj}[\frac{1}{3}(y - y^3) - \frac{k}{4}(1 - y^2)]}{1 + \frac{k}{2} + \frac{k^2}{16} - Re_{inj}[\frac{k}{6} - \frac{k^3}{64}]} \tag{4.10}$$

as $Re_{inj} \to 0$, with $k \leq 4[1 - \sinh Re_{inj}/(Re_{inj}\mathrm{e}^{Re_{inj}})]/Re_{inj} \sim 4[1 + Re_{inj}/3]$.

Examples of the base velocity profile are given in Fig. 4.1, for for $k = 0.5$ and different values of Re_{inj}. Observe that for $Re_{inj} = 8$, when $kRe_{inj} = 4$, the velocity profile is linear. This flow has been termed a "generalised Couette" flow by Nicoud & Angilella (1997).

We shall denote differentiation with respect to y by the operator D. The first and second derivatives of the base flow, Du and D^2u respectively, influence the stability of the flow. We find that D^2u has sign determined by $(kRe_{inj} - 4)$, and increases in absolute value exponentially towards the upper wall. For $kRe_{inj} < 4$, the velocity is concave, and is convex otherwise. Since D^2u does not change sign, the maximal absolute value of the first derivative is found

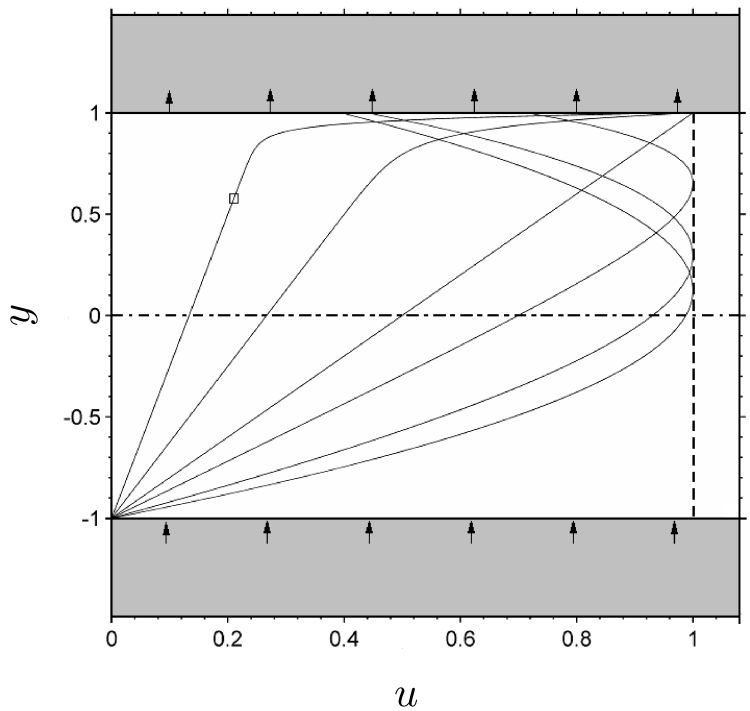

Figure 4.1: Mean Velocity Distribution for $k = 0.5$ and $Re_{inj} = 0$, 1, 4, 8, 15 and 30 ($Re_{inj} = 30$ marked with a $\square$)

either at the upper or lower wall, $y = \pm 1$. The maximal velocity gradients are found at the lower wall for small Re_{inj} and also for a range of Re_{inj} close to $kRe_{inj} = 4$, but otherwise are found at $y = 1$; see Fig. 4.2(a). At large Re_{inj} the maximal velocity increases almost linearly:

$$\begin{aligned} |Du|_{max} &= |Du(y=1)| = \frac{1}{k}\left[\frac{[kRe_{inj}-4]\mathrm{e}^{Re_{inj}}}{2\sinh Re_{inj}} + \frac{2}{Re_{inj}}\right] \\ &\sim Re_{inj} - \frac{4}{k} + \frac{2}{kRe_{inj}} + O(\mathrm{e}^{-2Re_{inj}}). \end{aligned} \tag{4.11}$$

Figure 4.2(b) shows examples of the profiles of D^2u. We observe that

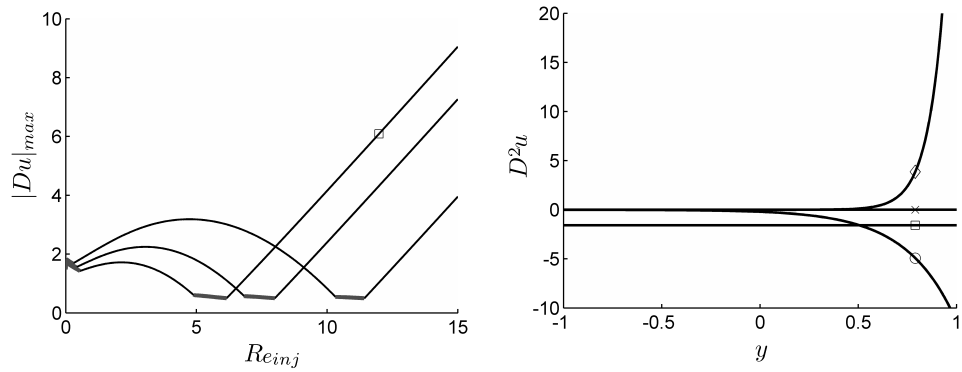

(a) (b)

Figure 4.2: (a) Maximal velocity gradient, $|Du|_{max}$, plotted against Re_{inj} for $k = 0.35$, 0.5, 0.65, ($k = 0.65$ marked with a $\square$). The thick line indicates where the maximum is attained at $y = -1$; otherwise at $y = 1$. (b) Variation of D^2u with y for $k = 0.5$ for : $Re_{inj} = 0$, ($\square$); $Re_{inj} = 4$, ($\circ$); $Re_{inj} = 8$, ($\times$); $Re_{inj} = 12$, ($\diamond$).

$D^2u \approx 0$ over a large range of y, close to the lower wall, whenever a significant amount of cross-flow is present, i.e. $Re_{inj} \gtrsim 1$.

4.2.1 Streamwise Reynolds number

The base base flow is fully defined by the parameters k and Re_{inj}, as discussed above. In addition, the transient flow and associated stability problem will depend on the streamwise Reynolds number, Re, which we define in terms of U_{max}, i.e.

$$Re = \frac{U_{max}h}{\nu}. \tag{4.12}$$

4.2.2 The stability problem

The base flow is two-dimensional, but since $v = Re_{inj}$ is constant, the 3D linear stability equations are only modified by the addition of a constant convective term:

$$Re_{inj}\frac{\partial}{\partial y}\mathbf{u}',$$

where $\mathbf{u}' = (u', v', w')$ denotes the linear perturbation. The classical Squire transformation can therefore be applied to the temporal problem, showing that for any unstable 3D linear disturbance there exists an unstable 2D linear disturbance at lower Re; see Squire (1933).

It suffices to consider only 2D disturbances and we adopt the normal mode approach introduced in Chapter 1. However the inclusion of cross-flow term adds an extra inertial component $Re_{inj}D(\alpha^2 - D^2)\phi$ (where ϕ is the amplitude of the perturbation streamfunction) to the conventional Orr-Sommerfeld (O-S) equation (see Eq. 1.16):

$$\mathrm{i}\alpha Re[(c-u)(\alpha^2 - D^2) - D^2 u]\phi - Re_{inj}D(\alpha^2 - D^2)\phi = (\alpha^2 - D^2)^2\phi, \quad (4.13)$$

The boundary conditions in this case are given by

$$\phi(\pm 1) \quad = \quad D\phi(\pm 1) = 0. \quad (4.14)$$

Note that Re_{inj} in Eq. (4.13) also influences stability via the base velocity profile $u(y)$. Equations (4.13)–(4.14) constitute the eigenvalue problem. The

eigenvalue c is parameterised by the 4 dimensionless groups $(\alpha, Re, Re_{inj}, k)$ and the condition of marginal stability is:

$$c_i(\alpha, Re, Re_{inj}, k) \quad = \quad 0 \tag{4.15}$$

We attempt to characterise the stability of (4.13)–(4.14) for positive (α, Re, Re_{inj}, k). We may note that the limit $Re \to \infty$ for finite Re_{inj}, reduces (4.13) to the Rayleigh equation. Since D^2u is of one sign only, there are no inflection points and hence no purely inviscid instability. This suggests that the instabilities of (4.13)–(4.14) will be viscous in nature.

Addition of the constant cross-flow terms does not fundamentally alter the O-S problem, and we expect a discrete spectrum. To find the spectrum of (4.13)–(4.14) we use a spectral approach, representing ϕ by a truncated sum of Chebyshev polynomials:

$$\phi \quad = \quad \sum_{n=0}^{N} a_n T_n\left(y\right) \text{ for } y \in [-1, 1] \tag{4.16}$$

where N is the order of the truncated polynomial, a_n is the coefficient of the n-th Chebyshev polynomial, $T_n\left(y\right)$. This method is described for example in Schmid & Henningson (2001) and is widely used. The discretised problem is coded and solved in Matlab. The accuracy of the code has been checked against the results of Mack (1976) for the Blasius boundary layer, with various results for PP flow in Schmid & Henningson (2001), with the PCP flow results of Potter (1966), and finally against results for PP flow with cross-flow; see

Sheppard (1972), Fransson & Alfredsson (2003). The results are accurate up to three, four and five significant places when validated against Potter (1966), Mack (1976) and Fransson & Alfredsson (2003), respectively. All the numerical results given below have been computed with $N = 120$. On using 200 collocation points, the growth rates changed only in the fourth significant place in the worst case.

4.2.3 Characteristic effects of varying k and Re_{inj}

Before starting a systematic analysis of (4.13)–(4.14), we briefly show some example results that illustrate the characteristic effects of varying the Couette component, k, and the cross-flow component, Re_{inj}. These examples also serve to establish the framework of analysis used later in this chapter. With reference to PP flow, Potter (1966) first observed that the stability is increased by adding a Couette component while Fransson & Alfredsson (2003) showed that cross-flow can stabilize or destabilize PP flow.

Eigenspectra

Setting $(\alpha, Re) = (1, 6000)$, we investigate variations in the eigenspectrum of (4.13)–(4.14). According to a classification proposed by Mack (1976), the spectrum of PP flow spectra may be divided into 3 distinct families: A, P and S. Family A exhibits low phase velocity and corresponds to the modes concentrated near the fixed walls. Family P represents phase velocities, c_r, close to the maximum velocity in the channel. Family S corresponds to the

mean modes and has phase velocity c_r close to the mean velocity. In Figs 4.3(a) & (b), we track the eigenmodes as k and Re_{inj}, respectively, are varied from zero. The initial condition (denoted by $\square$) represents the PP flow.

Referring to Fig. 4.3(a), (where $Re_{inj} = 0$), addition of the Couette component increases the mean velocity: the S modes shift from $c_r = 0.6667$ at $k = 0$ (PP flow) to $c_r = 0.7513$ at $k = 1$. The family of P modes is also shifted to the right. The A modes are associated with both walls and as k increases we see a splitting of the family, with the upper wall modes moving to the right as k is increased. The least stable mode is a wall mode associated with the lower wall, which we observe stabilizes monotonically as k is increased. Figure 4.3(b) shows the effects of increasing Re_{inj}, (holding $k = 0$). The least stable A mode of PP flow initially stabilizes and then destabilizes with increasing Re_{inj}. This behavior has also been observed by Fransson & Alfredsson (2003). For large Re_{inj} the A, P, and S families have disappeared, instead leaving two distinct families of modes. It appears that each of the A, P, and S families splits, with some modes entering each of the two families (this alternate splitting is most evident for the S modes). As observed by Nicoud & Angilella (1997), the phase speed no longer lies in the range of the axial velocity. This does not violate the conditions on c_r, given by Joseph (1968) and Joseph (1969), since these conditions are derived for parallel flows only.

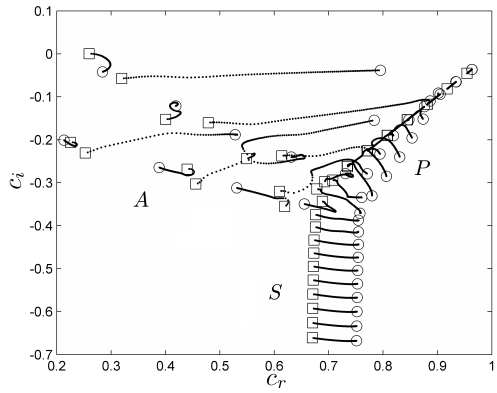

(a)

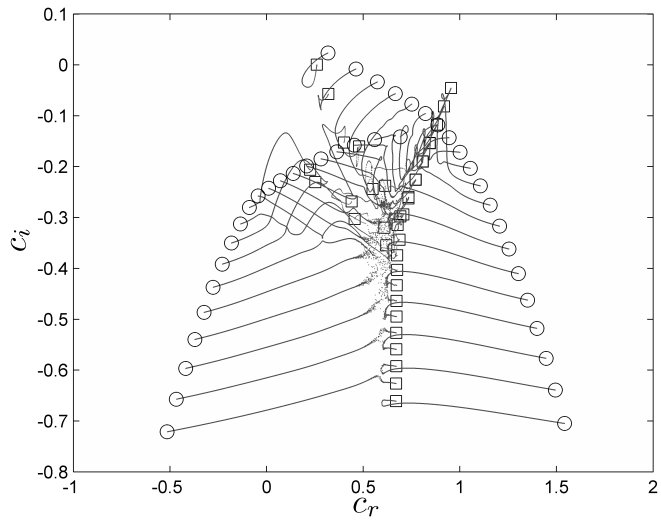

(b)

Figure 4.3: Eigenspectrum of $(\alpha, Re) = (1, 6000)$ by varying k and Re_{inj}. 40 least stable modes are considered. (a) Effect of increasing k from 0 to 1 in steps of 0.01, keeping $Re_{inj} = 0$. (b) Effect of increasing Re_{inj} from 0 to 100 in steps of 0.05, keeping $k = 0$ (PP flow). The symbols in (a) and (b) are similar and are denoted as follows: $k = 0$ or $Re_{inj} = 0$ by ($\square$), $k = 1$ or $Re_{inj} = 100$ by ($\circ$) and intermediate k or Re_{inj} by (.). Note that the PP flow spectrum is represented by the $\square$ in both figures, and shows the vertical family of S-modes, the branch of A-modes (diagonally upwards from centre to left) and branch of P-modes (diagonally upwards from centre to right).

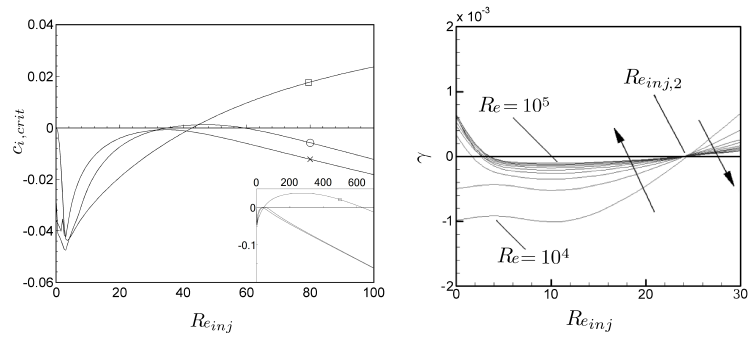

(a) (b)

Figure 4.4: (a) Effect of increasing Re_{inj} on the stability of PCP flow, for $(\alpha, Re) = (1, 6000)$ and different values of $k = 0\,(\square)$, $0.5\,(\circ)$, $1\,(\times)$. (b) Maximal growth rate for increasing Re_{inj} at different Re, ($k = 0.5$ and the step in values of Re between curves is 10^4).

Increasing Re_{inj}

Next, we illustrate the qualitative effects of increasing Re_{inj} at fixed (α, Re, k), in Fig. 4.4(a). We again fix $\alpha = 1$ and $Re = 6000$, and show the variation of the least stable eigenvalue, for $k = 0$, 0.5, 1. Our results for $k = 0$ (PP flow) may be compared directly with those of Fransson & Alfredsson (2003). We observe that as Re_{inj} increases we have an initial range of stabilization ($c_{i,crit}$ decreasing), followed by a range of destabilization ($c_{i,crit}$ increasing), and finally again stabilization at large Re_{inj}, ($c_{i,crit}$ decreasing). Qualitatively, we have observed these same three ranges of decreasing/increasing $c_{i,crit}$, as Re_{inj} increases, for all numerical results that we have computed, and this provides a convenient framework within which to describe our results.

For fixed (α, Re, k), the case $Re_{inj} = 0$ may either be stable or unstable, in which cases there are respectively two or three marginal stability val-

ues of Re_{inj}. We denote these marginal values of Re_{inj} by: $Re_{inj,1}$, $Re_{inj,2}$, $Re_{inj,3}$, noting that in the case that $Re_{inj} = 0$ is stable $Re_{inj,1}$ is absent. More clearly, $Re_{inj,2}$ will always represent a transition from stable to unstable, while $Re_{inj,1}$ & $Re_{inj,3}$ denote transitions from unstable to stable. The PCP flows for $k = 0.5$ and 1 are stable for $(\alpha, Re) = (1, 6000)$ in the absence of cross-flow, $Re_{inj} = 0$. For a larger Re, $k = 0.5$ is unstable at $Re_{inj} = 0$, but $k = 1$ remains stable for all (α, Re).

Figure 4.4(b) shows the maximal growth rate γ, for increasing Re_{inj} at different Re, with $k = 0.5$. The maximal growth rate is computed over wavenumbers $\alpha \in [0, 1]$:

$$\gamma = \max_{\alpha \in [0,1]} \{\alpha c_i\}, \tag{4.17}$$

which often captures the largest growth rates over all α. We observe that the first marginal value $Re_{inj,1}$ increases with Re, but appears to converge towards a finite value as $Re \to \infty$. The second marginal value of $Re_{inj,2}$ appears independent of Re, (at least numerically). For $k = 0.5$ we have $Re_{inj,2} \approx 24.7$. Nicoud & Angilella (1997) have observed a similar behaviour in studying the generalised Couette flow, (for which the constraint, $kRe_{inj} = 4$, is always satisfied). They have found $Re_{inj,2} \approx 24$ (note that Nicoud and Angilella use the full channel width as their length-scale, and therefore report $Re_{inj,2} \approx 48$, in their variables). In contrast, the third marginal value, $Re_{inj,3}$, is strongly dependent on Re. For example, for $k = 0.5$, the values corresponding to $Re = 10000$ and 100000 are $Re_{inj,3} \approx 83$ and $Re_{inj,3} \approx 287$ respectively.

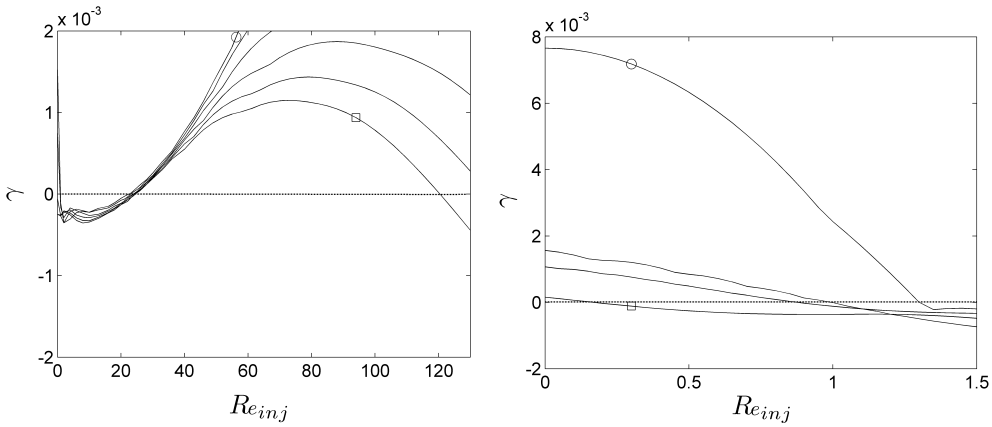

(a) (b)

Figure 4.5: Maximal growth rate versus Re_{inj} at $Re = 40000$: (a) $Re_{inj,2}$ & $Re_{inj,3}$ for $k = 0\,(\circ)$ to $1\,(\square)$; (b) $Re_{inj,1}$ for $k = 0\,(\circ)$ to $0.6\,(\square)$. Step size is 0.2 in both figures.

Increasing k

Figure 4.5 explores the effects of increasing the Couette component k, on γ and on the marginal values of Re_{inj}. Figure 4.5(a) indicates that the sensitivity of $Re_{inj,2}$ to k is also not extreme: we have found that this transition occurs within the range $\sim 22 - 25$ for $k \in [0, 1]$. For each value of k examined, we also observe numerically a similar independence of $Re_{inj,2}$ to Re as seen earlier in Fig. 4.4(b) for $k = 0.5$. The 3rd marginal value, $Re_{inj,3}$, is strongly dependent on k. For example, at $Re = 40000$, $Re_{inj,3}(k = 1) \approx 120$ and $Re_{inj,3}(k = 0.8) \approx 135$. In general, increasing k shifts $Re_{inj,3}$ to the left, thereby decreasing the span of the unstable region. Increasing k also decreases the maximum value of γ.

Figure 4.5(b) looks at the first transition, $Re_{inj,1}$ at $Re = 40000$. Potter

(1966) was the first to observe that for PCP flows (i.e. $Re_{inj} = 0$), a gradual increase in the wall velocity results in crossing a "cut-off" value of k, say k_1, such that for $k > k_1$ the flow is unconditionally linearly stable. It has already been pointed out from the results of Fig. 4.4(b) that $Re_{inj,1}$ is finite as $Re \to \infty$. In addition, the results in Fig. 4.5(b) indicate that $Re_{inj,1}$ decreases with k at a finite Re. Hence, it can be inferred that as $Re \to \infty$, the cut-off wall velocity, $k_1 = k_1(Re_{inj})$ must decrease with Re_{inj}.

4.3 PCP flows and the effects of small Re_{inj}

Having developed a broad picture of the different transitions occurring in the flow, we now focus in depth at each range of Re_{inj}, to understand the stability mechanisms in play. We start with the range of small Re_{inj}.

PCP flows without cross-flow are stable to inviscid modes, but viscosity admits additional modes, i.e. the Tollmien-Schlichting (TS) waves, which may destabilize, according to the value of k. When $\alpha R \gg 1$ with $c \sim O(1)$, viscous effects occur in thin oscillatory layers: (i) adjacent to the walls, (of thickness $\sim (\alpha Re)^{-1/2}$), and (ii) close to the critical point(s), y_c, where $u(y_c) = c_{r,crit}$ are found, (of thickness $\sim (\alpha Re)^{-1/3}$). It is in the critical layers that we see peaks in the distribution of energy production, implying transfer from the base flow. Potter (1966) put forward the argument that for a dimensionless wall velocity that exceeds $c_{r,crit}$, the critical layer near the moving wall will vanish and there remains only one critical layer, near the fixed lower wall. The thickness of this

second layer increases with wall velocity, thereby favouring stabilization.

This mechanism appears to correctly describe the long wavelength perturbations, (at $Re_{inj} = 0$), which are found to be the least stable for $k \sim O(1)$. Indeed Cowley & Smith (1985) developed a long wavelength analysis ($\alpha \sim Re$), in order to predict the cut-off value $k_1(Re_{inj} = 0) \approx 0.7$. For values $k \sim O(1)$, PCP flows have only a single neutral stability curve (NSC). However, Cowley & Smith (1985) noted that for smaller k, multiple neutral stability curves could exist, and at shorter wavelengths. For example, when $0 \leq k \leq Re^{-2/7}$ there is one NSC, when $Re^{-2/7} \leq k \leq Re^{-2/13}$ there are three NSC's, and when $Re^{-2/13} \leq k \ll 1$ there are two NSC's; see Cowley & Smith (1985). Thus to understand the effect of cross-flow in PCP flows, the different regimes of k need to be considered separately.

For $Re_{inj} \approx 0$, we expect the stability behaviour to be close to that of the PCP flow without cross-flow. Intuitively we expect cross-flow to stabilize, and so study the range $c_{r,crit} < k \leq k_1(Re_{inj} = 0)$. We examine the NSC's obtained from the O-S equation corresponding to $k = 0.5$, under different values of Re_{inj}; see Fig. 4.6(a). As expected, increasing Re_{inj} results in a progressively larger critical $Re = Re_{crit}$. We also observe that both the upper and the lower branches are oriented at an angle of 45 degrees, (i.e. $\alpha \sim Re^{-1}$), at high values of Re. On fixing Re_{inj} and increasing k we have found that for successively large k the upper and lower branches move together as Re_{crit} increases, eventually coalescing at $k = k_1(Re_{inj})$. This mechanism is identical with that observed by Cowley & Smith (1985), suggesting the applicability of

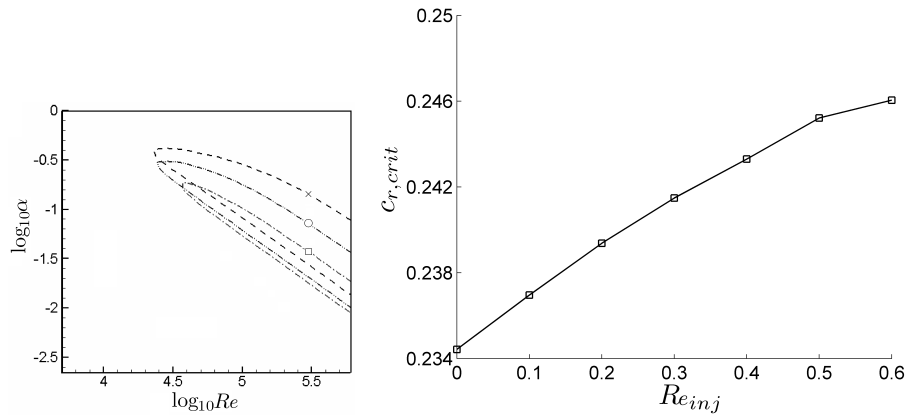

(a) (b)

Figure 4.6: Critical values for $k = 0.5$: (a) neutral stability curves for $Re_{inj} = 0\,(\times)$, $0.3\,(\circ)$ and $0.53\,(\square)$; (b) variation in $c_{r,crit}$ with Re_{inj}.

Re_{inj}	α_{crit}	Re_{crit}	$c_{r,crit}$
0	0.3851	22600	0.2344
0.1	0.3576	22538	0.2370
0.2	0.3275	22924	0.2394
0.3	0.2950	23986	0.2415
0.4	0.2550	26321	0.2433
0.5	0.2000	31656	0.2452
0.6	0.1200	51115	0.2461

Table 4.1: Critical values for $k = 0.5$ and increasing Re_{inj}.

a long wavelength approximation in order to predict $k_1(Re_{inj})$. Figure 4.6(b) plots the values of c_r at criticality, as Re_{inj} is varied, also for $k = 0.5$. The critical values are tabulated in Table 4.1. The dependence is initially linear. We observe that $k > c_{r,crit}$ over the computed range.

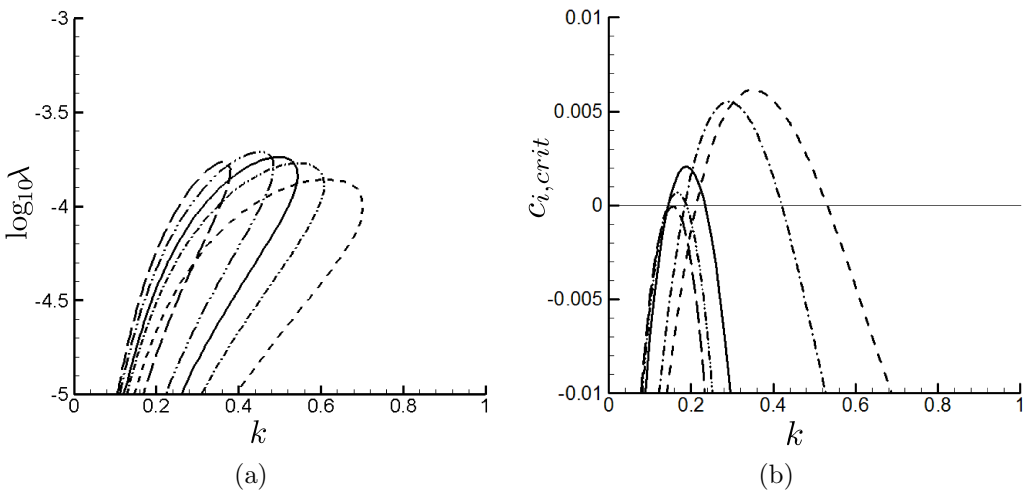

Figure 4.7: (a) Long wave NSC's showing the dependence of λ on k for $Re_{inj} = 0$ (dashed line), 0.3 (dash-dot), 0.5 (solid), 0.7 (dash-dot-dot) and 1 (long dash); (b) $c_{i,crit}$ versus k for $\lambda = 2.5 \times 10^{-5}$, and $Re_{inj} = 0$ (dashed line), 0.3 (dash-dot), 1 (solid), 1.2 (dash-dot-dot) and 1.3 (long dash).

4.3.1 Long wavelength approximation

We follow the long wavelength distinguished limit approach of Cowley & Smith (1985), taking $\alpha \to 0$ and $Re \to \infty$, with $\lambda = (\alpha Re)^{-1}$ fixed. The product αRe is fixed along the upper and lower branches of the NSC. Thus, as the two branches of the NSC coalesce, in the (k, λ)-plane we observe $k \to k_1(Re_{inj})$. In the long wavelength limit, equation 4.13 becomes:

$$i\lambda \left[D^4 - Re_{inj} D^3\right] \phi + (u - c)\, D^2\phi - (D^2 u)\phi = 0, \tag{4.18}$$

with boundary conditions (4.14).

Figure 4.7(a) shows the NSC obtained from (4.18), plotted in the (k, λ)-plane for various Re_{inj}. The cut-off value $k_1(Re_{inj})$ is the maximal value of k

$Re_{inj,1}$	k_1	$c_{r,crit}$	$\tilde{k}(k_1, Re_{inj,1})$
0	0.70	0.2331	0.5070
0.3	0.60	0.2431	0.4657
0.5	0.54	0.2455	0.4386
0.7	0.48	0.2472	0.4085
1.0	0.38	0.2358	0.3489
1.29	0.19	0.1556	0.1939

Table 4.2: Cut-off values, k_1, and wavespeed $c_{r,crit}$, for increasing Re_{inj}.

on each of these curves. These values are listed in Table 4.2. We also list the dimensionless wall speeds at cut-off, i.e. $\tilde{k}(k_1, Re_{inj})$. We observe that the cut-off wall speed decreases with Re_{inj}. This is in agreement with the concluding remarks of §4.2.3.

Figure 4.7(b) shows c_i for the least stable eigenvalue of the long wavelength problem, for fixed $\lambda = 2.5 \times 10^{-5}$ and different values of Re_{inj}, as k is varied. When $Re_{inj} \geq 1.3$, we find that $c_{i,crit} \leq 0$, $\forall\ k \in (c_{r,crit}, k_1(0)]$, implying that there are no neutral or unstable long wavelength perturbations in this range of k, (i.e. at least until we approach the second transition at $Re_{inj,2}$). Thus, in this initial range of say $Re_{inj} \lesssim 1.3$, provided that $k > c_{r,crit}$, we can talk equally of a cut-off value for k or for Re_{inj}.

4.3.2 Effects of asymmetry of the velocity profile

We observe that Re_{inj} enters the stability problem in two distinct ways. The first one represents the direct contribution of the additional third order inertial term, $Re_{inj}D(\alpha^2 - D^2)\phi$, in the O-S equation (4.13). For the second one,

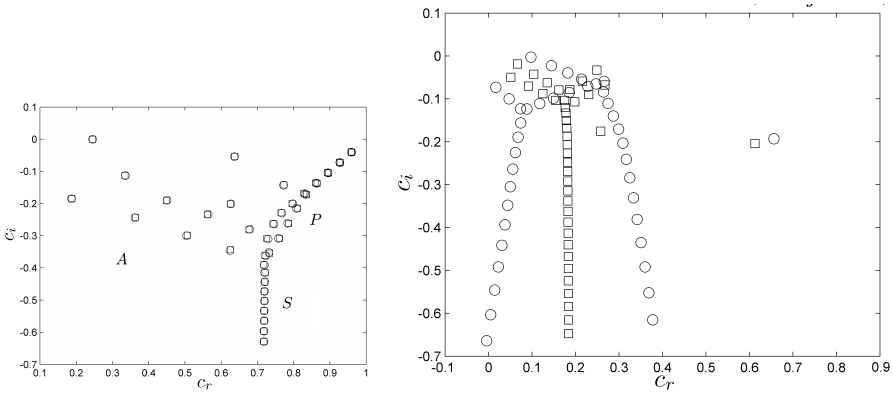

(a) (b)

Figure 4.8: Eigenspectrum for (k, α, Re) = (0.5, 0.2, 31656) (a) Re_{inj} = 0.5 (Critical Conditions) and (b) $Re_{inj} = 23.5$. Symbol $\circ$ indicates the eigenspectrum from the O-S equation while $\square$ indicates the spectrum obtained by neglecting the additional cross-flow inertial term.

Re_{inj} influences the base velocity profile. To explore which of these effects is dominant, we show in Fig. 4.8 the spectra of (4.13)–(4.14) obtained with and without the term, $Re_{inj}D(\alpha^2 - D^2)\phi$, included in the computation. The critical parameters corresponding to $Re_{inj} = 0.5$, in Table 4.1, are chosen and fixed for this comparison. Figure 4.8(a) shows the two spectra at $Re_{inj} = 0.5$, which are near identical, completely overlapping on the figure. This suggests that at smaller Re_{inj}, the effects of cross-flow manifest completely via the base flow velocity profile. Figure 4.8(b) shows a similar comparative study at a larger value of Re_{inj}, closer to $Re_{inj,2}$. In this figure we see a distinct difference between the spectra. The additional third order term is apparently responsible for the splitting of the A, P, and S families, illustrated earlier in Fig. 4.3(b).

In Fig. 4.9, we plot k_1 against $Re_{inj}(= Re_{inj,1})$. A linear dependence is evident. The slope of the line is approximately $-1/3$. The flow is unconditionally linearly stable above the line and conditionally unstable otherwise. For small values of Re_{inj}, we have seen in Fig. 4.1 that the principal effect is to skew the velocity profile towards the upper wall. A similar asymmetric skewing of the velocity profile is also induced in an annular Couette-Poiseuille (ACP) flow, through geometric means by varying the radius ratio, η, (defined as the radius of the outer stationary cylinder to the radius of inner moving cylinder). ACP flow has been studied extensively by Sadeghi & Higgins (1991), and we superimpose their results on ours, in Fig. 4.9. The comparison is striking. We believe there are 2 features of Fig. 4.9 that are unusual and worthy of note. Unsurprising is of course the identical limits $Re_{inj} = 0 = (\eta - 1)$. Note that $Re_{inj} \to 0$ is the PCP flow, and $\eta \to 1$ represents the narrow gap limit of ACP, which is also the PCP flow.

The first feature is the very similar linear decay in critical $k = k_1(Re_{inj})$, from the PCP values. It can be argued along the lines of Mott & Joseph (1968), that for a fixed Couette component (k), increasing the cross-flow for the PCP flow, or the radius ratio in the ACP flow of Sadeghi & Higgins (1991), skews the velocity profile more towards the moving boundary, thus increasing asymmetry and thereby stability. Since it has been already observed in Fig. 4.8(a) that for small Re_{inj} the influence of injection on the eigenspectrum is through the velocity profile only, we do expect stabilization. However, when $(\eta - 1)$ and Re_{inj} are of $O(1)$, we can see no obvious quantitative relation between these

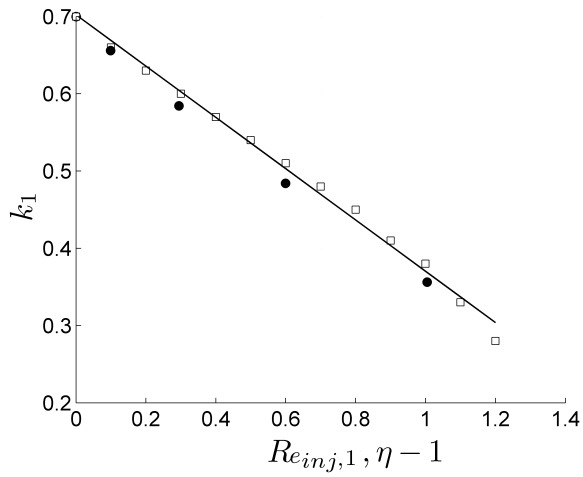

Figure 4.9: k_1 as a function of $Re_{inj,1}$ (shown by □) and the radius ratio, η (shown by ●) in ACP flow (Sadeghi & Higgins (1991))

flows and even the stability operators are quite different.

The second noteworthy feature of Fig. 4.9 is that there is a minimum value of k_1 ($k_{1,min}$) below which it is not possible to produce unconditional stability by applying (modest) cross-flow. This minimum value is found when $k_1 \rightarrow c_{r,crit}$. We have found approximately that $k_{1,min} = 0.19$ and the corresponding $Re_{inj,1} = 1.29$. This is very similar to Sadeghi & Higgins (1991), who found that the critical layer near the moving wall of ACP flows remained up to $c_{r,crit} \approx 0.18$.

Linear energy budget considerations

The strong analogy with the ACP results of Sadeghi & Higgins (1991) suggests that a similar mechanism may be responsible for the stabilization and cut-off behaviour. To investigate this we examine the linear energy equation,

derived in modal form from the Reynolds-Orr energy equation. This yields the following two identities:

$$c_i = \frac{\langle(\phi_r D\phi_i - \phi_i D\phi_r)Du\rangle - \dfrac{1}{\alpha Re}[I_2^2 + 2\alpha^2 I_1^2 + \alpha^4 I_0^2]}{I_1^2 + \alpha^2 I_0^2}, \tag{4.19}$$

$$c_r = \frac{\langle(\alpha^2|\phi|^2 + |D\phi|^2)u\rangle + \dfrac{Re_{inj}}{\alpha Re}\langle\alpha^2(\phi_r D\phi_i - \phi_i D\phi_r) + (D\phi_r D^2\phi_i - D\phi_i D^2\phi_r)\rangle}{I_1^2 + \alpha^2 I_0^2} \tag{4.20}$$

where $I_k = I_k(\phi)$ is the semi-norm defined by:

$$I_k = \left[\int_{-1}^{1} |D^k\phi|^2 \, \mathrm{d}y\right]^{1/2}, \quad k = 0, 1, 2,$$

and where

$$\langle f\rangle = \int_{-1}^{1} f(y) \, \mathrm{d}y.$$

Before proceeding further, we note that Re_{inj} only appears indirectly in (4.19), reinforcing the assertion that for order unity Re_{inj}, the principle contribution to stability of injection is via the mean flow. Indeed, in the long wavelength limits of cut-off k that we have studied, we have found values $\lambda = (\alpha Re)^{-1} \lesssim 10^{-4}$ for instability. Thus, in (4.20) the term directly involving Re_{inj} has minimal effect on c_r, explaining the observations in Fig. 4.8(a).

The identity (4.19) can also be interpreted as an energy equation, in form:

$$\frac{d}{dt}\langle T_1\rangle = \langle T_2\rangle - \frac{1}{Re}\langle T_3\rangle \tag{4.21}$$

where

$$T_1 = 0.5\left(|D\phi|^2 + \alpha^2 |\phi|^2\right), \qquad \frac{\mathrm{d}}{\mathrm{d}t}T_1 = \alpha c_i T_1, \tag{4.22}$$

$$T_2 = 0.5\alpha\tau Du, \qquad \tau = \phi_r D\phi_i - \phi_i D\phi_r, \tag{4.23}$$

$$T_3 = 0.5(\left|D^2\phi\right|^2 + 2\alpha^2 |D\phi|^2 + \alpha^4 |\phi|^2). \tag{4.24}$$

The left-hand side of (4.21) represents the temporal variation of the spatially averaged (one wavelength) kinetic energy. The first term on the right-hand side of (4.21) is the exchange of energy between the base flow and the disturbance. The last term, $\left(\frac{1}{Re}\langle T_3\rangle\right)$, represents the rate of viscous dissipation. At criticality, the two terms on the right-hand side balances each other, but the spatial distributions of T_2 and T_3/Re indicate where the energy is generated and dissipated in the channel.

Sadeghi & Higgins (1991) extensively utilised this linear energy approach in studying the effect of k on stability of ACP flow. They found that increase in the value of $k - c_{r,crit}$ decreases the Reynolds stress (τ) near the moving wall until it becomes negative, hence stabilizing. The critical layer near the moving wall vanishes for $k > c_{r,crit}$ and as k increases the Reynolds stress becomes progressively negative within the critical layer at the fixed wall, but this behavior is destabilizing since the velocity gradient is negative there for ACP flow.

Figures 4.10(a)-(d) examine the distribution of T_2 and T_3/Re for the least stable eigenmode for the parameters listed in Table 4.1, i.e. we fix $k = 0.5$ and

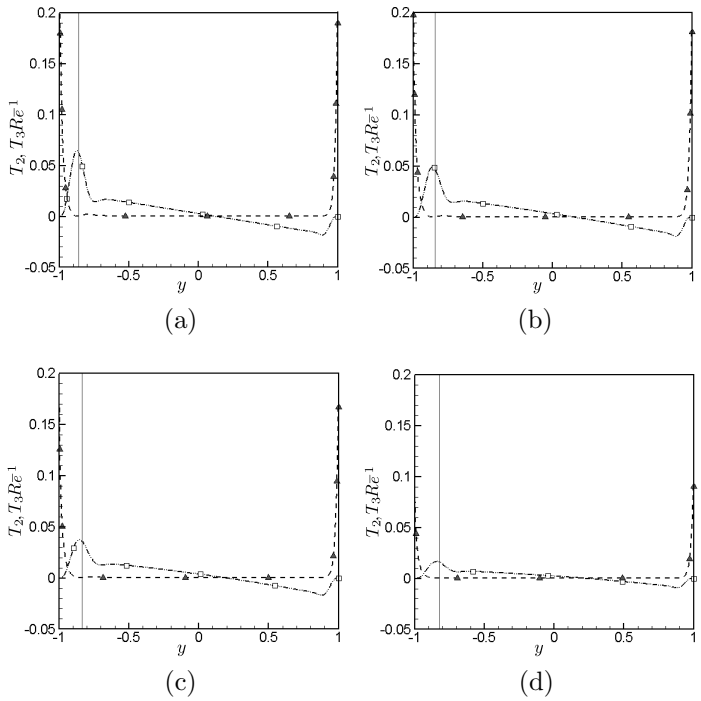

Figure 4.10: Distribution of energy production (T_2) and dissipation ($\frac{1}{Re}T_3$) terms across the domain corresponding to criticality at Re_{inj}= (a) 0, (b) 0.2, (c) 0.4 and (d) 0.6. In all the cases, $k = 0.5$. Dash-dot-dot line with symbol $\square$ represents T_2, dashed line with filled $\triangle$ represents $\frac{1}{Re}T_3$ and solid vertical line represents the location of the critical layer.

increase Re_{inj} up to $Re_{inj} = Re_{inj,1} \approx 0.6$. The critical layer is marked with a vertical line. We observe that both the rate of energy transfer and the rate of viscous dissipation decrease with the cross-flow. Without cross-flow, T_2 is positive and negative respectively in the lower (injection) and upper (suction) halves of the domain. Increasing the cross-flow decreases both the positive (near injection wall) and negative (near suction wall) peaks. The location of the critical layer also moves away from the injection wall due to the skewing of the velocity profile. When $Re_{inj} \approx Re_{inj,1}$, $\langle T_2 \rangle$ and $\frac{1}{Re}\langle T_3 \rangle$ not only equalize

but (since ϕ has been normalised), will have magnitudes $O(\alpha^{-1})$ since $\alpha Re =$ constant at cut-off; (see also Sadeghi & Higgins (1991)). This reduced energy budget as $Re_{inj} \approx Re_{inj,1}$. This is the primary reason for the cut-off.

4.3.3 Summary

For the range of small to order unity Re_{inj} with $k \geq c_{r,crit}$, the flow instability is dominated by long wavelength perturbations. This instability mchanism exhibits a cut-off phenomenon characterised by a near linear boundary in the (Re_{inj}, k)-plane. The initial cut-off mechanism is very similar to that for ACP, as studied by Sadeghi & Higgins (1991), combining skewing of the velocity profile, shifting of the critical layer and decay of the net perturbation energy.

4.4 Intermediate Re_{inj} and short wavelength instabilities

We now consider the range $0 \leq k \leq c_{r,crit}$, in which the critical layer at the upper wall is still present. We investigate its stability characteristics by adding cross-flow of intermediate strength ($0 \leq Re_{inj} \lesssim 21$), avoiding for the moment the second transition. It is intuitive that the presence of the critical layer will affect the stability behavior. To verify this we have studied the two extremities of the range of k considered, i.e. $k = 0$ (PP flow) and $k = 0.18$. The respective NSCs are shown in Fig. 4.11. It is evident that the presence of the critical

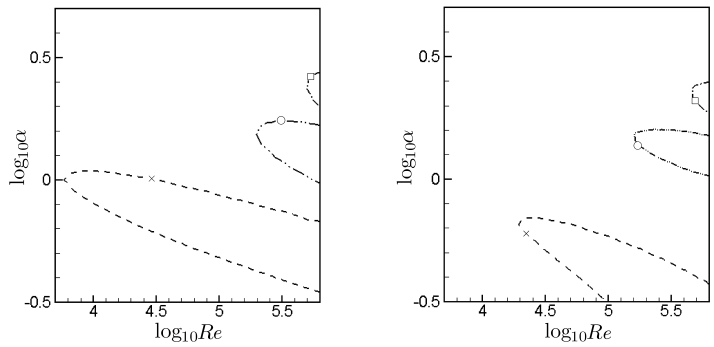

Figure 4.11: Neutral Stability Curves (NSCs) for (a) $k = 0$ and (b) 0.18 at different Re_{inj}. The symbols indicate different values of Re_{inj} and are as follows: $\times \rightarrow Re_{inj} = 0$, $\circ \rightarrow Re_{inj} = 6$ in (a) and 4 in (b), $\square \rightarrow Re_{inj} = 12$ in (a) and 8 in (b)

layers render shorter wavelength modes unstable. Yet, it is also observed that with Re_{inj} in this intermediate range, the stability increases dramatically.

We have been unable to make any advance analytically in this range of Re_{inj}, and therefore have proceeded numerically. First we note that when we have considered $k \gtrsim 0.19$ for the range of $1.3 < Re_{inj} < 21$, we have found that the least stable modes are long wavelength modes and that these are linearly stable. Thus, $k \gtrsim 0.19$ appears to represent an absolute cut-off in this range of Re_{inj}.

For smaller k we have seen that the NSC's occur with wavenumbers that are $O(1)$ and apparently increasing with Re_{inj}. Unlike the long wavelength problem, the asymptotic behaviour along the branches of the NSC's is not easily treated. At fixed large Re, we are able to compute numerically a cut-off value of k for increasing Re_{inj}, i.e. $k = k_1(Re_{inj}, R)$. These cut-off curves do

k_1	$Re_{inj,1}$	α_{crit}
0	20.8	3.5227
0.0225	20.6	3.7458
0.0450	20.0	3.9381
0.0675	18.6	3.9831
0.0900	15.6	3.4146
0.1125	14.4	3.2112
0.1350	13.4	3.2112
0.1575	12.6	3.2112
0.1800	11.8	3.2112

Table 4.3: Cut-off values evaluated for shorter wavelength instabilities for $Re = 10^6$.

lie below $k \sim 0.19$, but are not wholly independent of Re, at least within the range of Re up to which our numerical code is reliable, i.e. it is quite possible that these asymptote to a cut-off curve as $Re \to \infty$, but we cannot reliably evaluate this limit numerically. As an example of this numerical cut-off, (at $Re = 10^6$), we have computed the cut-off values $Re_{inj,1}$, as listed in Table 4.3 and shown in Fig. 4.12(a). For the range $1.4 < Re_{inj} < 11.8$, the cut-off is close to $k \sim 0.19$.

Although we see that the unstable wavenumbers increase with Re_{inj} in Fig. 4.11, note that asymptotically as $\alpha \to \infty$ the short wavelengths are stable. To see this, from (4.19) we bound

$$\langle(\phi_r D\phi_i - \phi_i D\phi_r)Du\rangle \leq |Du|_{max} I_0 I_1 \leq 0.5|Du|_{max}[\alpha I_0^2 + I_1^2/\alpha],$$

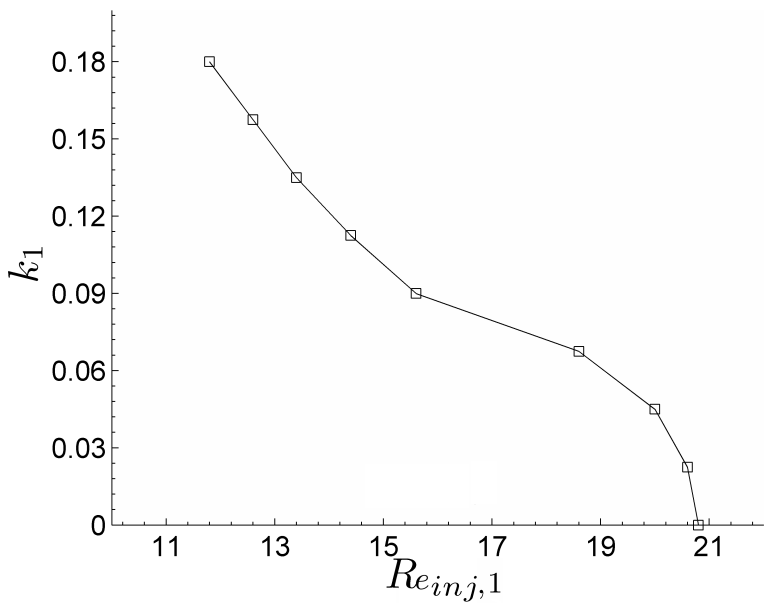

Figure 4.12: Shorter wavelength cut-off showing k_1 as a function of $Re_{inj,1}$. The flow is linearly stable for $Re \leq 10^6$ above the curve. The values in Table 4.3 are marked by $\square$.

so that $c_i < 0$ provided that:

$$Re < \frac{|Du|_{max}}{2\alpha^2}, \tag{4.25}$$

(and better bounds are certainly possible). In Table 4.3 we note that the maximal critical wavenumber is in fact attained at an intermediate Re_{inj}.

4.4.1 Behaviour of preferred modes for intermediate Re_{inj}.

In our preliminary results, (§4.2.3), we saw that at fixed values of (Re, k, α), increasing the Re_{inj} led to regimes of stabilization, then destabilization, and then finally stabilization. For $k \geq c_{r,crit}$, only long wavelengths appear unstable and how the cut-off values of k and Re_{inj} vary in this regime are illustrated in Fig. 4.9. For the lower range of k, our results are primarily numerical, indicating a cut-off value $k \approx 0.19$ for $1.3 \lesssim Re_{inj} \lesssim 11.8$ and then with decaying cut-off k for $11.8 \lesssim Re_{inj} \lesssim 20.8$, as illustrated in Fig. 4.12. Therefore, we have linear stability as we cross some cut-off frontier, $k > k_1(Re_{inj})$ in the (Re_{inj}, k)-plane, (alternatively for $Re_{inj} > Re_{inj,1}$).

We now consider what happens to the certain eigenmodes (preferred modes) as we extend the injection cross-flow up until the second critical Re_{inj}. Our analysis up to now suggests that the behaviour may be different depending on whether we consider small or moderate k. In Fig. 4.13, we have plotted the locations of certain eigenmodes as Re_{inj} is increased, by keeping the Reynolds number Re constant at 10^6. This gives us some idea of how cut-off behaviour changes with Re_{inj}. Although the "preferred modes" are simply those we have selected, we implicitly mean modes that are involved in the transition from stable to unstable as one of our dimensionless parameters is varied (here Re_{inj}), i.e. at some point a preferred mode becomes the least stable mode and then unstable.

Figure 4.13(a) shows two eigenmodes corresponding to $k = 0$, (PP flow). A least stable long wavelength mode is tracked for $\alpha = 0.001$, denoted by 'A'. This mode is stable at $Re_{inj} = 0$ and its stability increases further as Re_{inj} increases up to around 1.7. However, further increases in Re_{inj} destabilize this mode progressively until it becomes unstable at $Re_{inj} = 25$. In the inset of Fig. 4.13(a) we have also plotted the least stable short wavelength mode at $\alpha = 3.5227$. Such modes become unstable only under the influence of cross-flow of intermediate strength. This particular mode, (denoted by 'B'), starts becoming unstable approximately when $Re_{inj} > 15$, but recovers stability later for $Re_{inj} \geq 20.8$. This behavior is a direct consequence of the trajectory of the NSCs observed in Fig. 4.11(a). The preferred mode 'B' is the critical mode at cut-off, (see Table 4.3). Thus PP flow with cross- flow is unconditionally linearly stable in the range $20.8 \leq Re_{inj} \lesssim 25$.

For larger k, the stability behavior is primarily governed by the long wavelength modes, as shown in Fig. 4.13(b) for $k = 0.5$. The least stable mode corresponding to $\alpha = 0.01$ is unstable for $Re_{inj} = 0$, denoted mode 'C'. This viscous mode becomes stable when Re_{inj} increases to 0.6, which is indeed the cut-off value, i.e. $Re_{inj,1}$. This is expected, according to Table 4.2. Mode 'C' is weakly damped and its stability increases for $Re_{inj} \lesssim 3$, after which it starts destabilizing. The mechanism of this destabilization can probably be analysed along the lines of resonant interactions of the Tollmien-Schlichting (T-S) waves; see Baines *et al.* (1996). To show this interaction, we have traced the locus, (for $Re_{inj} = [7, 30]$), of the least stable inviscid short wavelength mode 'D', at

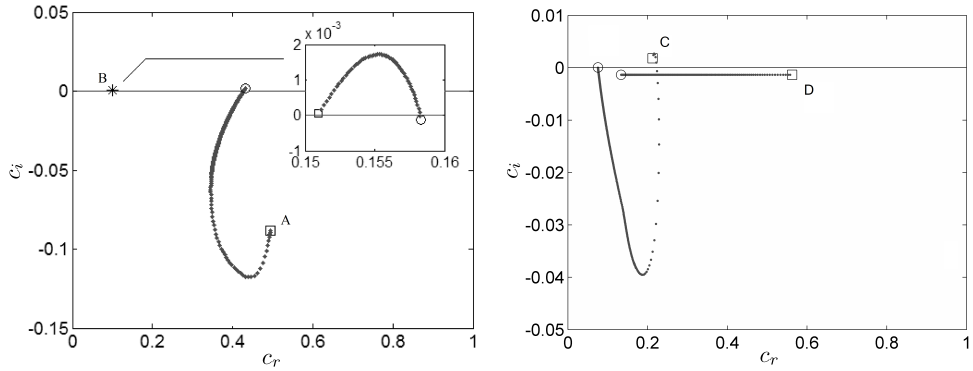

(a) (b)

Figure 4.13: Behavior of preferred modes (belonging to different wavelengths and denoted by alphabets 'A'-'D') under the influence of cross-flow with $Re = 10^6$. Symbols □ and ∘ respectively imply the starting and the ending position of the preferred mode in the c_i, c_r plane, whereas the dots ('.') trace the locus. The difference in Re_{inj} between consecutive dots is 0.1. (a) $k = 0$. Mode 'A' has $\alpha = 0.001$ and is traced for Re_{inj}=[0,25]. Mode 'B' has $\alpha = 3.5227$ and is traced for Re_{inj}=[15,21] (shown in the inset), the position at $Re_{inj} = 15$ is marked by '$*$'. (b) $k = 0.5$. Mode 'C' has $\alpha = 0.01$ and is traced for Re_{inj}=[0,30]. Mode 'D' has $\alpha = 2.5$ and is traced for Re_{inj}=[7,30].

$\alpha = 2.5$. This mode, being inviscid, remains stable but has c_i very close to zero as Re_{inj} increases. The wave speed c_r decreases continuously with Re_{inj} for mode 'D'. The resonant interaction takes place when its wave speed matches with that of mode 'C', which signals the destabilization of mode 'C'. This destabilization continues until mode 'C' becomes unstable when $Re_{inj} \gtrsim 30$.

In Fig. 4.14 we show examples of the streamfunction for the preferred modes, corresponding to various k and Re_{inj} in the transitions of Fig. 4.13. For the long wavelength mode 'C', Figs. 4.14(a)-(c) show that strong Re_{inj} appears to skew the streamlines towards the lower wall. The same is true for the long wavelength mode 'A' under strong injection; see Fig. 4.14(f). On the

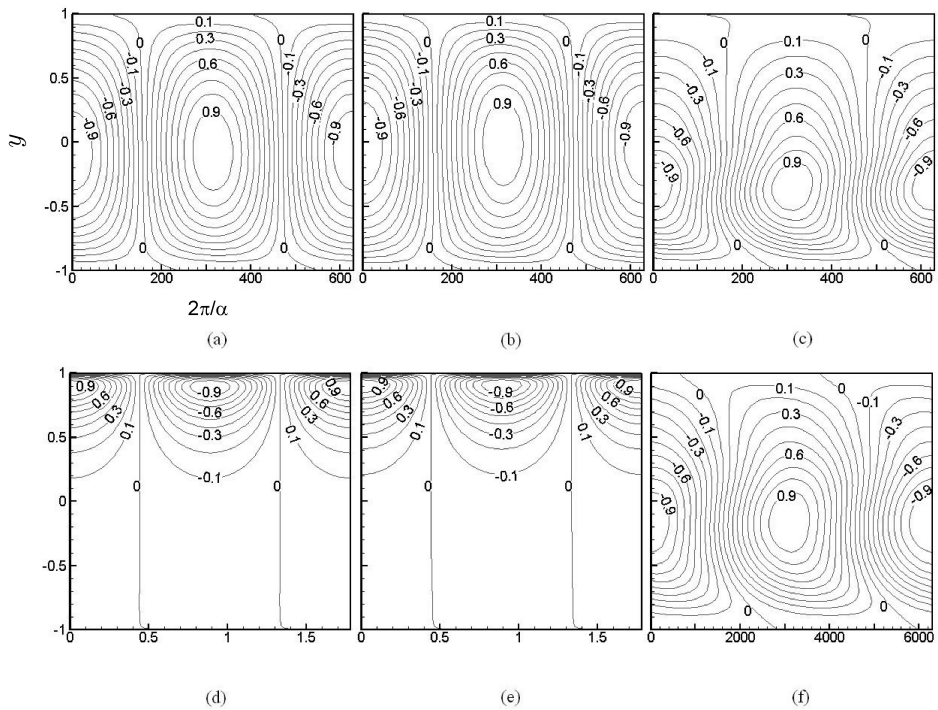

Figure 4.14: Isovalues of the normalised perturbation stream functions (ψ') for the preferred modes at $Re = 10^6$ under different Re_{inj}. The streamwise extent of the domain is one wavelength. Corresponding to $k = 0.5$, the long wavelength mode 'C' is shown for (a) $Re_{inj} = 0.1$ (unstable), (b) $Re_{inj} = 1$ (stable) and (c) $Re_{inj} = 30$ (unstable). Corresponding to $k = 0$, ψ' for two different preferred modes, viz. 'A' and 'B' are shown. The shorter wavelength mode 'B' ($\alpha = 3.5227$) is shown for (d) $Re_{inj} = 15$ (unstable) and (e) $Re_{inj} = 21$ (stable). The longer wavelength mode 'A' ($\alpha = 0.001$) is shown for (f) $Re_{inj} = 25$ (unstable).

contrary, Figs. 4.14(d)-(e) show that for large Re_{inj}, the streamlines of the shorter wavelength mode 'B' are skewed and localised towards the upper wall.

4.5 Stability and instability at large Re_{inj}.

We turn now to the transition to instability at $Re_{inj,2}$ and then later to stabilizing effects at very large Re_{inj}. As observed in §4.2.3, the transition at $Re_{inj,2}$ appears to be independent of streamwise Reynolds number Re (see Fig. 4.4(b)) and occurs for all k. Although there is sensitivity to k, it is not very significant. Values of $Re_{inj,2}$ are found for all $k \in [0, 1]$ and are in a fairly tight range of $Re_{inj} \sim 22 - 25$.

As suggested in the previous subsection, although instability at moderate Re_{inj} may be either short wavelength or long wavelength, according to $(k - c_{r,crit})$, as we approach $Re_{inj,2}$ from below it is the long wavelengths that are unstable. Figure 4.15a shows the neutral stability curves corresponding to PP flow for Re_{inj} just above $Re_{inj,2}$. The NSC's are nested with decreasing Re_{inj} and as we approach $Re_{inj,2}$ the upper and lower branches of the NSC are seen to coalesce. The slope of the two branches suggests that $\alpha \sim R^{-1}$ in the limit of cut-off, and hence the previous long wavelength approximation, leading equation (4.18), should be effective for predicting the cut-off in the (k, λ)-plane; (recall $\lambda = (\alpha R)^{-1}$).

Figure 4.15b shows the NSC's obtained from long wave approximation. The cut-off velocity k_2 is the maximum value of k encountered along the NSC

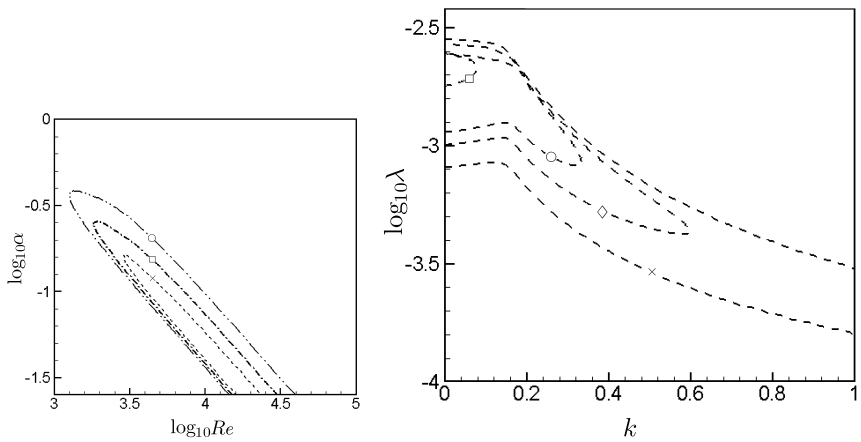

(a) (b)

Figure 4.15: (a) NSC of PP flow ($k = 0$) when $Re_{inj} \to Re^{-}_{inj,2}$. The different values of Re_{inj} are 22.5 (dashed line with $\times$), 23 (dash-dot line with $\square$) and 24 (dash-dot-dot line with $\circ$). Near cut-off, αRe is constant along the upper and lower branches. (b) Long wave NSCs showing the dependence of $\log_{10}\lambda$ on k. The different values of Re_{inj} are 22.4 ($\square$), 23.5 ($\circ$), 24 ($\diamond$) and 25 ($\times$). Cut-off is achieved over the entire range of k, i.e. $[0, 1]$.

for a given $Re_{inj} = Re_{inj,2}$. Unlike Fig. 4.7, the entire range of k becomes unconditionally stable. For $Re_{inj,1} < Re_{inj} < 22.2$, $c_i < 0 \ \forall \ k \in [0, 1]$. Another significant difference with Fig. 4.7 and the results of Cowley & Smith (1985) is that "bifurcation from infinity" is not observed as $k \to 0$. This is possibly because the curves bifurcate from infinity for negative values of k, but we have not studied this range. Finally, we mention that for cross-flow rates slightly greater than $Re_{inj,2}$, the Re_{crit} is relatively low for the entire range of k. For example, $Re_{inj,2} \approx 23.8$ for $k = 0.5$, (implying $Re_{crit} \to \infty$ as $Re_{inj} \to Re^{-}_{inj,2}$). Increasing Re_{inj} to 25 decreases Re_{crit} to around 6000. Thus, on crossing $Re_{inj,2}$ we find a dramatic decrease in the flow stability.

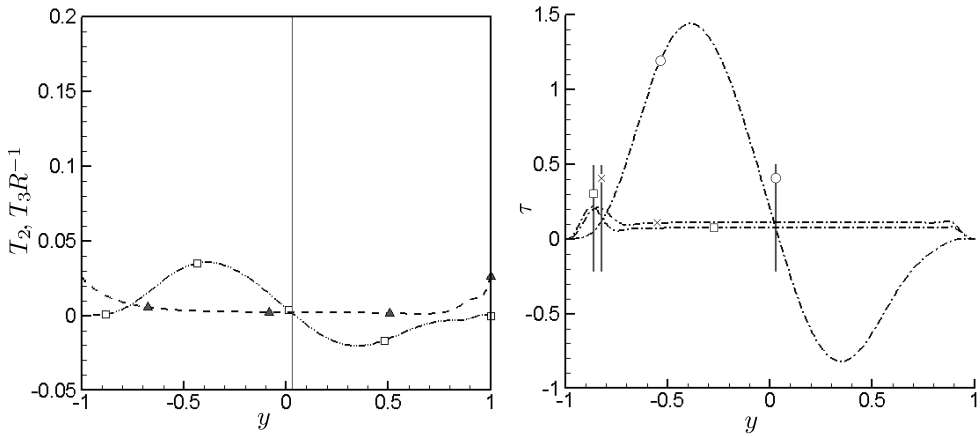

(a) (b)

Figure 4.16: (a) Distribution of energy production (T_2) and dissipation ($\frac{1}{Re}T_3$) terms across the domain corresponding to criticality at $Re_{inj} = 25$. Dash-dot-dot line with symbol $\square$ represents T_2, dashed line with filled $\triangle$ represents $\frac{1}{Re}T_3$ and solid vertical line represents the location of the critical layer. (b) Reynolds Stress τ distribution at criticality for $Re_{inj} = 0$ (denoted by $\square$ symbol), $Re_{inj} = 0.6$ (denoted by $\times$) and $Re_{inj} = 25$ (denoted by $\circ$). The location of the critical layers are shown by solid lines with corrosponding symbols.

4.5.1 Linear energy balance at $Re_{inj,2}$

An interesting feature of transition at $Re_{inj,2}$ is the independence with respect to Re. With reference to the energy equation (4.21), this insensitivity implies that in this range $|T_2|$ is much larger than the viscous dissipation, $\frac{1}{Re}T_3$. In other words, at criticality $c_i = 0$ is achieved by a balance of energy production and dissipation within T_2, more so than via balance with the viscous dissipation. Figure 4.16(a) investigates the energy budget at criticality for $k = 0.5$ at $Re_{inj} = 25$. The critical parameters are observed to be $(\alpha_{crit}, Re_{crit}) = (0.31, 6000)$. This implies that crossing the cut-off $Re_{inj,2}$, there is a transition from unconditional stability ($Re_{crit} \to \infty$) to high

instability($Re_{crit} = 6000$). Comparing with Fig. 4.10 (which shows energy distribution corresponding to criticality for $k = 0.5$ and $Re_{inj} \leq Re_{inj,1}$) , it is obvious that T_2 has a higher amplitude while the viscous dissipation $\frac{1}{Re}T_3$ is weaker.

This behavior is due to the generation of larger Reynolds stresses τ, as Re_{inj} increases, as illustrated in Fig. 4.16(b). The dominance of T_2 over the viscous dissipation suggests that the critical layers have little to do with instability in this range. Note that τ is small in the critical layer, which has now moved towards the channel centre, and hence T_2 is also small. Referring to Fig. 4.2(b), the vanishing vorticity gradient (D^2u) found in the bulk of the flow domain at high values of Re_{inj} removes/diminishes the singular effects associated with the critical layer.

The growth of τ is probably not responsible for the spreading of the spectrum along the real axis, that we have observed in Fig. 4.3(b). Equation (4.20) may be rewritten as:

$$c_r = \frac{\langle(\alpha^2|\phi|^2 + |D\phi|^2)u\rangle + \dfrac{Re_{inj}}{\alpha Re}\langle\alpha^2\tau - \phi_r D^3\phi_i + \phi_i D^3\phi_r\rangle}{I_1^2 + \alpha^2 I_0^2}. \tag{4.26}$$

The first term leads simply to values of c_r in the range of u. The second term does contain $\alpha^2\tau$, i.e. longitudinal gradients of the Reynolds stresses. However, note that even for the shorter wavelengths we have $\alpha \sim O(1)$, and if we consider long wavelengths, we have typically found instability only for

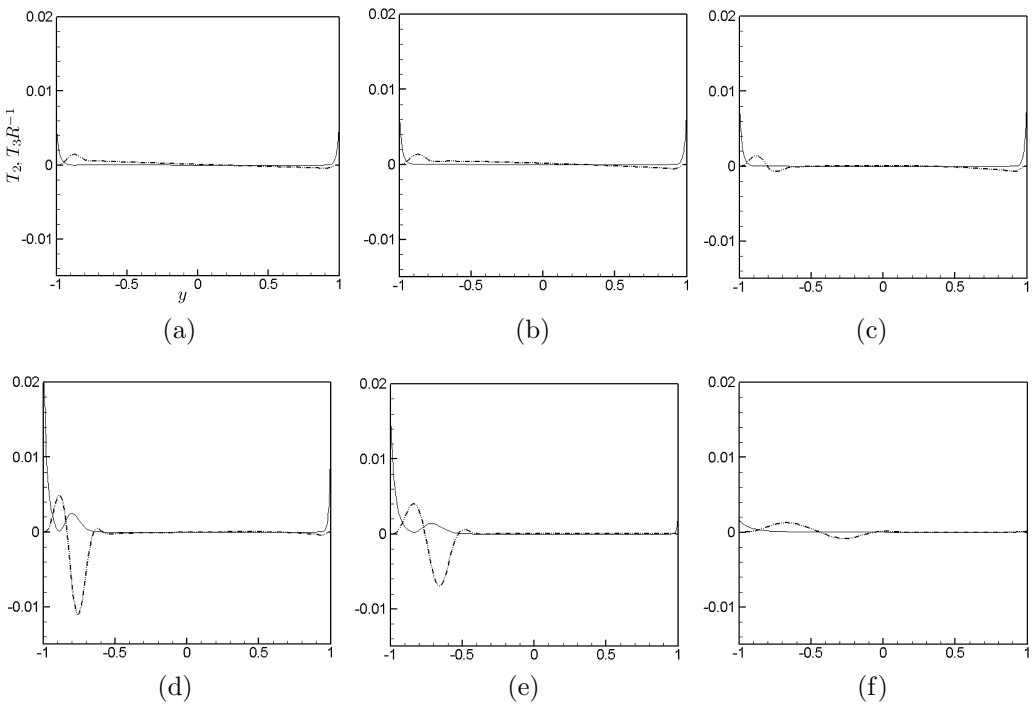

Figure 4.17: Distribution of energy production (T_2) and dissipation ($\frac{1}{Re}T_3$) terms across the domain corresponding to mode 'C' at Re_{inj}= (a) 0, (b) 0.6, (c) 1, (d) 3, (e) 10 and (f) 30. Dash-dot-dot line represents T_2, solid line represents $\frac{1}{Re}T_3$.

$\alpha Re \gg 1$. Thus, even for these larger Re_{inj}, the term involving $\alpha^2\tau$ is likely to be insignificant.

The extension of c_r beyond the usual bounds of the base flow velocity is therefore due to the 3rd derivative terms in (4.26), which cannot be bounded by the denominator. Interestingly therefore, the larger values of c_r, which indicate less regular eigenmodes, also lead to larger viscous dissipation, and hence more stable modes. This explains the shape of the spectrum in Fig. 4.3(b).

In Fig. 4.13(b), we tracked the behaviour of mode 'C' as Re_{inj} increased.

This mode becomes unstable for $Re_{inj} \geq Re_{inj,2}$, implying that it governs the transition behavior. In Fig. 4.17 we show the evolution of the energy balance terms for this mode as Re_{inj} increases from zero. This mode is stable from $Re_{inj} = 0.6$ to 30. The cut-off achieved at $Re_{inj} = 0.6$ is primarily due to the increased viscous dissipation at both walls. This phenomenon continues until $Re_{inj} \approx 3$, see Fig. 4.17(d). At this point, the 'viscous hump' observed near the lower wall gets amplified. This mechanism is probably due to the resonant interaction between mode 'C' and an (approximately) neutrally stable inviscid mode ,for example mode 'D'. Further increase in Re_{inj} thins out the viscous layer at the suction wall faster than that at the injection wall. Suction negates both the exchange as well as the dissipation of energy, and the viscous hump is localised within the lower half of the channel, i.e. injection side. $\frac{1}{Re}T_3$ reduces faster than T_2 and finally the mode becomes unstable when Re_{inj} increases to 30. The condition at this point is $\langle T_2 \rangle > \frac{1}{Re} \langle T_3 \rangle$; see Fig. 4.17(f). It is interesting to observe that the mode becomes unstable when the viscous hump reaches the centre of the channel. Further increase of Re_{inj} results in a gradual reduction of T_2 and the mode becomes stable again. The mean perturbation kinetic energy $q(y)$ distribution provides further insight into the instability mechanism. It is defined modally to be:

$$q = \frac{1}{4} \left(|D\phi|^2 + \alpha^2 |\phi|^2 \right) \tag{4.27}$$

Figure 4.18 shows the mean perturbation kinetic energy profiles for mode 'C'

at different Re_{inj}. Each distribution of q has been normalised by its maximum value.

Without any cross-flow, the amount of energy in the two halves of the domain are comparable, the suction half having $\sim 43\%$ of the energy, (note $k = 0.5$). Increasing cross-flow up to $Re_{inj} \approx Re_{inj,1} = 0.6$ increases the secondary peak until the cut-off is achieved. The energy in the suction half at this point is 46.7%. The primary peak moves toward the lower wall but cannot reach it because of the no-slip conditions. At $Re_{inj} > 1$, the primary peak starts moving away from the suction wall. At $Re_{inj} = 3$, the mode is at its maximum stability (see Fig. 4.13(b)). At this point, the perturbation energy is highly localised within the lower $\frac{1}{8}$th of the channel, along with a small secondary peak at the upper quarter. Further increase of Re_{inj} to 10 causes the secondary peak to vanish; the energy content in the suction half being only $\sim 7.6\%$. The resonant interactions of T-S waves result in the development of a secondary peak from the primary peak itself. During this process, the secondary peak slowly separates from the primary peak and moves in the direction of the upper wall. For $Re_{inj} = 30$, the perturbation reaches the channel centre and the mode becomes unstable. The amount of energy in the suction half increases to 18.1%. For even higher values of Re_{inj}, for example 45, the upper half holds $\sim 32\%$ of the energy.

Thus it appears that the onset of the cut-off at $Re_{inj,1}$ occurs when the secondary peak holds maximum energy. Increasing injection decays this peak until it reaches a minimum and then starts to grow out from the primary

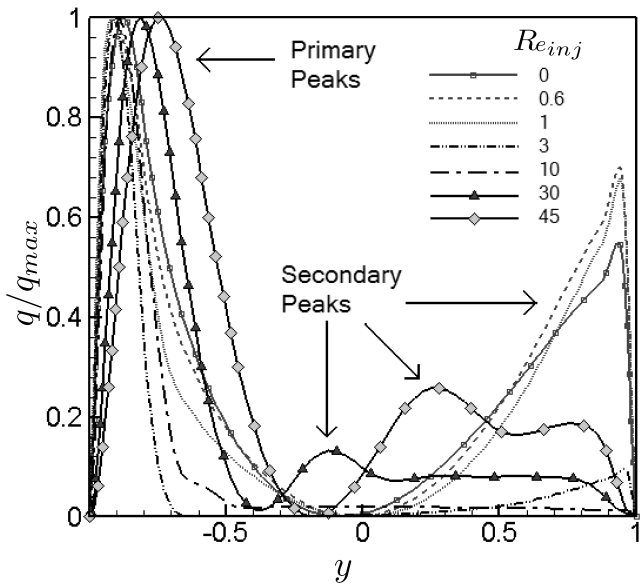

Figure 4.18: Non-dimensional mean perturbation kinetic energy profiles for mode 'C' at different Re_{inj}. Solid lines with symbols denote the unstable modes. For each Re_{inj}, q has been scaled by its maximum value.

peak. The end of the cut-off regime, marked by $Re_{inj} > Re_{inj,2}$, occurs when the secondary peak reaches the channel centre and holds sufficient energy.

4.5.2 Eventual stabilization at $Re_{inj,3}$

We have not studied in detail the eventual stabilization of the flow at very large Re_{inj} (i.e. $Re_{inj} \sim Re_{inj,3}$), but we believe the energetics of this stabilization are due to a decay in the energy production. This can be seen most clearly from the identity (4.19), which is in the same form as that for any parallel shear flow, i.e. cross-flow only influences (4.20) directly. Joseph has used this expression to derive general bounds that depend on $|Du|_{max}$, and

various functional inequalities; see Joseph (1968, 1969). For example, we have linear stability provided that:

$$\alpha Re|Du|_{max} < \max(\xi^2\pi + 2^{3/2}\alpha^3, \xi^2\pi + \alpha^2\pi) \tag{4.28}$$

where $\xi = 2.36502$ is the least eigenvalue of a vibrating rod with clamped ends at $y = \pm 1$.

The condition (4.28) evidently holds for the flows we consider, but is very conservative and especially so in the limit of large Re_{inj}. This conservatism at large Re_{inj} stems directly from the simplistic treatment of Du in bounding the energy production term:

$$\langle(\phi_r D\phi_i - \phi_i D\phi_r)Du\rangle < |Du|_{max} I_0 I_1.$$

With reference to Figs. 4.1 & 4.2 and to (4.11), we see that at large Re_{inj} the base velocity profile consists of a thin layer near the upper suction wall, within which $Du \sim |Du|_{max} \sim Re_{inj}$, which has thickness of $O(Re_{inj}^{-1})$. Away from this thin boundary layer, the velocity gradients are of size $Du \sim 2(kRe_{inj})^{-1} + O(Re_{inj}\mathrm{e}^{-Re_{inj}(1-y)})$. Note however, that within this suction layer, we have $\phi \sim (1-y)^2$ due to the boundary conditions on the perturbation. Therefore,

taking a nominal suction layer boundary at $y = y_s$, we may estimate as follows:

$$\begin{aligned}
\langle(\phi_r D\phi_i - \phi_i D\phi_r)Du\rangle &= \int_{-1}^{1-y_s} (\phi_r D\phi_i - \phi_i D\phi_r)Du \, \mathrm{d}y + \\
&+ \int_{1-y_s}^{1} (\phi_r D\phi_i - \phi_i D\phi_r)Du \, \mathrm{d}y \\
&\leq \frac{2}{kRe_{inj}} \int_{-1}^{1-y_s} |\phi_r D\phi_i - \phi_i D\phi_r| \, \mathrm{d}y \\
&+ O(|Du|_{max}(1-y_s)^4) \\
&\leq \frac{2}{kRe_{inj}} I_0 I_1 + O(Re_{inj}^{-3}) \qquad (4.29)
\end{aligned}$$

Following Joseph (1969), this leads directly to the bound

$$\frac{2\alpha Re}{kRe_{inj}} \lesssim \max(\xi^2\pi + 2^{3/2}\alpha^3, \xi^2\pi + \alpha^2\pi), \qquad (4.30)$$

sufficient for linear stability at large Re_{inj}, (with asymptotically $kRe_{inj} \gtrsim 4$ required). In other words, at large Re_{inj}, the energy production T_2 will decay like $(kRe_{inj})^{-1}$ at leading order, so that the viscous dissipation need only be of this order to stabilize the flow.

4.6 Summary

To summarise, we have presented a detailed analysis of linear stability and instability in the (Re_{inj}, k)-plane, for PCP flow with cross-flow. The most complete analysis concerns the important range of low Re_{inj} and modest k. In this range we have demonstrated that the stabilization mechanism, due to

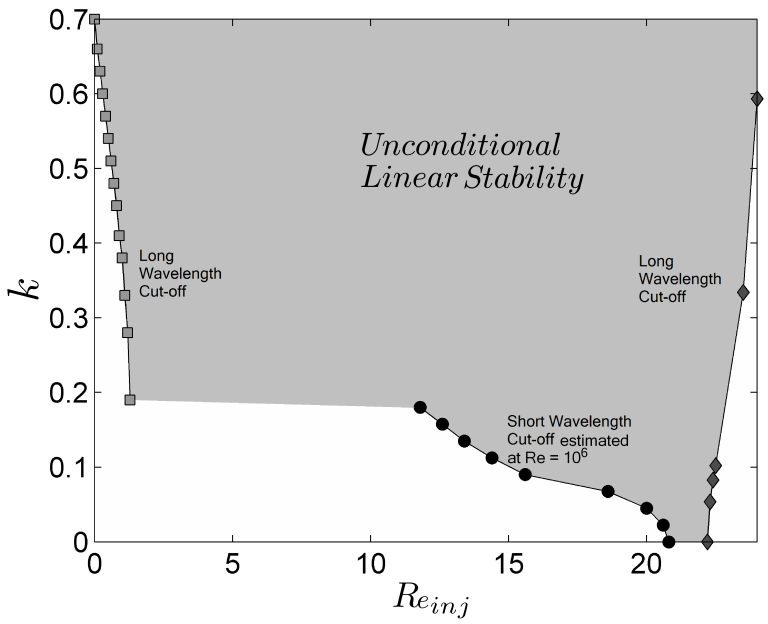

Figure 4.19: Variation of k with Re_{inj}. The filled $\square$ symbols show the long wavelength cut-off achieved for $0.7 \geq k \geq 0.19$. The filled $\circ$ symbols show the shorter wavelength cut-off for $0.19 > k \geq 0$ evaluated numerically for $Re = 10^6$. The filled $\diamond$ symbols imply the second long wavelength cut-off. The shaded region depicts the entire zone of unconditional linear stability.

either injection or wall motion, is essentially the same. Long wavelengths dominate. Skewing of the velocity profile shifts the critical layer and at the same time the energy production is diminished until viscous dissipation dominates at cut-off. In Fig. 4.9, we have also shown an interesting quantitative analogy with the cut-off behavior of ACP flows; see Sadeghi & Higgins (1991).

This lower range of Re_{inj} and modest k is probably that which is most important practically. Essentially, this range allows one to compensate cross-flow by wall-motion and vice-versa, achieving unconditional linear stability via either mechanism. With reference to Fig. 4.1, it is the range of Re_{inj} in which

the cross-flow and wall motion are modifications of a base Poiseuille flow. Due to the scaling, the peak velocity is always 1, but at larger Re_{inj} with modest k the Poiseuille component is completely dominated by cross-flow and wall motion.

Globally, the cut-off regimes in the (Re_{inj}, k)-plane are as illustrated in Fig. 4.19. The shaded area shows the region of unconditional linear stability. In the intermediate range of approximately $1.3 \leq Re_{inj} \leq 20.8$ values of $k \gtrsim 0.19$ are dominated by long wavelengths and are stable. Below this value, we are able to compute numerical cut-off curves for fixed Re. With the limits of our computations, we cannot determine if these cut-off curves asymptote to an unconditional cut-off curve as $Re \to \infty$.

There appears to be a short band of unconditional linear stability for all computed values of k around approximately $20.8 \leq Re_{inj} \leq 22$, before the destabilization occurs at larger $Re_{inj} = Re_{inj,2}$. Since this band can make PP flow unconditionally stable, it could be effectively used in applications where wall motion is not feasible, e.g. cross-flow filtration, medical dialysis. From the practical perspective, it is worth noting that the transition across $Re_{inj,2}$, is from unconditional stability to critical values of Re which are relatively modest (e.g. in the range $10^3 - 10^4$) just a short distance beyond $Re_{inj,2}$. Assuming that the PP flow is linearly unstable, this means stabilization can be achieved with cross-flow velocities of the order of 1% of the mean axial flow velocity.

This destabilization at $Re_{inj,2}$ is again a long wavelength mechanism, which we have analysed using the long wavelength approximation of Cowley & Smith

(1985). A possible cause of this instability has been found to be resonant interactions of the T-S waves. Study of the linear energetics of the upper limit, $Re_{inj,2}$, has shown that neither viscous dissipation, nor the involvement of a critical layer are significant. Rather, the balance of energy production and dissipation within T_2 keeps the mode neutrally stable. Energy analysis of the preferred mode 'C' has revealed that the precursor of the transition to instability from unconditional stability is the amplification of disturbances near the injection wall. The mean perturbation kinetic energy has also been analyzed. It has shown that the lower limit occurs when the secondary peak holds maximum energy. Increasing injection decreases the secondary peak until it reaches a minimum and then it starts to grow from the primary peak. When the secondary peak reaches the channel centre and holds a sufficient amount of energy, the unconditional stability mechanism breaks down.

The final stabilization occurring at large $Re_{inj} \geq Re_{inj,3}$ has been analyzed using linear energy bounds. By careful treatment of the energy production term, we are able to show that the energy production terms decreases asymptotically like Re_{inj}^{-1} as $Re_{inj} \to \infty$. We believe that this mechanism leads to the eventual domination of the viscous dissipation at large enough Re_{inj}.

In terms of the spatial structure of the perturbations, we note that the stabilization at small and moderate Re_{inj} are both long wavelength phenomena for which the approximation of Cowley & Smith has been shown effective. Implicitly therefore, the critical wavenumbers scale like Re^{-1} in these limits. For the shorter wavelength instabilities we have not analysed the asymptotic

behaviour of the wavenumber with Re. A more detailed look at the spatial structure of certain eigenmodes has been presented in Fig. 4.14. This shows a skewing of the streamline recirculatory regimes towards the lower wall for long wavelengths as Re_{inj} is increased, and towards the upper wall at shorter wavelengths as Re_{inj} is increased.

Chapter 5

Conclusions

Education never ends Watson. It is a series of lessons with the greatest for the last. — Sherlock Holmes in The Red Circle.

5.1 Summary

In this thesis we have investigated various aspects of two dimensional shear flow instabilities. In Chapter 2 we have investigated the physical reason behind the exponential amplification of an infinitesimal disturbance in an otherwise stable shear flow. By considering idealized shear layers, we have shown that hydrodynamic instability occurs because two (or more) linear interfacial waves, having arbitrary initial amplitudes and phases, interact with each other in such a way that they eventually attain a resonant configuration. The latter provides the condition for (idealized) shear instabilities; it furnishes with the range of unstable wavenumbers. This generalized wave interaction approach (referred to as wave interaction theory (WIT)) has been validated against three different types of shear instabilities, Kelvin-Helmholtz (KH), Holmboe, and Taylor.

WIT also provides a non-modal description of idealized shear instabilities.

Non-modal instability signifies non-orthogonal interaction between the two wave modes, and is the entire process occurring prior to resonance. Rapid transient growth is a key feature of non-modal instability process. WIT shows that optimal growth occurs when the two waves are in quadrature.

In Chapter 3, the idea proposed in Chapter 2 has been extended to the non-linear regime for the case of KH. It has been shown that the non-linear interaction between two counter-propagating vorticity waves produce elliptical vortices. Contrary to the common notion that KH manifests itself in the form of spiral billow structures, our simulation has shown that elliptical vortices are another asymptotic form of KH. The dynamics of such elliptical vortices (rotation and nutation) as well as the attached thin braids have been investigated. Simple models are shown to provide a leading order description of the vortex and braid dynamics. It has been hypothesized that elliptical vortices in geophysical flows arise due to this phenomenon.

In Chapter 4 we have followed the conventional normal-mode approach to investigate how channel flows can be unconditionally stabilized/destabilized. A channel flow can be unconditionally stabilized by making one of the walls to move (i.e. adding "Couette" component). Previous studies have shown that adding small amount of cross-flow (suction from one wall and injection from the other) produces a stabilizing influence, but little is known about the influence of moderate or large cross-flows. In a parameter space of non-dimensional wall velocity and non-dimensional cross flow velocity, we have investigated how these two parameters influence the stability of a channel flow. It has been

shown that the two effects compensate each other (in the parameter space considered here). Most importantly, it has been found that there exists a small band of cross-flows for which the channel flow is unconditionally linearly stable even in the absence of wall motion.

5.2 Main contributions

The contributions of each Chapter are as follows:

5.2.1 Chapter 2

Here we have been able to provide a mechanistic understanding of shear instabilities in terms of interfacial wave interactions. Moreover we have showed that in the case of idealized shear instabilities, normal modes of spectral analysis, resonant condition of wave mechanics, and equilibrium points of dynamical systems can be brought under one umbrella. We have formulated a condition for idealized, homogeneous or stratified shear instabilities. Our formulation provides a non-modal description of instabilities, hence transient growth processes can be well understood in the light of this theory.

5.2.2 Chapter 3

The main contribution of this work is to bridge contour dynamics with wave interaction theory. We have shown that contour dynamics is the non-linear extension of WIT, and using it we have studied the non-linear evolution of a

piecewise linear shear layer. It is found that this shear layer produces elliptical vortex. The dynamics of this vortex is well predicted by the theory proposed by Kida. By comparing our results with a number of geophysical vortices, e.g. meddies, Jupiter's Great Red Spot, Neptune's Great Dark Spot, we have conjectured that elliptical shaped geophysical vortices probably arise due to the above-mentioned mechanism.

5.2.3 Chapter 4

The main contribution of this chapter is finding the range of non-dimensional wall velocities and non-dimensional injection Reynolds numbers for which the two effects compensate each other. This finding can help developing a robust compensatory design of flow stabilization using either mechanism. The most important contribution of this work is finding a range of non-dimensional injection Reynolds numbers for which the flow is unconditionally stable even in the absence of wall motions. Practically speaking, wall motions are not a feasible option for flow stabilization. Suction-injection on the other hand is comparatively easier to implement. The study can therefore be valuable for various engineering applications where stabilizing the flow is crucial.

5.3 Future research

5.3.1 Chapter 2

Wave interaction theory proposed in Chapter 2 is only valid in the linear regime. In future, this theory needs to be extended into the non-linear regime to understand finite amplitude modal and non-modal instability mechanisms. Although we have extended the KH instability into non-linear domain in Chapter 3, Holmboe and Taylor instabilities need to be considered in future.

Although we have limited our study to the interaction between two waves, the Taylor and Holmboe profiles actually involve multiple wave interactions, which we have neglected. Each density interface in these profiles supports two gravity waves, out of which only the counter-propagating wave has been considered. Noting that two wave interactions are sufficient to produce the normal mode characteristics of Holmboe and Taylor instabilities, it can be argued that the inclusion of co-propagating gravity wave would have been unnecessary. However this wave might have some effect during the initial interaction (non-modal) stages, which needs to be studied in future.

5.3.2 Chapter 3

To better understand the formation of geophysical vortices, more realistic velocity profiles need to be studied. In such flows, the dynamics of the elliptical vortices will be affected by strain-rate as well as background shear. Another interesting aspect worth studying is the nature of the ensuing KH when the

velocity profile is gradually varied from piecewise linear to hyperbolic tangent. Moreover, our analysis is mainly restricted to the early post-saturation phase. We have briefly studied the late post-saturation phase when Kelvin waves appear on the elliptical core. Future study may provide valuable insight into the sustainability of geophysical vortices.

5.3.3 Chapter 4

Future experimental and numerical research needs to be undertaken to shed light into the stabilization of the channel flow by the application of cross-flow. Linear stability analysis has provided us with a range of injection Reynolds number for which the flow is unconditionally stable. Since viscous normal mode stability theory does not correspond very well with experiments or computations, It is unlikely to get the exact predicted range in practice. However linear theory is known to provide an estimate, which can be favorably utilized while designing experiments or performing numerical analysis.

Bibliography

Baines, P.G., Majumdar, S.J. & Mitsudera, H. 1996 The mechanics of the tollmien-schlichting wave. *Journal of Fluid Mechanics* **312** (107), 107–124.

Baines, P.G. & Mitsudera, H. 1994 On the mechanism of shear flow instabilities. *J. Fluid Mech.* **276**, 327–342.

Bretherton, F. P. 1966 Baroclinic instability and the short wavelength cut-off in terms of potential vorticity. *Q. J. Roy. Meteor. Soc.* **92** (393), 335–345.

Cairns, R.A. 1979 The role of negative energy waves in some instabilities of parallel flows. *J. Fluid Mech.* **92**, 1–14.

Carpenter, Jeffrey R., Tedford, Edmund W., Heifetz, Eyal & Lawrence, Gregory A. 2013 Instability in stratified shear flow: Review of a physical interpretation based on interacting waves. *Applied Mechanics Reviews* **64** (6), 061001.

Caulfield, C.P. 1994 Multiple linear instability of layered stratified shear flow. *J. Fluid Mech.* **258**, 255–285.

Caulfield, C.P., Peltier, W.R., Yoshida, S. & Ohtani, M. 1995 An experimental investigation of the instability of a shear flow with multilayered density stratification. *Phys. Fluids* **7**, 3028–3041.

Chérubin, L. M., Serra, N. & Ambar, I. 2003 Low-frequency variability of the mediterranean undercurrent downstream of portimão canyon. *J. Geophys. Res.* **108** (C3), 3058.

Constantinou, Navid C. & Ioannou, Petros J. 2011 Optimal excitation of two dimensional holmboe instabilities. *Phys. Fluids* **23** (7), 074102.

Corcos, G. M. & Sherman, F. S. 1976 Vorticity concentration and the dynamics of unstable free shear layers. *J. Fluid Mech.* **73** (02), 241–264.

Cowley, SJ & Smith, FT 1985 On the stability of poiseuille-couette flow: a bifurcation from infinity. *Journal of Fluid Mechanics* **156**, 83–100.

Davidson, P. A. 2004 *Turbulence: an introduction for scientists and engineers*. Oxford University Press, USA.

Davies, HC & Bishop, CH 1994 Eady edge waves and rapid development. *J. Atmos. Sci.* **51** (13), 1930–1946.

Deem, Gary S. & Zabusky, Norman J. 1978 Vortex waves: Stationary "v states," interactions, recurrence, and breaking. *Phys. Rev. Lett.* **40**, 859–862.

Drazin, P.G. & Reid, W.H. 2004 *Hydrodynamic Stability*, 2nd edn. Cambridge University Press.

Farrell, B. 1984 Modal and non-modal baroclinic waves. *J. Atmos. Sci.* **41** (4), 668–673.

Farrell, B.F. & Ioannou, P.J. 1996 Generalized stability theory. part i: Autonomous operators. *J. Atmos. Sci.* **53** (14), 2025–2040.

Fransson, J.H.M. & Alfredsson, P.H. 2003 On the hydrodynamic stability of channel flow with cross flow. *Physics of fluids* **15**, 436–441.

Goldstein, S. 1931 On the stability of superposed streams of fluids of different densities. *Proc. R. Soc. Lond. A* **132**, 524–548.

Green, MA 2006 Turbulent channel structures, princeton university art of science gallery.

Hains, FD 1967 Stability of plane couette-poiseuille flow. *Physics of Fluids* **10**, 2079–2080.

Hains, FD 1971 Stability of plane couette-poiseuille flow with uniform cross-flow. *Physics of Fluids* **14** (8), 1620–1623.

Hazel, P. 1972 Numerical studies of the stability of inviscid stratified shear flows. *J. Fluid Mech.* **51**, 39–61.

Heifetz, E., Bishop, CH & Alpert, P. 1999 Counter-propagating Rossby waves in the barotropic Rayleigh model of shear instability. *Q. J. R. Meteorol. Soc.* **125** (560), 2835–2853.

Heifetz, E., Bishop, CH, Hoskins, BJ & Methven, J. 2004 The counter-propagating rossby-wave perspective on baroclinic instability. i: Mathematical basis. *Q. J. Roy. Meteor. Soc* **130** (596), 211–231.

Heifetz, Eyal & Methven, John 2005 Relating optimal growth to counterpropagating Rossby waves in shear instability. *Phys. Fluids* **17** (6), 064107.

Hendel, Tal 2008 http://www.mathworks.com/matlabcentral/fileexchange/22423-ellipse-fit.

Holmboe, J. 1962 On the behavior of symmetric waves in stratified shear layers. *Geofys. Publ.* **24**, 67–112.

Hoskins, B.J., McIntyre, M.E. & Robertson, A.W. 1985 On the use and significance of isentropic potential vorticity maps. *Q. J. Roy. Meteor. Soc.* **111** (470), 877–946.

Joseph, D.D. 1968 Eigenvalue bounds for the orr-sommerfeld equation. *J. Fluid Mech* **33** (part 3), 617–621.

Joseph, D.D. 1969 Eigenvalue bounds for the orr-sommerfeld equation. part 2. *J. Fluid Mech* **36** (part 4), 721–734.

Kida, Shigeo 1981 Motion of an elliptic vortex in a uniform shear flow. *J. Phys. Soc. Jpn.* **50** (10), 3517–3520.

Kundu, PK & Cohen, IM 2004 *Fluid Mechanics*. Elsevier, Boston.

Liu, J. & Schneider, T. 2010 Mechanisms of jet formation on the giant planets. *J. Atmos. Sci.* **67**, 3652–3672.

Mack, L.M. 1976 A numerical study of the temporal eigenvalue spectrum of the blasius boundary layer. *Journal of Fluid Mechanics* **73** (3), 497–520.

Mitchell, T. B. & Rossi, L. F. 2008 The evolution of kirchhoff elliptic vortices. *Phys. Fluids* **20** (5), 054103.

Morales-Juberías, R., Sánchez-Lavega, A., Lecacheux, J. & Colas, F. 2002 A comparative study of jovian anticyclone properties from a six-year (1994–2000) survey. *Icarus* **157** (1), 76–90.

Mott, J. & Joseph, D.D. 1968 Stability of parallel flow between concentric cylinders. *Physics of Fluids* **11** (10), 2065–2073.

Nicoud, F. & Angilella, JR 1997 Effects of uniform injection at the wall on the stability of couette-like flows. *Physical Review E* **56** (3), 3000–3009.

Orszag, S.A. 1971 Accurate solution of the orr-sommerfeld stability equation. *J. Fluid Mech* **50** (4), 689–703.

Polivani, L. M., Wisdom, J., DeJong, E. & Ingersoll, A. P. 1990 Simple dynamical models of neptune's great dark spot. *Science* **249**, 1393–1398.

Potter, M.C. 1966 Stability of plane couette-poiseuille flow. *J. Fluid Mech* **24** (4), 609–619.

Pozrikidis, C. 1997 *Introduction to Theoretical and Computational Fluid Dynamics*, first edition edn. Oxford University Press.

Pozrikidis, C. & Higdon, J. J. L. 1985 Nonlinear kelvin–helmholtz instability of a finite vortex layer. *J. Fluid Mech.* **157**, 225–263.

Pullin, D. I. 1992 Contour dynamics methods. *Annu. Rev. Fluid Mech.* **24** (1), 89–115.

Rayleigh, J.W.S. 1880 On the stability, or instability, of certain fluid motions. *Proc. Lond. Math. Soc.* **12**, 57–70.

Reynolds, WC & Potter, M.C. 1967 Finite-amplitude instability of parallel shear flows. *J. Fluid Mech* **27** (3), 465–492.

Romanov, VA 1973 Stability of plane-parallel couette flow. *Functional Analysis and its Applications* **7** (2), 137–146.

Sadeghi, V.M. & Higgins, B.G. 1991 Stability of sliding couette–poiseuille flow in an annulus subject to axisymmetric and asymmetric disturbances. *Physics of Fluids A: Fluid Dynamics* **3** (9), 2092–2104.

Saffman, P. G. 1995 *Vortex Dynamics*, first edition edn. Cambridge University Press.

Schmid, P.J. & Henningson, D.S. 2001 *Stability and transition in shear flows*, , vol. 142. Springer Verlag.

Sheppard, D.M. 1972 Hydrodynamic stability of the flow between parallel porous walls. *Physics of Fluids* **15** (2), 241–244.

Smyth, W. D. & Moum, J. N. 2012 Ocean mixing by kelvin-helmholtz instability. *Oceanography* **25**, 140–149.

Squire, HB 1933 On the stability for three-dimensional disturbances of viscous fluid flow between parallel walls. *Proceedings of the Royal Society of London. Series A* **142** (847), 621–628.

Sutherland, B.R. 2010 *Internal gravity waves*. Cambridge University Press.

Taylor, G.I. 1931 Effect of variation in density on the stability of superposed streams of fluid. *Proc. R. Soc. Lond. A* **132**, 499–523.

Trefethen, L.N., Trefethen, A.E., Reddy, S.C. & Driscoll, T.A. 1993 Hydrodynamic stability without eigenvalues. *Science* **261**, 578–584.

Waugh, D.W. & Randel, W.J. 1999 Climatology of arctic and antarctic polar vortices using elliptical diagnostics. *J. Atmos. Sci.* **56** (11), 1594–1613.

Winters, K. B., MacKinnon, J. A. & Mills, B. 2004 A spectral model for process studies of rotating, density-stratified flows. *J. Atmos. Ocean. Tech.* **21**, 69–94.

Appendix

Stokes' Theorem applied on a vorticity interface

Stokes' theorem relates the surface integral of the curl of a vector (in our case this vector is velocity) field $\vec{u}$ over a surface A to the line integral of the vector field over its boundary δA:

$$\oint_{\delta A} \vec{u}.d\vec{l} = \iint_{A} (\nabla \times \vec{u}) .d\vec{A} \tag{5.1}$$

Holmboe (1962) used this theorem to relate the interfacial displacement η_i with the difference in velocity perturbation $(u_i^+ - u_i^-)$ produced at a vorticity interface; see Eq. (2.12). This equation is referred to as "Eq. (3.2)" in his paper. However, the relevant steps required to derive this equation has not been provided. In order to understand how Eq. (2.12) is obtained, we first graphically describe the problem in Fig. 5.1. The background velocity is such that the flow is irrotational when $z > z_i$, and has a constant vorticity, say S, when $z \leq z_i$. When the interface is disturbed by an infinitesimal displacement η_i (solid black curve in Fig. 5.1), the velocity field also changes slightly - the perturbation velocity in the upper layer $(z > z_i)$ becomes u_i^+ and that in the lower layer $(z \leq z_i)$ becomes u_i^-.

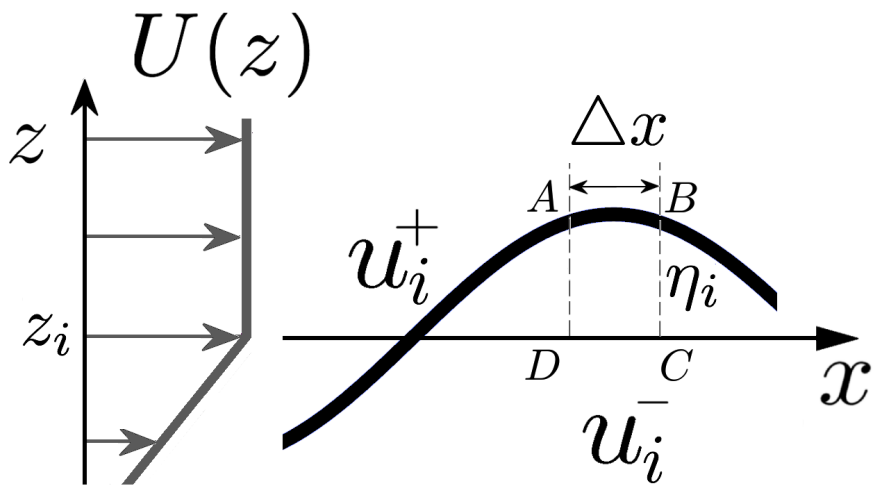

Figure 5.1: Schematic of a vorticity interface - left half shows unperturbed velocity field, while the right half depicts infinitesimal interfacial displacement.

Let us consider a circuit A-B-C-D, see Fig. 5.1. Applying Stokes' theorem, we obtain

$$(u_i^+ - u_i^-)\triangle x = S.A \tag{5.2}$$

where $A = \eta_i \triangle x$ is the area of A-B-C-D, and $S = \nabla \times \vec{u}$ is the vorticity in this area. Therefore we obtain

$$u_i^+ - u_i^- = S\eta_i \tag{5.3}$$

which is basically Eq. (2.12).

Normal mode form of Holmboe instability

Both interfaces in the Holmboe profile (Eq. (2.67)) individually satisfy the kinematic condition:

$$\frac{\partial \eta_1}{\partial t} = \frac{\partial}{\partial x}\left(e^{-\alpha}\psi_2 + \frac{1-2\alpha}{2\alpha}\eta_1\right) \tag{5.4}$$

$$\frac{\partial \eta_2}{\partial t} = \frac{\partial}{\partial x}\left(\psi_2 + \frac{e^{-\alpha}}{2\alpha}\eta_1\right) \tag{5.5}$$

where ψ_2 is the stream function perturbation at the lower interface. This interface being a density interface also satisfies the dynamic condition:

$$\frac{\partial \psi_2}{\partial x} = \frac{J}{\alpha}\frac{\partial \eta_2}{\partial x} \tag{5.6}$$

We assume the perturbations to be of normal-mode form: $\eta_1 = \hat{\eta}_1 e^{i\alpha(x-ct)}$, $\eta_2 = \hat{\eta}_2 e^{i\alpha(x-ct)}$, and $\psi_2 = \hat{\psi}_2 e^{i\alpha(x-ct)}$. Here the wave speed c is generally complex. Defining $\hat{\varsigma} = \begin{bmatrix} \hat{\psi}_2 & \hat{\eta}_2 & \hat{\eta}_1 \end{bmatrix}^T$, we obtain the following eigenvalue problem:

$$(M + cI)\,\hat{\varsigma} = 0 \tag{5.7}$$

where

$$M = \begin{bmatrix} 0 & J/\alpha & 0 \\ 1 & 0 & e^{-\alpha}/(2\alpha) \\ e^{-\alpha} & 0 & (1-2\alpha)/(2\alpha) \end{bmatrix} \tag{5.8}$$

Eq. (5.7) generates the following characteristic polynomial:

$$c^3 + \left(\frac{1-2\alpha}{2\alpha}\right)c^2 - \frac{J}{\alpha}c - J\left(\frac{1-2\alpha}{2\alpha^2}\right) + J\frac{e^{-2\alpha}}{2\alpha^2} = 0 \tag{5.9}$$

This equation produces complex conjugate roots only when the discriminant is negative. Since the presence of complex roots signify normal-mode instability, negative values of the discriminant is of our interest. The discriminant (D) in this case is given by:

$$\begin{aligned} D = {} & 16\alpha^2 J^2 - \alpha J\left[8\left(2\alpha-1\right)^2 + 36e^{-2\alpha}\left(2\alpha-1\right) + 27e^{-4\alpha}\right] \\ & - \left(1-2\alpha\right)^3\left(2\alpha - 1 + e^{-2\alpha}\right) \end{aligned} \tag{5.10}$$

Imposing the condition $D < 0$, we find

$$\frac{1}{2A}\left(-B - \sqrt{B^2 - 4AC}\right) \leq J \leq \frac{1}{2A}\left(-B + \sqrt{B^2 - 4AC}\right) \tag{5.11}$$

where

$$\begin{aligned} A &= 16\alpha^2 \\ B &= -\alpha\left[8\left(2\alpha-1\right)^2 + 36\left(2\alpha-1\right)e^{-2\alpha} + 27e^{-4\alpha}\right] \\ C &= \left(2\alpha - 1 + e^{-2\alpha}\right)\left(2\alpha-1\right)^3 \end{aligned}$$

Thus Holmboe instability occurs only when the condition in Eq. (5.11) is satisfied.